ECOLE
POLYTECHNIQUE
DE BRUXELLES

ULB

UNIVERSITÉ LIBRE DE BRUXELLES

Defect detection in silicon charged particle detectors with a short-wave infrared (SWIR) camera

In order to be awarded the Master's Degree in
Physics Engineering

Mathias Beghuin

Master thesis submitted under the supervision of
Pr. Nicolas Pauly

The co-supervision of
Dr. Yannick Allard
Pr. Pascal Vanlaer

Research department
Interuniversity Institute for High Energies (IIHE)

Academic year
2024 - 2025

ECOLE
POLYTECHNIQUE
DE BRUXELLES

DOCUMENT TO BE INCLUDED IN THE MASTER THESIS

CONSULTATION OF THE MASTER THESIS

I, the undersigned

NAME Beghuin

FIRST NAME Mathias

MASTER PROGRAM Physics Engineering

MASTER THESIS TITLE Defect detection in silicon charged particle detectors with a short-wave infrared (SWIR) camera

AUTHORIZE*

~~REFUSE~~*

(IN CASE OF REFUSAL, THIS DOCUMENT MUST BE COUNTERSIGNED BY THE MASTER THESIS SUPERVISOR)

(Delete as appropriate)*

Consultation of this master thesis by users of the libraries of the Université libre de Bruxelles.

If consultation is authorised, the undersigned hereby grants the Université libre de Bruxelles a free and non-exclusive licence, for the duration of the legal term of protection of the work, to reproduce and communicate to the public the above-mentioned work, on graphic or electronic media, in order to enable users of the libraries of the ULB and other institutions to consult it within the framework of inter-library loan.

Brussels, 18/08/2025

Signature of the student

Signature of the supervisor
(only if consultation is refused)

Abstract

Keywords: CMS Phase-2 Upgrade, silicon strip detector, defect detection, electroluminescence, short-wave infrared (SWIR) camera, particle physics

In the early 1950s, a group of physicists founded the European Organization for Nuclear Research, better known as CERN, to foster international collaboration in high-energy particle physics through the construction and operation of particle accelerators. Today, at CERN, protons and heavy ions can be accelerated to nearly the speed of light using a complex chain of accelerators.

The Large Hadron Collider (LHC) is CERN's largest accelerator, located 100 m underground with a circumference of 27 km. Inside, two counter-rotating particle beams are brought into collision to study the fundamental nature of our universe, aiming to overcome the incompleteness of the Standard Model.

The Compact Muon Solenoid (CMS) is a massive detector positioned at one of the LHC's collision points, designed to study the particles produced in these collisions. With the upcoming High-Luminosity LHC (HL-LHC) project, expected to be operational by 2030, CMS will undergo major upgrades through the Phase-2 Upgrade Project, which includes a complete replacement of its silicon tracker used to reconstruct the trajectories of charged particles around the collision point.

The new tracker will be partly composed of 2S modules, which are silicon strip detection units. Each module consists of two silicon sensors that collect free carriers generated by charged particles crossing the material, transmitting a signal to aluminum readout strips 5 cm long and spaced by 90 µm across the sensor surface.

The upgrade requires the production of at least 7680 such modules across CMS partner institutes. The Interuniversity Institute for High Energies (IIHE) is expected to assemble over 1500 modules. However, the assembly line involves repeated handling of the fragile silicon sensors, creating risks of damage. Efficient quality control is therefore essential to characterize and validate the sensors against the required specifications.

This thesis aims to design and build an experimental setup to explore two techniques with potential for defect detection in silicon sensors.

Silicon, as a semiconductor, has an indirect forbidden bandgap of 1,12 eV at room temperature. Optically, photons with an energy below or near this value are only weakly absorbed. In this work, this property is referred to as the transparency of silicon in the short-wave infrared (SWIR) range. The first technique therefore explores illuminating the silicon sensors in the SWIR to exploit this transparency and attempt to reveal potential defects using a SWIR camera.

The second technique relies on electroluminescence (EL). In the 2S sensors, a reverse-biased p-n junction extends the depletion region where ionizing particles generate carriers that

create the signal. Under forward bias, injected carriers recombine and emit photons with energies close to the bandgap, in the same way as a LED. This is EL. Widely employed for defect detection in silicon solar cells, extending this technique to charged particle detectors could offer a major advantage for quality control.

The first stage of this work focused on the design, assembly, and commissioning of the experimental setup inside a light-isolated cabinet. It includes a SWIR camera and a set of infrared LEDs mounted with 3D-printed holders on a metallic frame, enabling vertical imaging at multiple magnifications. Storage requirements for the 2S modules also led to the implementation of a pneumatic system to dry the air inside the cabinet. A microcontroller on a custom electronic board was programmed to provide control of the LEDs in the setup.

Experiments on silicon solar cells and a wafer fragment confirmed the ability of the setup to reveal defects using both methods. These initial results were encouraging for both SWIR transparency imaging and EL.

The study was then extended to 2S sensors and older-generation strip sensors. For transparency imaging, the inspection of a sensor with irregular electrical characteristics did not reveal any specific defects. However, since the cause of its irregular behavior remains unknown, no firm conclusion can be drawn on the method's inefficiency. This analysis also highlighted some limitations of the setup. EL analysis, on the other hand, required currents beyond what the 2S module electronics can sustain, which limits its relevance for quality control. Moreover, the confinement of EL emission to the sensor edges further reduces its usefulness compared with solar cell analysis.

In conclusion, the setup successfully revealed defects by transparency and EL in solar cells, but results on strip sensors proved less conclusive. Transparency imaging remains of interest for sensor inspection, although no clear defects were detected in strip sensors in this study, whereas EL appears unsuitable due to its destructive impact on the module electronics. Based on the current results, these methods cannot yet be considered sufficient for systematic inspection of freshly assembled modules in production.

Nevertheless, this study points to possible future developments, including improved EL imaging and photoluminescence approaches, to overcome current limitations and enhance defect detection.

Mathias Beghuin
Physics Engineering
Defect detection in silicon charged particle detectors with a short-wave infrared (SWIR) camera
Academic Year 2024-2025

Contents

Chapter 1

Context

1.1 The CERN accelerator complex

In the late 1940s, the world was in a post-war context, and physics research in Europe was stagnating . A group of physicists proposed the idea of building a large international research facility to foster intergovernmental and peaceful collaboration. To this end, the European Organization for Nuclear Research, or CERN (standing initially for "Conseil européen pour la recherche nucléaire" in French), was established by a convention between 12 states, with the mission of enabling collaboration in the field of high-energy particle physics research through the construction and operation of particle accelerators [1]. This convention established that every research or result must be public, and research must never be with military purposes.

The Organization has been joined by other states and now counts 23 Member States. Its headquarters is located in Geneva. Research institutes from around the world use CERN's facilities for their experiments, which have, to date, led to several scientific achievements, such as the discovery of the Z and W bosons [2] and the detection of the Higgs boson [3].

CERN's accelerator complex is a succession of machines, each injecting a particle beam into the next, which then accelerates it to increasingly higher energies. The largest accelerator of this complex is the Large Hadron Collider (LHC) and led to the discovery of the Higgs boson. This complex is represented in figure 1.1.

1.2 The Large Hadron Collider

The LHC is a 100 m underground circular accelerator that accelerates and collides protons and heavy-ion beams at a speed close to the speed of light in a 27 km tunnel [5]. Since its first operation in 2009, the center-of-mass energy $\sqrt{s}$ of the collisions at the LHC has in steps grown from 7 to 13.6 TeV, as represented on Figure 1.4. These collisions take place at four experimental locations on the LHC track, as depicted in Figure 1.1: at CMS, LHCb, ATLAS and ALICE. At each of these particle detectors, experiments and measures are made to try to understand the nature of the universe and to overcome the incompleteness of the standard model. The main questions they try to answer with the LHC are related to the origin of mass, dark matter and dark energy, supersymmetry, matter and antimatter asymmetry and quark-gluons plasmas.

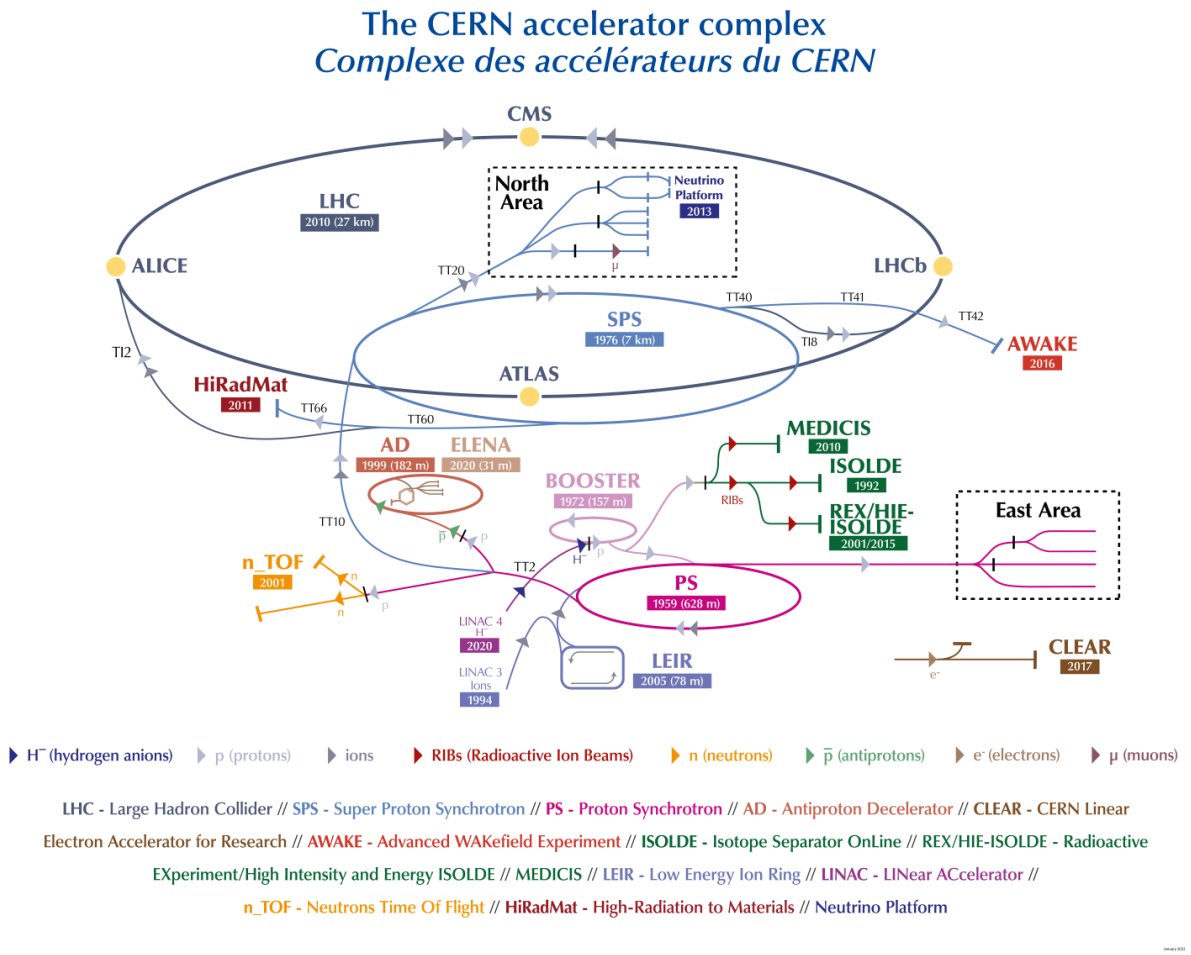

Figure 1.1: The CERN accelerator complex, taken from [4].

1.3 The Compact Muon Solenoid

The Compact Muon Solenoid CMS is a large particle detector located at one of the four collision spots of the LHC. It has been designed to study particles produced during high-energy proton-proton and nucleon-nucleon collisions [6, p. 277-352]. CMS has the same broad physics programme as ATLAS but differs in its design, allowing for a comparison of the results of the measurements performed.

As depicted on Figures 1.2 and 1.3, the CMS detector is composed of:

- **a superconducting solenoid**, cooled at 4.65 K, generating a homogeneous magnetic field of 3.8 T enabling the bending of trajectories of charged particles;
- **a silicon tracker** near the collision point, which measures the trajectories of charged particles;
- **an electromagnetic calorimeter** which is a $PbWO_4$ scintillating crystal, used to measure the energy of photons and electrons;
- **a hadron calorimeter** which is a sampling calorimeter with brass as an absorber and scintillating plastic as an active material. It is principally designed to detect particles made up of quarks;

- **Muon chambers** (muon detectors) are interleaved with iron "return yoke" plates at the outer part of the superconducting solenoid, covering angles up to 10° from the beam direction.

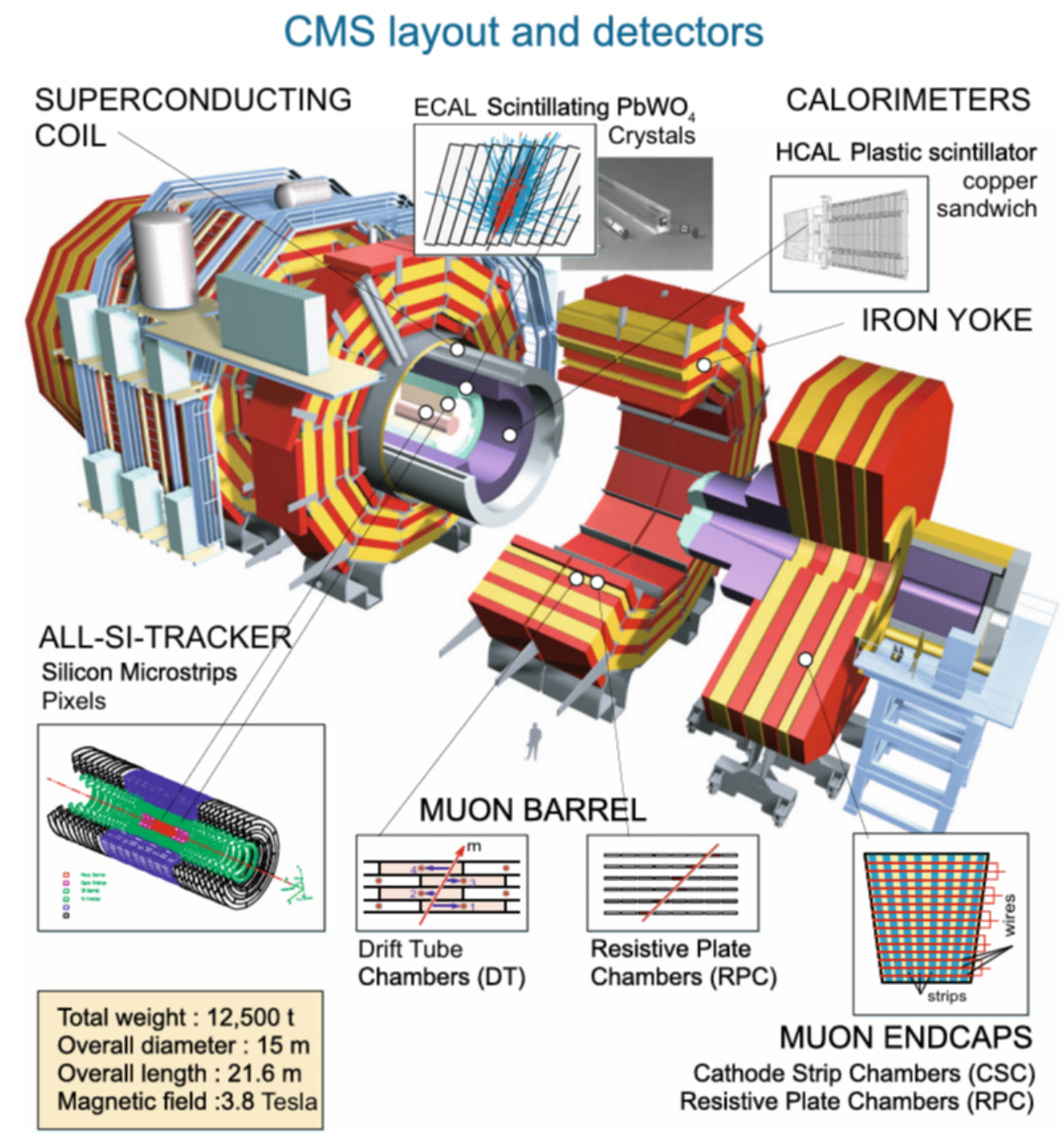

Figure 1.2: The CMS detector and its components, taken from [6].

This configuration enables to measure the momentum p of stable charged particles with a great precision reconstruct their track. Indeed, the greater the momentum, the less the trajectory is deflected by the magnetic field. Outside the tracker, the calorimeters aim to measure the energy of the stable charged and neutral particles (except muons and neutrinos), which means that the silicon tracker should interfere as little as possible with the particles. The iron magnet "return yoke", at the outer part of the detector, is used to confine the magnetic field and to stop all remaining particles except muons and neutrinos.CMS is designed to detect particles with momenta ranging from as low as 100 MeV up to a few TeV [6]. All

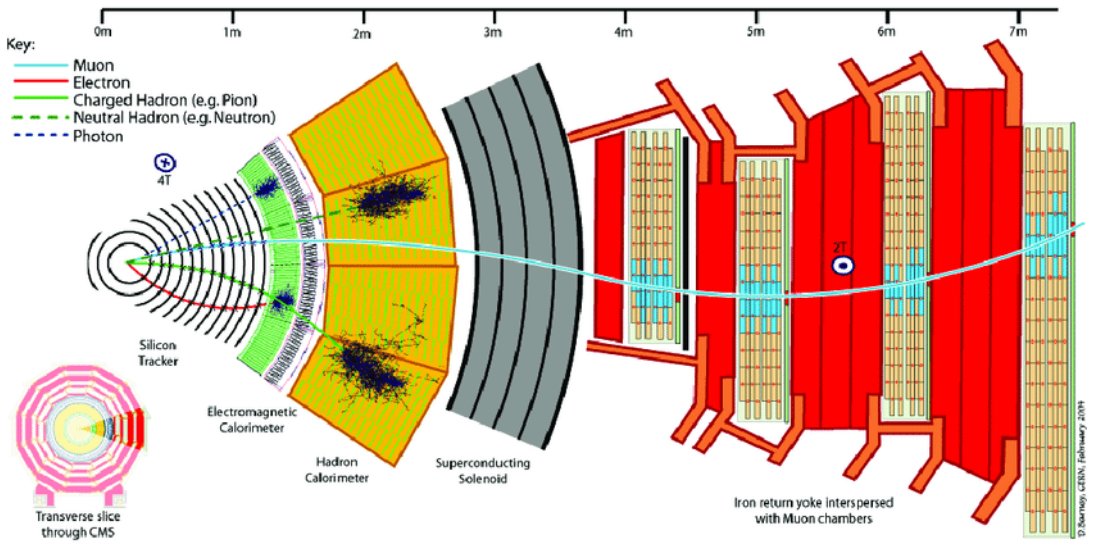

Figure 1.3: Transverse slice of the CMS detector, taken from [7].

these measurements enable the data analysts to identify particles produced by proton-proton or nucleus-nucleus interactions.

1.4 The High Luminosity LHC

The LHC does not contain continuous beams of particles, but beams composed of bunches of particles due to the design of the accelerator (synchrotron accelerator) [8, p. 26]. The CMS detector thus has to work at a fast response time of 25 ns to resolve the bunch crossing rate where about 65 proton-proton inelastic collisions occur per crossing of proton bunches. This induce around 1000 particles per bunch crossing at an instantaneous luminosity of the order of $\mathcal{L} = 10^{34}$ cm^{-2} s^{-1} [9]. The luminosity constitutes one of the most important parameter in the physics of colliders. It quantifies the number of potential events per time unit and per cross section. It is defined as:

$$\frac{dR}{dt} = \mathcal{L}\sigma \tag{1.1}$$

where dR/dt is the number of interactions per time unit and σ is the cross section at a given energy for a given interaction between particles brought into collision [8, p. 252]. To study rare events with a small cross section, it is thus important for colliders such as the LHC to reach high luminosities.

A higher revolution frequency, a higher number of bunches, a higher number of particles per bunch or a smaller beam size are parameters that induce a higher luminosity. The integrated luminosity is defined as:

$$L_i = \int \mathcal{L} dt \tag{1.2}$$

It is usually expressed in fb^{-1} and can be interpreted as the number of occurrence of an interaction with a cross section of 1 fb during the period of integration. The integral is usually taken over the duration of the experiment.

The High Luminosity LHC (HL-LHC) is a project aiming to upgrade the LHC in order to exploit the full capacity of the collider by increasing the instantaneous luminosity by a factor

of 7,5 over its nominal value. This upgrade will allow the CMS and the ATLAS experiment to collect integrated luminosities of 4000 fb^{-1} [10].The HL-LHC project is, to this end, exploring new beam configurations and new technologies in the domain of superconductivity, cryogenics, electronics, rad-hard materials and remote handling. A long shutdown (LS3) of the LHC is thus planned in 2026 to perform the update of the LHC. Figure 1.4 provides a timeline of the performances of the LHC since Run 1 to the the HL-LHC. The upgrades of ATLAS, CMS, ALICE and LHCb are also represented. The HL-LHC will be in operation from 2030 to 2041.

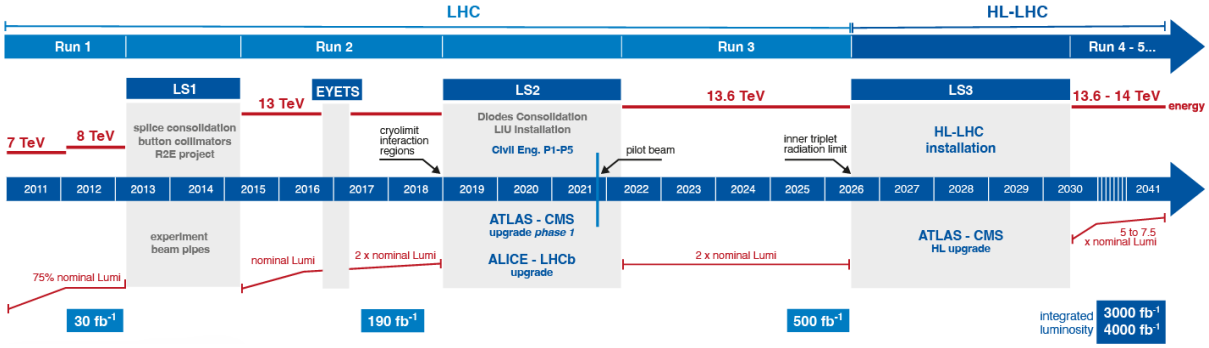

Figure 1.4: The LHC to HL-LHC timeline, taken from [11].

1.5 The Phase-2 Upgrade of CMS's Silicon Tracker

In order to exploit the increase of luminosity provided the HL-LHC, the CMS detector has to be substantially upgraded. This project is known as the CMS Phase-2 Upgrade. The increase of particle density requires a higher detector granularity and improved radiation hardness (the capability of electronics to withstand radiation without performance degradation [6, 12, 13]). The CMS capabilities will greatly benefit from an extended acceptance of the tracker and calorimeters but also from improved trigger capabilities [14]. To this aim, the entire silicon tracker needs to be replaced.

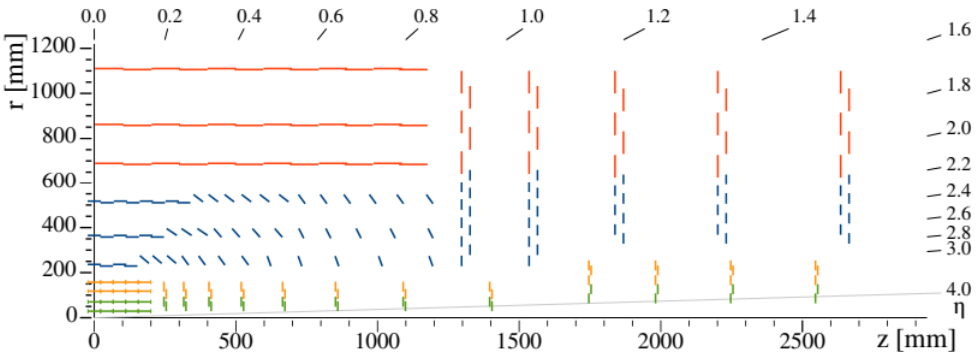

Figure 1.5: Sketch of one quarter of the tracker layout in r-z view. The origin is at the collision center of CMS and the z axis is along the longitudinal axis of CMS. η stands for the pseudorapidity. Taken from [14].

The tracker will be composed of two distinct subsystems: the Inner Tracker and the Outer Tracker. The inner part of the tracker will be based on pixel detector technology with 25x100 μm^2 and 50x50 μm^2 pixels [14]. These detection modules are represented in green and

yellow on Figure 1.5. Above 200 mm in the radial region, the Outer Tracker is based on silicon macro-pixel and strip technology. On Figure 1.5, the blue detection modules are composed of one macro pixel and one strip sensor (PS modules) where some of them are tilted for trigger efficiency reasons. In red, modules composed of 2 strip sensors (2S modules) are represented. This work will focus on these 2S modules.

1.6 The 2S Modules

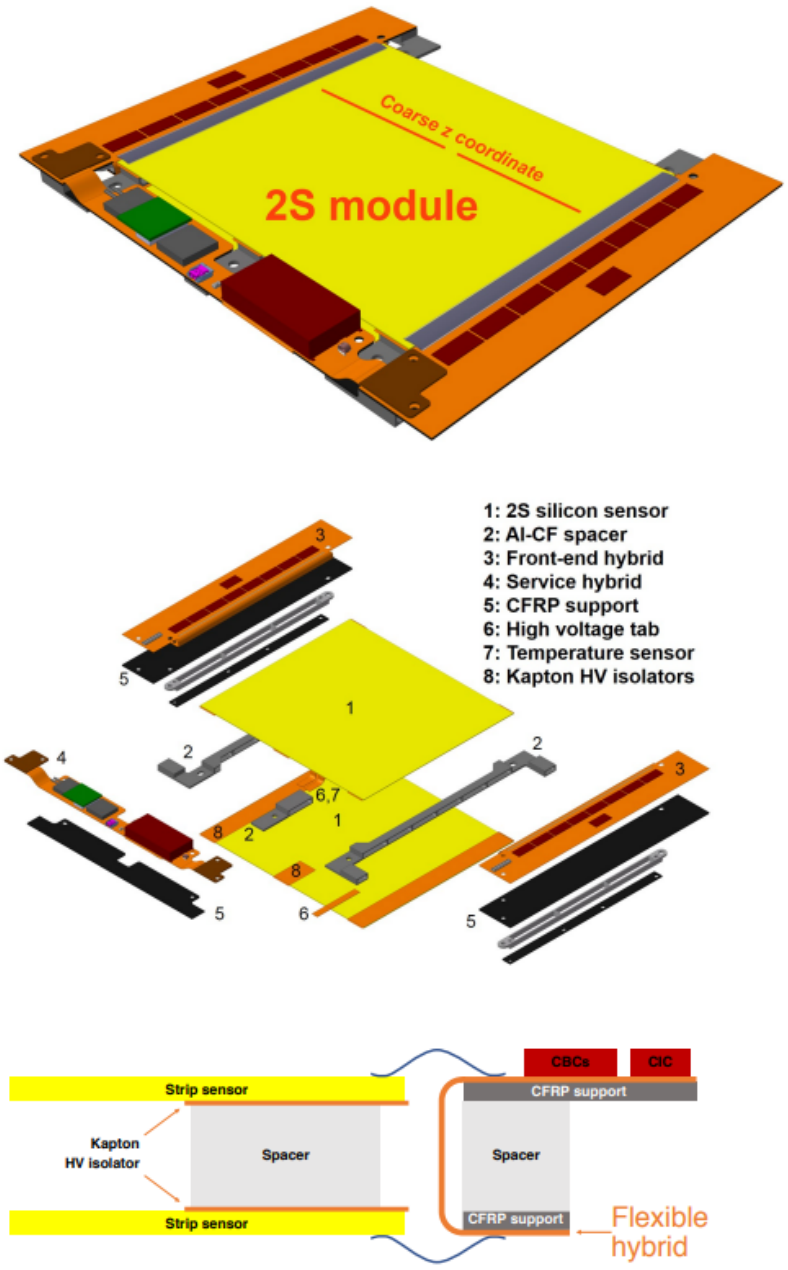

Figure 1.6: The 2S module with the two sensors and the readout hybrids, taken from [14].

This section is mostly based on the specifications given in [14]. The 2S modules consist of two silicon strip sensors, glued a few millimeters apart on both sides of aluminum-carbon fiber composite spacers, and wirebonded to the readout chips. Each sensor is composed of

2x1016 strips with a pitch of 90 μm and a length of 5 cm. Strips are arranged in pairs on a sensor along the z coordinate, shown in Figure 1.6. The physical dimensions of the sensors are 94183x102700 μm^2 with a thickness of 320 μm. Figure 1.6 shows a picture of the composition of a 2S module. The sensors are separated by spacers and high voltage isolators. Two variants of 2S modules are needed for the tracker depending on the resolution needed in the tracker layout: modules with a gap between the sensors of 1,8 mm or 4 mm. In total, more than 15000 such modules (of both variants) need to be produced across 10 production centers. The assembly of more than 1500 modules of both variants for the outer tracker is planned to be performed in Brussels at the Interuniversity Institute for High Energies (IIHE), which is a joint institute of Université Libre de Bruxelles (ULB) and Vrije Universiteit Brussel (VUB).

1.6.1 The Level-1 trigger decision

For the 2S modules, the charged particle passes through two strip sensors, as shown on figure 1.6. If the particle momentum is above a certain threshold p_T, the particle will generate a correlated signal (a stub) in both sensors of the module since its trajectory will be less bended by the magnetic field of the superconducting solenoid [10]. Under this threshold, the signal is not correlated and not sent to the online track reconstruction (L1 trigger). Figure 1.7 shows an illustration of L1 trigger decision. This enable to reduce the amount of data and to output a stub data stream of 40 MHz.

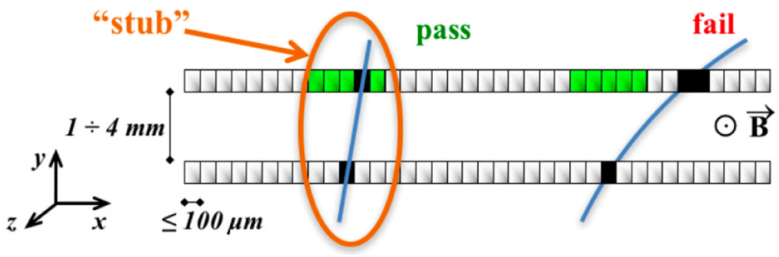

Figure 1.7: Cross section of the two sensor layers of a silicon module and illustration of the Level-1 trigger decision, taken from [10].

1.6.2 The assembly line at IIHE

The assembly line at IIHE is operational, with the objective of producing six modules per day. Figure 1.8 describes the assembly steps involved in assembling a 2S module.
Most steps involve gluing, wire bonding, and encapsulation (i.e., covering the bonding microwires with soft glue), interspersed with quality control tests such as IV curve measurements, alignment checks, and burn-in tests. Throughout or between each step, the sensors are subject to numerous manipulations. Human handling, quality control procedures, the use of weight plates, vacuum systems, and spring mechanisms to secure the sensors in the jigs all present potential risks for sensor damage (e.g., breaks, cracks or electrostatic discharges). Appendix A provides a more detailed description of the jig-based assembly technique used in the IIHE assembly line.

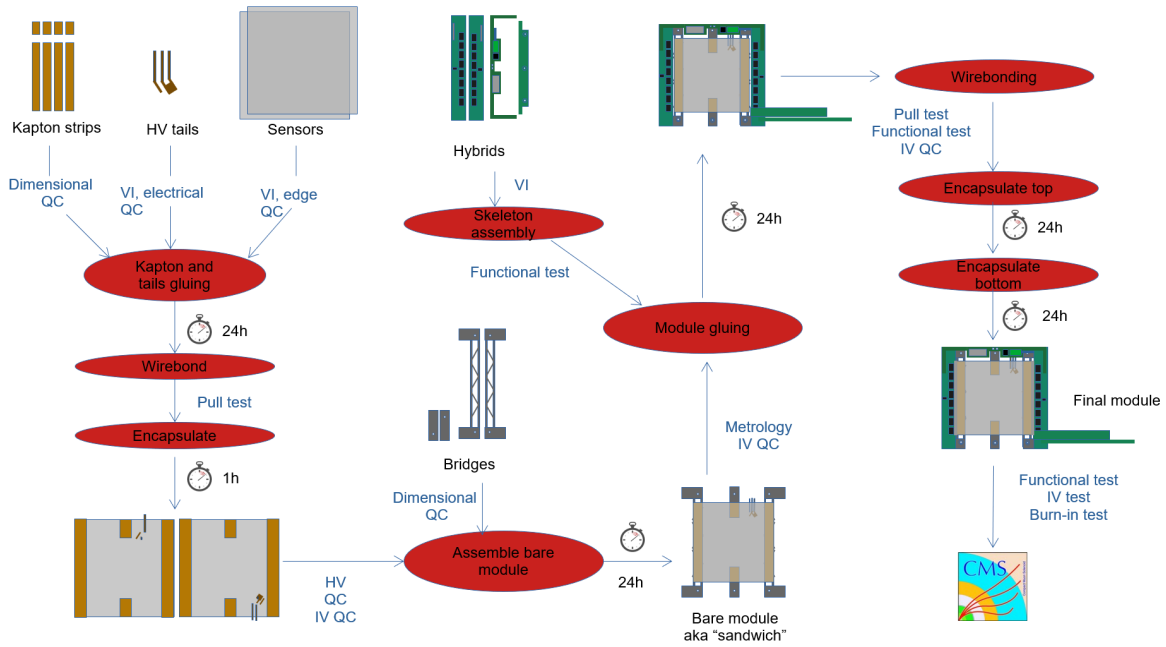

Figure 1.8: Assembly steps carried out at IIHE. Courtesy of Martin Delcourt.

1.7 The strip sensors

Tracking detectors make use of the free charges resulting from the ionization performed by a charged particle passing through the sensor.

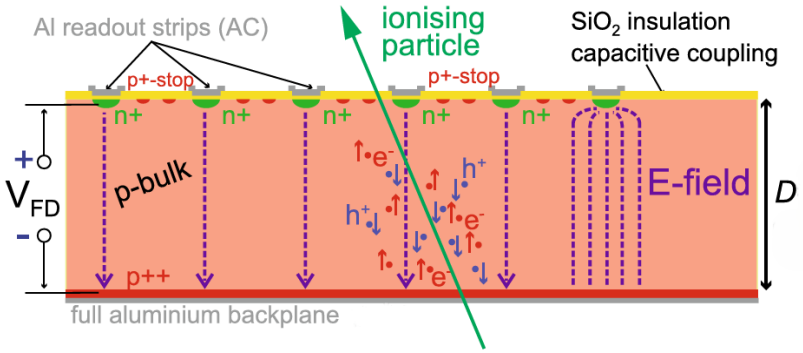

Figure 1.9: Schematic of a n-in-p strip sensor. In the case of the sensors used for the phase-2 upgrade of the CMS tracker, the physical thickness D = 320 μm. Taken and modified from [14].

Silicon particle detectors are usually reverse biased p-n junctions where a high voltage is applied in order to extend the depletion region. The voltage at which the depletion region is fully extended is called the full depletion voltage V_{FD}. The free carriers created by the incident particle are collected in order to generate a signal. Figure 1.9 shows the schematic principle of a n-in-p strip sensor used in the 2S modules. n-doped strips are implemented in a p-doped substrate to collect electrons, which are then capacitively coupled (AC) to aluminium readout strips. These readout strips are themselves directly connected to the charge preamplifier of the readout chip.

The p^+ stop implants are necessary to isolate the individual strips and to ensure a proper

electric field distribution, while the p^{++} doping at the aluminium backplane ensures a good ohmic contact with the alumium backplane.

1.7.1 Production of a n-in-p silicon strip sensors

The following section provides a brief overview of the production of silicon sensors from pure sand. It is based on [15] for the processing of sand into highly purified silicon ingots, on [16] for the technical specifications of the strip sensors used in the CMS upgrade project, and on [6] for both aspects. The reader is referred to the aforementioned references for more detailed information on the production processes.

Starting from simple mined quartz sand (SiO_2), a series of purification and distillation processes lead to Electronic Grade Silicon (EGS) with less than 1/100 ppb[1] impurity.

Following an extensive R&D campaign conducted by CMS, high resistive p-type wafers were selected produced in Float-Zone (FZ) technology with a crystal orientation of $\langle 100 \rangle$. Table 1.1 summerizes the substrate specification selected for the production on the 2S sensors. The FZ crystal growth technique was selected for its mass-production capabilities. This technique is necessary for further purification to "sensor-grade" silicon, as well as for the doping process and the manufacturing of single-crystal ingots.

Wafer size	150mm
Type	p-type FZ
Crystal orientation	<100>
Thickness (physical)	320 µm
Thickness (active)	290 µm
Thickness tolerance	$\pm$ 5 %
Resitivity	>3.5 kΩcm
Oxygen concentration	1.5x10^{16} - 6.5x10^{17} cm^{-3}

Table 1.1: Wafer specifications, taken and adapted from [16].

The silicon ingot is cut into wafers about 1 mm thick. They then undergo lapping, etching, and polishing steps, reducing them to the desired thickness of 320 μm while removing imperfections, eliminating surface impurities, and minimizing the number of defects.

The wafer can thus be processed through a series of oxidation, photolithography, doping, etching, Chemical Vapor Deposition (CVD), and thinning steps to obtain the desired detector with the structure illustrated in Figure 1.10. Various defects may arise during processing, including pinholes, undesired increases in capacitance, cross-talk between channels, trace contamination in oxide layers, and failures affecting neighboring strips. Since a single sensor occupies the entire wafer, even one defect can lead to the rejection of the whole processed wafer. Finally, the wafer is passivated with a SiO_2 layer to protect most of the surface; otherwise, the silicon would react with contaminants from the environment.

The sensor is then cut from the wafer using a diamond saw with continuous water flushing. This operation is known to cause cracks and burns, necessitating meticulous inspection during quality control.

[1] Part per billion.

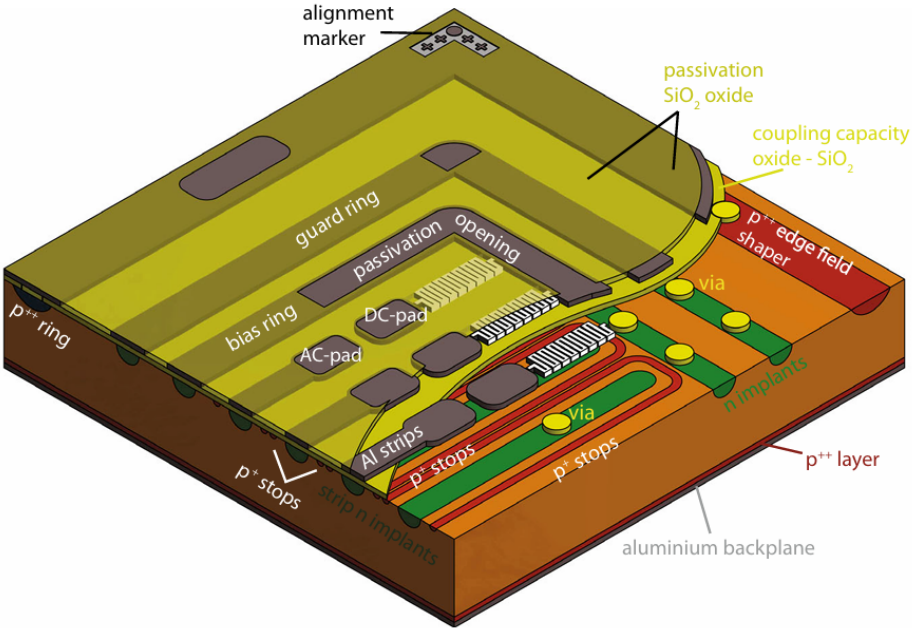

Figure 1.10: 3D schematic of the corner of a n-in-p strip sensor, taken from [6].

1.7.2 Bias, guard and edge ring

This section describes the role of the different structures shown in Figure 1.10, which are further explained in [6, p. 48-59]. Three main rings surround the entire sensor: the bias ring, the guard ring, and the edge ring.

To bias the sensor and ensure a homogeneous electric field distribution, the implant strips are connected to the bias ring via polysilicon bias resistors (the white serpentine structures visible in Figure 1.10). The bias ring is wire-bonded to the bias terminal and is generally connected to ground (GND), while the aluminium backplane is biased with a negative high voltage.

The purpose of the guard ring is to shape the electric field, ensure a uniform potential for each strip, and serve as a drain for leakage currents at the edges.

The active edge ring is brought to the same potential as the backplane to prevent the extension of the depletion zone to the sensor's physical edge, which would create a conductive surface and increase leakage current. This is necessary because the sensor cutting process introduces microcracks at the edges, which in turn induce energy levels in the silicon bandgap with a high density of defects.

Figure 1.11 shows a simulation of the depletion zone extension for various bias voltages, given the ring structure.

1.7.3 Common strip faults

The strip sensors dedicated to the CMS upgrade are rejected if more than 1% of bad strips per sensor are detected, or if more than two bad strips appear within any set of five consecutive strips [16, p. 13]. Common strip defects are listed in [6, p. 60-62]:

- **Pinholes** in the $\mathrm{SiO_2}$ layer can create shorts or low-ohmic connections between the readout strip and the implant, potentially leading to amplifier overload.

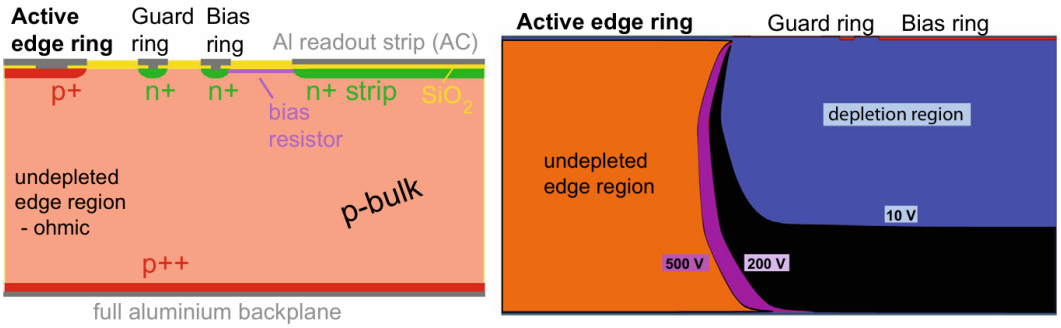

Figure 1.11: The left figure provides a schematic representation of the ring structure at the edge of a n-in-p sensor, while the right figure shows a simulation of the depletion zone extension for different bias voltages (note that for n-in-p sensors, the HV is negative). Taken from [6].

- **Breaks** in the aluminium readout strip, typically caused by processing errors or mechanical damage such as scratches.
- **Shorts**, resulting from unintended connections between neighboring strips. While not critical, they increase noise and can cause multi-strip hits, thereby degrading the position resolution.
- **Leaky strips**, which exhibit high leakage currents and can significantly increase the channel noise. These may result from various causes, such as defective bias resistors, inhomogeneities in the bulk silicon (especially near the surface), faulty implantations, or undepleted regions. This defect usually affects groups of adjacent strips rather than isolated ones.

Most of these defects can be detected electrically through current and capacitance measurements. Sensors arriving at assembly centers, such as IIHE, are generally free from such issues, as manufacturers must perform extensive quality control to meet the required specifications. Nevertheless, careful handling remains essential due to the fragile nature of the sensors.

1.8 Goal of the project

During the assembly of the modules, errors can occur and the sensors can be damaged. Currently, the quality control of the sensors in the modules is performed with a digital microscope in the visible range and by inspecting the electronic characteristics (IV curves), which implies that the sensor is tested with probes. This last method has a drawback, since the probes can also damage the sensor. The goal of this project is to explore the possibility of using a safer way to inspect the sensors with an infrared camera, leveraging the optical properties of silicon. This could help reduce the number of damaged modules by identifying the sources of defects in the production chain, and thus increase the yield. If this project leads to positive results, it could pave the way for the implementation of innovative techniques in the quality control tests along the production chain of such sensors, both at the manufacturer and at the end of the assembly line. Furthermore, some sensors have shown unexplained behavior in the IV curves. This project also aims to better understand the origin of these behaviors.

1.8.1 Transparency of Silicon

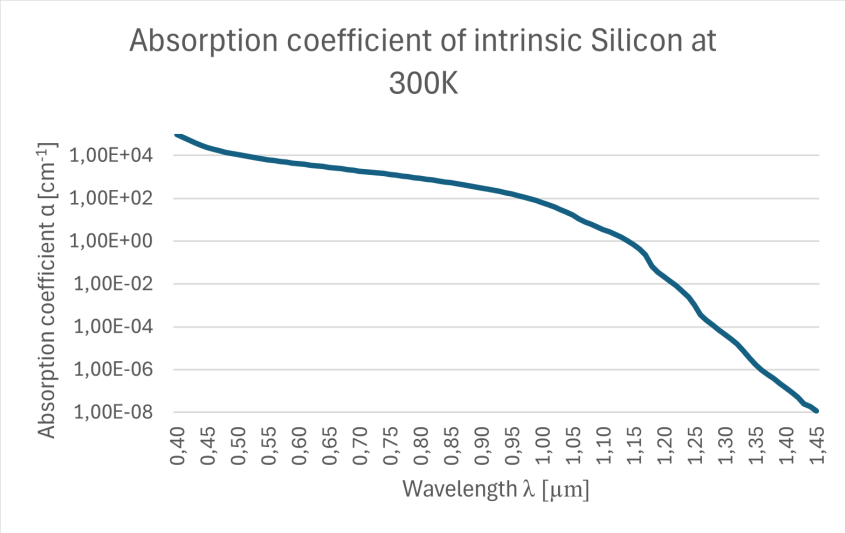

Figure 1.12: Absorption coefficient of intrinsic silicon as a function of the wavelength at 300K. Data taken from [17].

Silicon is a semiconductor material with an indirect bandgap of 1.12 eV at room temperature. This corresponds to a wavelength of 1107 nm, in the infrared range. For photons with energies lower than the bandgap, ideal intrinsic silicon is expected to be completely transparent, since no absorption can occur. Figure 1.12 shows the absorption coefficient in intrinsic silicon as a function of wavelength, and highlights a decrease in this coefficient at energies below the bandgap. As a reminder, light intensity decreases exponentially according to $I(x) = I_0 \exp(-\alpha x)$, where α is the absorption coefficient, x is the propagation distance in the material, and I_0 is the incident intensity.

Since the strip sensor consists of a p-doped substrate with a highly doped p^{++} zone at the aluminium backplane, the absorption coefficients plotted in Figure 1.12 cannot be used as quantitative values, but rather as qualitative information. One does not expect a drastic change in the absorption coefficient for the p^{++} layer (30 μm thick), since the concentration of boron (the dopant) is at most 10^3 times lower than that of silicon [6, p. 4, p. 99], and 10^9 times lower elsewhere.

The aim of this project is to exploit this property to qualitatively analyse the strip sensors using infrared illumination (LEDs in the 850-1200 nm range) and attempt to reveal otherwise invisible structures.

1.8.2 Electroluminescence

A second objective of this work is to use electroluminescence (EL) to reveal defects in sensors. As explained in Section 1.7, the sensors are designed as p-n junctions where a high voltage is applied in reverse bias. However, the sensors can also be operated in forward bias to perform EL, functioning similarly to a Light Emitting Diode (LED). Free carriers recombine in the depletion region and emit photons with an energy close to the bandgap, in the infrared spectrum. This EL signal is proportional to the current density.

This technique is already widely used for defect identification in silicon photovoltaic (PV) cells and has proven to be a powerful tool for detecting cracks and shunts. This is mainly

performed on aged PV modules, but some faults can also arise during the production, transport, or installation stages. [18] provides an overview of the state-of-the-art in EL imaging for solar cells. Figure 1.13 is shown for illustration. Different types of defects and their causes are identified in [19]:

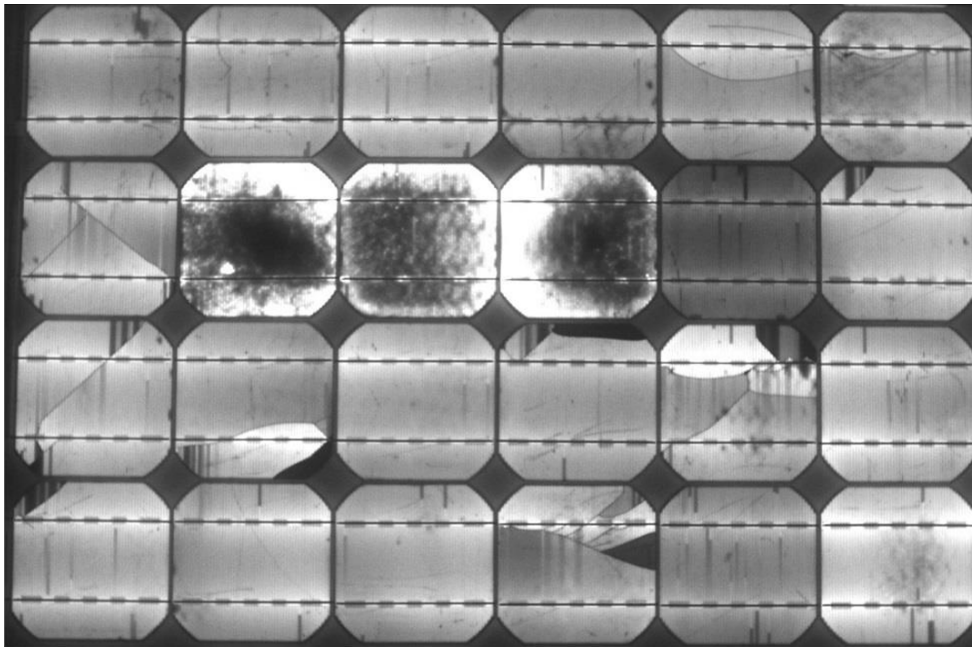

Figure 1.13: EL image of defective monocrystalline silicon photovoltaic module, taken from [18].

- Temperature inhomogeneities arising during the firing process of solar cells at the production stage can lead to a gradient in the contact resistance of the cell-finger metallization[2], typically from the center to the edges of the cell. This results in very bright and dark areas in EL images, such as the three cells in the second row of Figure 1.13. Typical "chain-like" patterns can also arise from the same issue, as seen in the last cell on the right in the fourth row. The finger metallization is comparable to the aluminium strips used in charged particle detectors, but with the difference that they are not connected to the substrate (AC-coupling). For this reason, this particular type of fault is not expected in the CMS sensors.

- A significantly dimmer EL signal, such as that of the fifth cell in the second row, is generally caused by a poor connection to the busbars[3]. In the case of 2S modules, a similar effect could occur due to poor biasing (e.g., a bad connection between the bias terminal, the bias ring, and the implant strips), which would be relevant to identify during the assembly process.

- Isolated interrupted fingers may appear but are considered a marginal defect in solar cells. This can be observed in some cells in the last row of the same figure. This type of fault is comparable to breaks in aluminium strips, as mentioned in Section 1.7.3. However, since biasing in the sensors is done through the implant strips, such patterns in EL images may actually originate from interruptions in the implant strips themselves.

[2]Thin metal lines printed across the surface of a solar cell.

[3]Metallic strips conducting the current generated by the cells, orthogonal to the fingers. Two busbars per cell are visible in Figure 1.13.

- Cracks are also visible in Figure 1.13. They can be either electrically conductive (allowing current to flow through) or insulating (causing dark areas and interrupted fingers). These defects can occur during busbar soldering (resulting in cracks near the busbars), during transport or installation, or due to mechanical impacts. Similarly, silicon sensors for the CMS upgrade are subject to the same risks: cracks can develop during module assembly, wire bonding, transport, or due to accidental impacts. Moreover, during the burn-in test at the end of the assembly line, the modules are subjected to thermal cycling. It is plausible that marginal cracks could evolve into harmful ones, as observed in silicon solar cells due to thermoelastic effects [20].

- Corroded busbars can also be detected via EL imaging, appearing as a dark halo along the busbars. However, no example of this defect is visible in Figure 1.13. CMS sensors are affected by Al_2O_3 corrision after some time under voltage in a humid environment [6, p. 117-118]. EL could therefore be used to detect such corrosion in strip sensors.

Nowadays, research on machine learning techniques for fault diagnosis and defect classification in PV systems yields promising results, paving the way for future automated defect detection and assistance.

Motivated by its success in PV applications, this study seeks to explore the feasibility of applying EL imaging to silicon strip detectors, with the goal of identifying potential defects during production or quality control.

1.8.3 Experimental approach

The objective of this work is to develop an experimental setup capable of exploring both the transparency and electroluminescence (EL) of silicon strip sensors for defect detection using an infrared camera, and to evaluate their potential as a quality control tool in the production chain of the 2S modules for the CMS Phase-2 Upgrade. Chapter 2 presents the design of the constructed experimental setup. Chapter 3 describes the validation of the setup using small silicon solar cells, including the image processing techniques and a discussion of encountered artefacts. Finally, Chapter 4 presents the results obtained from the transparency and EL analyses performed on silicon strip sonsors from both the phase-2 and phase-0 of CMS.

Chapter 2

Design of the experimental Setup

This chapter is dedicated to the design and description of the materials used in the construction of the experimental setup. The objective is to develop a mount equipped with an infrared camera to capture images of strip sensors at different scales. The setup also includes infrared LEDs to investigate silicon transparency, their control system, and a dry-air pneumatic system to prevent deformation of the spacers between the two sensors of a module and to avoid leakage currents.

2.1 The Optical Design

To avoid backgroud noise, the experiments have to be performed in an dark isolated environnement. A light-isolated cabinet is thus selected to accommodate the experimental setup.

2.1.1 The SWIR Camera

The infrared camera used for this work is the Bobcat320-GigE-100 provided with the Xeneth Software for the camera control. Table 2.1 summarizes the features of the camera. The spectral response of the camera lies in the short-wave infrared (SWIR) range. The Gigabit Ethernet (GigE) interface was used to connect the camera to the network at IIHE.

Camera features	
Spectral range	0.9-1.7 µm
Exposure time	0.5-10 ms
pixel size	20 μm^2
Focal plane array	320 x 256
Frame rate	100 fps

Table 2.1: Features of the Bobcat320-GigE-100 camera.

A lens f = 16 mm is provided with a manual focus and iris, a special coating for a sensitivity in the near-infrared (NIR) and a field of view 23°x31°. A set of extention tubes from 0.5 - 40 mm was also available for the magnification the object in the image plane, working on the principle described in Appendix B.

Due to the magnification with the extention tubes, the modules under investigation must be positioned close to the camera. For practical implementation, a vertical imaging setup is chosen, equipped with a height-adjustable mechanism that allows the modules to be brought closer to the camera as needed. This is illustrated on Figure 2.5.

2.1.2 The LEDs for transparency analysis

Multiple LED's with various emission spectrums were selected to inspect the modules with different absorption coefficients, see Figure 1.12 for the absorption coefficient as a function of the wavelength at 300 K. The LED's used are given in Table 2.2.

LEDs reference	Wavelength	Luminous or radiant flux
ILH-OO01-NUWH-SC211-WIR200	400-750 nm	<280 lm
ILH-IW01-85SL-SC211-WIR200	850 nm	1030 mW
ILH-IS01-94SN-SC201-WIR200	950 nm	1130 mW
ILM-IP01-BBEM-SC201-WIR200	650-1050 nm	74 mW
M1200D3	1200 nm	200 mW

Table 2.2: Features of the LEDs. Their typical luminous or radiant fluxes are taken from their respective datasheets.

The white LED (400-750 nm) was selected to illuminate the dark cabinet, providing visual comfort for the operator during manipulations. The 850 nm LED lies outside the spectral sensitivity range of the camera, so no signal is expected. The remaining three LEDs are used for the transparency analysis. Each LED was ordered in duplicate as a precaution in case one gets damaged.

In addition, all LEDs must be mounted on a heatsink to ensure proper thermal dissipation.

2.1.3 The Narrow-Band Filters

Narrow-band filters were placed in front of the last three LEDs listed in Table 2.2 to isolate specific wavelengths corresponding to different attenuation coefficients in silicon. This was necessary because the emission spectra of the LEDs are relatively broad around their nominal wavelengths. The attenuation coefficients presented in this table are not quantitative values directly applicable to the 2S module sensors, as these are not made of intrinsic silicon; rather, a qualitative approach is adopted in this work. The selected filters are listed in Table 2.3, and their transmission spectra are provided in Appendix D.

Narrow band filter reference	Central wavelength λ [nm]	Attenuation coefficient in intrinsic silicon α [cm^{-1}]
FBH950-10	950	156
FBH1050-10	1050	16.3
FBH1200-10	1200	$2.2 \cdot 10^{-2}$

Table 2.3: Central wavelength of the transmission spectrum of the narrow-band filters and the corresponding attenuation coefficent at 300 K, taken from [17].

The addition of optical filters required the design of 3D-printed parts to mount them in front of their corresponding LEDs. This is further explained in Section 2.4.1.2.

2.2 The pneumatic design

A dry-air pneumatic system is required for the storage and operation of the modules. The spacers (also called bridges), shown in Figure 1.6, are made of an aluminum-carbon fiber

composite that is highly sensitive to humidity, which can lead to deformation [21]. Furthermore, according to [22], the sensors are hygroscopic, which alters their electrical properties and results in premature breakdown voltages. Finally, in humid environments, the sensors are affected by Al_2O_3 corrosion after prolonged operation under voltage [6, p. 117-118].

The laboratory is supplied with pressurized air at 8 bar through a valve. The rest of the pneumatic system was designed with the constraint of using as many components already employed at the IIHE as possible, in order to ensure the availability of replacement parts in case of failure. The list and references of the selected components are provided in Appendix E. Figure 2.1 shows the schematic of the designed system.

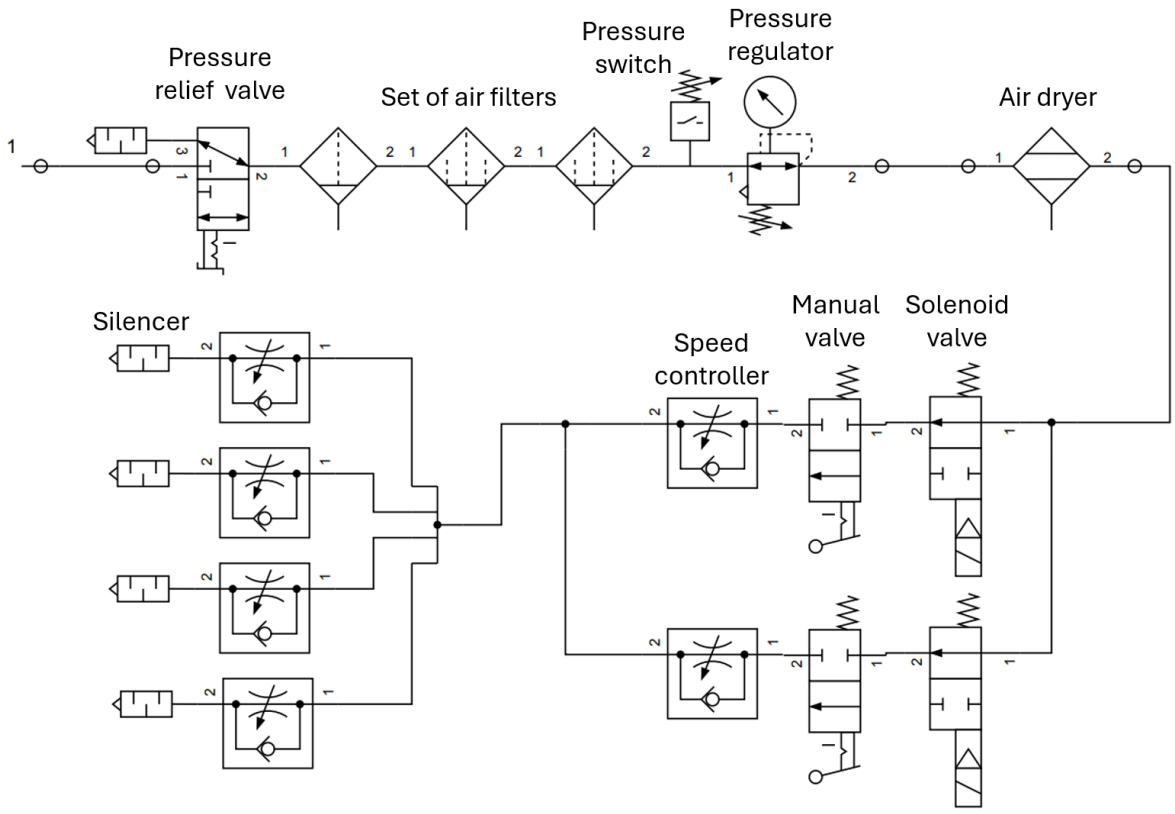

Figure 2.1: Schematic of the pneumatic system.

The pneumatic system starts at the 8 bar valve (the fitting at the top left of Figure 2.1), reaches the dark cabinet through a ±20 m tube, and is connected to an assembly composed of:

- a pressure relief 3-port valve,
- a set of three air filters, removing dust and impurities down to 0.01 µm,
- a pressure switch, intended to be connected to the light controller (see Section 2.3),
- a pressure regulator with an integrated pressure gauge.

The filtered output air then passes through a membrane air dryer with a standard dew point of –40°C and a nominal outlet flow rate of 75 L/min. Thereafter, the system is separated into two parallel branches, each containing a flow controller, a manual valve, and a solenoid valve, intended to be connected to the light controller (see Section 2.3). The branches merge

downstream into a common output, enabling a two-speed operation depending on the selected flow path. The system described up to now was attached on the dark cabinet and is represented on Figure 8 in Appendix E.

The merged tube is then split again into four branches inside the dark cabinet, allowing the diffusion of dry air throughout the enclosure. Figure 9 represent this diffusion system in Appendix E.

2.3 The light controller

In this section, the light controller is described. It is an electronic PCB with a microcontroller that offers great potential for controlling the LED illumination inside the dark cabinet, managing the pneumatic system, and monitoring both temperature and relative humidity.

2.3.1 Description of the light contoller

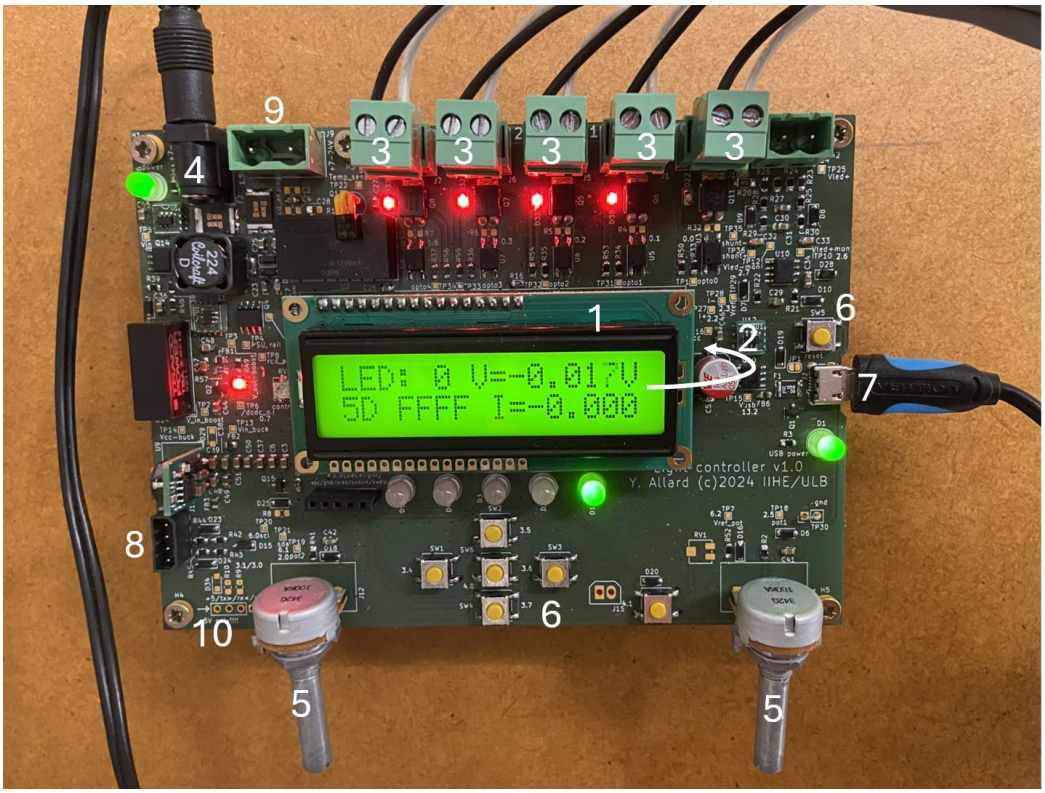

Figure 2.2: The ligth controller.

Figure 2.2 gives an image of the light controller PCB. Its main components are:

1. An LCD screen to display measurements.
2. A programmable microcontroller CY8C4248AZI-L485 form the PSoC 4 family (under the LCD screen).
3. Five screw terminal blocks to suply the 5 LEDs.
4. A 24V power supply.

5. Potentiometers to adapt the supply of the LEDs (one analog and one digital supply).
6. Navigation buttons and reset button.
7. Micro-USB port for serial communication with a computer.
8. Pin header for connection to a miltiplexer PCB connected to 4 temperature and humidity sensors. Images of them are given in Appendix F on Figure 10.
9. Connector for powering the solenoid valves of the pneumatic system (see Section 2.2).
10. Pin header providing the logic output to control the solenoid valves. A driver is required to connect 10 to 9.

2.3.2 Firmware

A part of this work involved programming the microcontroller firmware in C, based on the firmware and graphical user interface (GUI) python code of a previous project carried out at IIHE by Martin Delcourt, in which a PCB with a different design from that of the light controller was used. By contrast, the PCBs shown in Appendix originate from this earlier project. The GitLab repository is available at the following link: ir-camera.

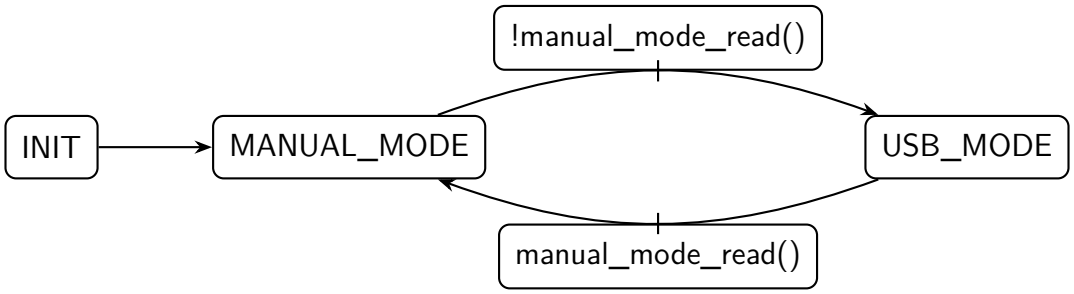

Figure 2.3: Main state machine.

The firmware is structured around a main state machine, as illustrated in Figure 2.3. It operates in two primary modes:

- **Manual Mode**: In this mode, the user can control the LEDs using the onboard navigation buttons and potentiometers. This allows for direct adjustment of LED intensity and selection without the need for a computer.
- **USB Mode**: In this mode, the microcontroller was intended to communicate with the GUI on a PC, enabling real-time monitoring and control. The GUI was designed to display measurements such as the temperature and relative humidity inside the cabinet, as well as the voltage, current, and temperature of each LED. It was also meant to provide control over the solenoid valves from the PC. However, this communication mode could not be made functional during the project. Therefore, the decision was made to operate fully in manual mode to save time and focus on the main objective of this work: the transparency and electroluminescence analysis of the strip sensors. Consequently, its potential could not be explored.

The transition between modes is triggered by pressing the `manual_mode` button on the controller.

The USB communication (serial driver) was intended to be managed by the state machine shown in Figure 2.4. Each state corresponds to a specific action to be performed by the microcontroller, which is initialized in the `NOTHING` state. At each iteration of the main loop in USB mode, the microcontroller reads a command signal from the serial port. If this command is not zero, it switches the state to perform the requested action sent by the PC: sending measurement data, synchronizing the microcontroller with the PC, or transmitting configuration data. Other commands that do not change the `NOTHING` state are used to maintain proper communication with the PC and help with debugging.

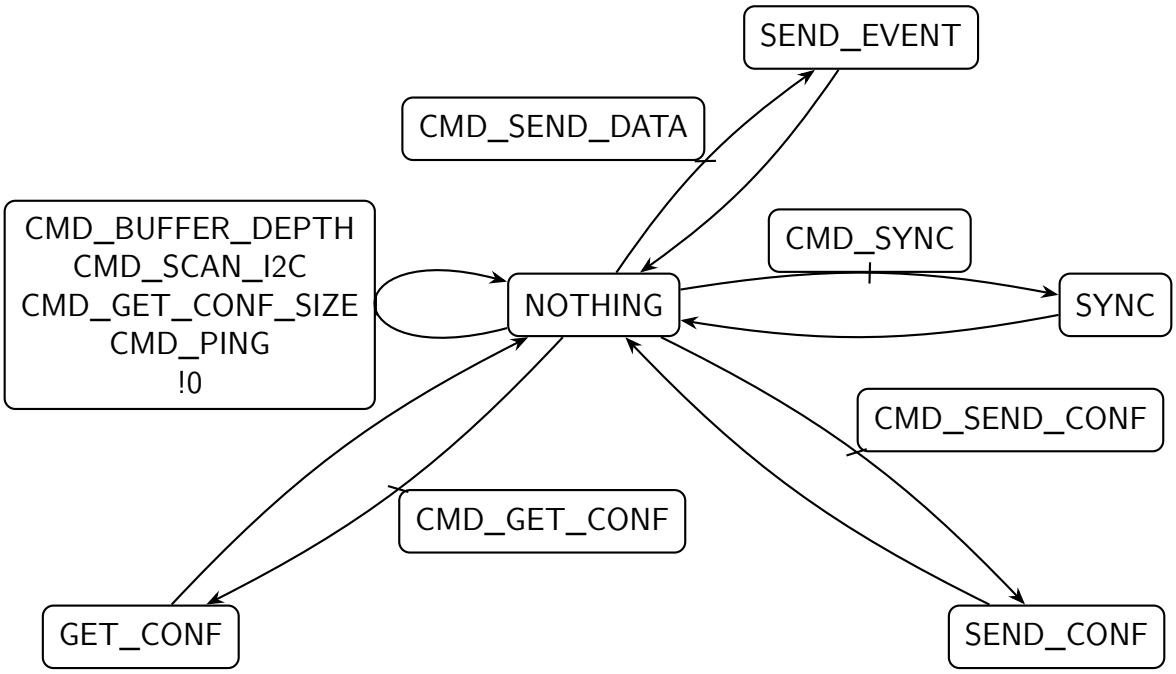

Figure 2.4: State machine of the USB serial communication.

On the PC side, the Python code manages the GUI (a screenshot of which is provided in the Appendix G) and the serial communication. Unfortunately, in the current state of the code, the `CMD_PING` command is received by the microcontroller and its response is successfully received by the PC, but no other commands appear to reach the microcontroller afterward. The cause of this issue has not yet been identified.

2.4 The mechanical design

The experimental setup is shown in Figure 2.5, where the following components can be identified:

1. **The IR camera** is mounted onto the structure using a custom 3D-printed bracket.

2. **The frame** is built from 40 mm × 80 mm dark-coated aluminum C-Beam linear rails. The dark finish helps minimize unwanted photon reflections. This modular rail system allows for flexibility, making it easy to adjust the positions of both the camera and the LEDs to test different configurations.

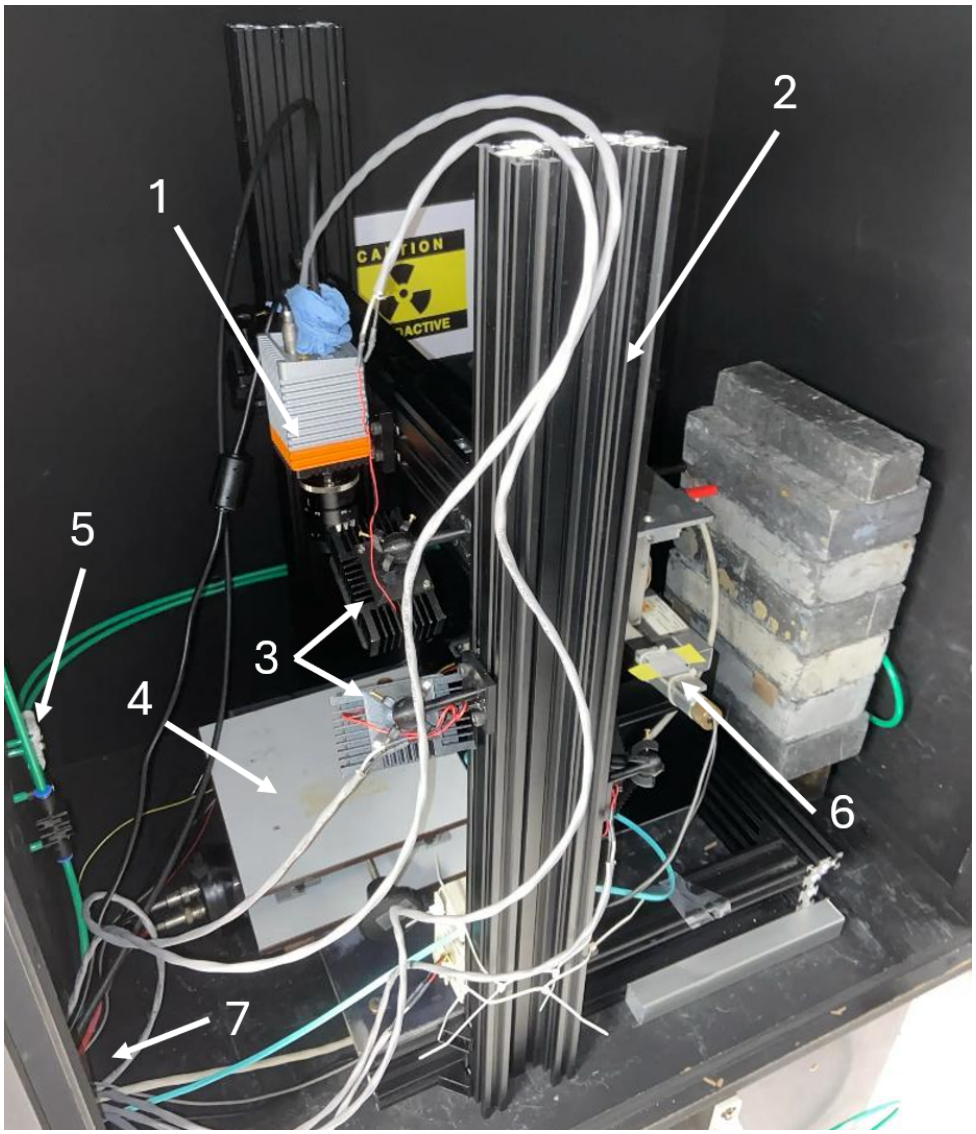

Figure 2.5: Experimental setup disposed in the light-isolated cabinet.

3. **LEDs**, each mounted on a heatsink to ensure proper thermal dissipation, are fixed to the structure using 3D-printed mounts. In addition, the optical filters are housed in 3D-printed caps positioned in front of the corresponding LEDs and attached directly to the same heatsinks (see Section 2.4.1.2).

4. **A scissor lift table** is used to adjust the vertical position of the sample, enabling fine control of its distance from the camera.

5. **The pneumatic system** inside the dark cabinet continuously supplies dry air. This is particularly important to maintain the integrity of the spacers glued between the two sensors of the 2S modules.

6. **A second experimental setup** involving a radioactive source was installed in the same dark cabinet for a separate project. This introduced several constraints:

    - Operations inside the cabinet had to be minimized to reduce exposure to radiation.

- A configuration had to be found that allowed both experiments to coexist. For example, the electron gun from the second experiment was placed under the lift table, necessitating the addition of a plexiglass plate in between.
- A fan required by the second experiment had to be mounted onto the rail structure to keep it out of the IR camera's field of view.
- Fragile cables had to be carefully routed outside the camera's field of view and kept away from the lift mechanism to avoid being damaged by the scissor action.

These constraints made manipulations more delicate and demanded extra care when handling fragile sensors. Furthermore, the operation of the electron gun prevented both experiments from running simultaneously.

7. **An opening** in the dark cabinet allows the passage of cables, tubes, and air. It is sealed as much as possible with dark tape to prevent external light from entering the cabinet.

2.4.1 3D Parts

Some 3D-printed components were necessary to assemble certain parts of the setup.

2.4.1.1 Camera Mount

First, the camera needs to be mounted onto the frame. Figures 2.6 and 2.7 show the top and bottom views of the designed 3D-printed mount.

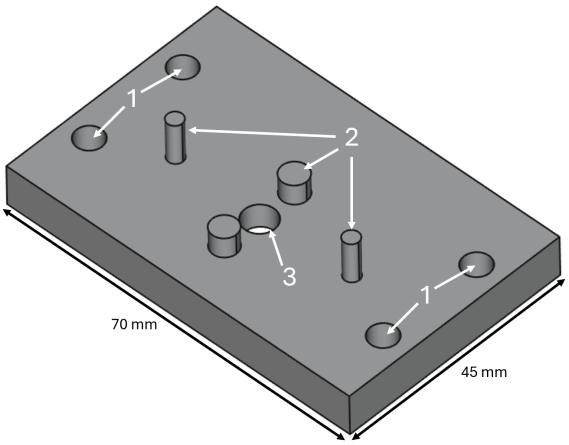

Figure 2.6: Top view of the camera mount.

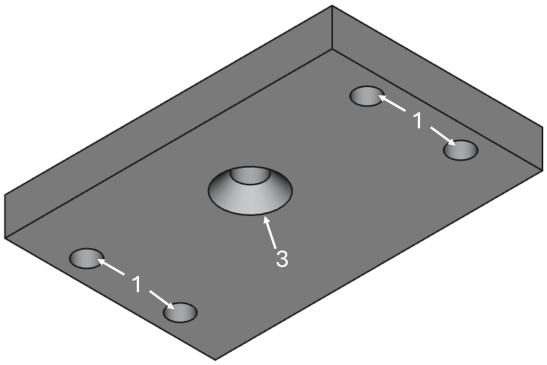

Figure 2.7: Bottom view of the camera mount.

The following features can be identified:

1. **Four mounting holes** designed for M5 screws to fasten the part onto the frame.
2. **Four extruded pins** designed to fit into the holes on the bottom of the camera, preventing rotation and ensuring correct positioning.
3. **A central hole**, countersunk, designed for an M6 screw to secure the mount to the camera.

2.4.1.2 Filter Caps

These parts were designed to hold the narrow-band filters in front of the LEDs and ensure proper sealing to block unwanted photons (i.e., photons with undesired wavelengths) emitted by the LEDs. The caps are designed to be mounted directly onto the LED heatsinks. Figures 2.8 and 2.9 show top and bottom views of these components.

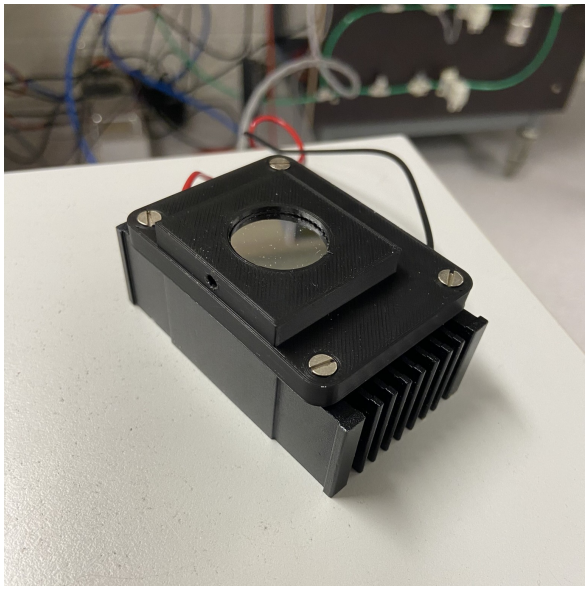

Figure 2.8: Top view of a filter cap mounted on a heatsink.

Figure 2.9: Bottom view of a filter cap with its O-ring.

The narrow-band filter can be inserted into the cap through a side slot. This slot is precisely sized to the filter's dimensions to prevent photon leakage. On the opposite side, a small pinhole (visible in Figure 2.8) allows the filter to be pushed out using, for example, an Allen key.

On the back of the part (see Figure 2.9), a groove is provided to accommodate an O-ring, ensuring a tight seal between the cap and the heatsink. Additionally, serpentine-shaped grooves allow the LED cables to pass through while minimizing light leakage from the interior of the cap.

Different designs were created depending on the cable positioning or the dimensions of the optical filter.

2.4.1.3 Articulated mounting arm for LEDs

An articulated mounting arm was designed to secure the illumination system to the structure and to allow control of its orientation. Figure 2.10 shows the articulated system, which consists of two parts: the arm and the clamp.

The arm is attached to the frame with screws. A small extruded pin is provided to tie the LED cables, which helps prevent accidents in case the cable is accidentally pulled elsewhere in the cabinet. The arm ends with a sphere onto which the clamp is mounted.

The clamp is screwed onto the heatsink. Two of its four fingers are equipped with screws that apply pressure on the spherical end of the arm, keeping the system securely in place. The illumination direction can thus be adjusted easily.

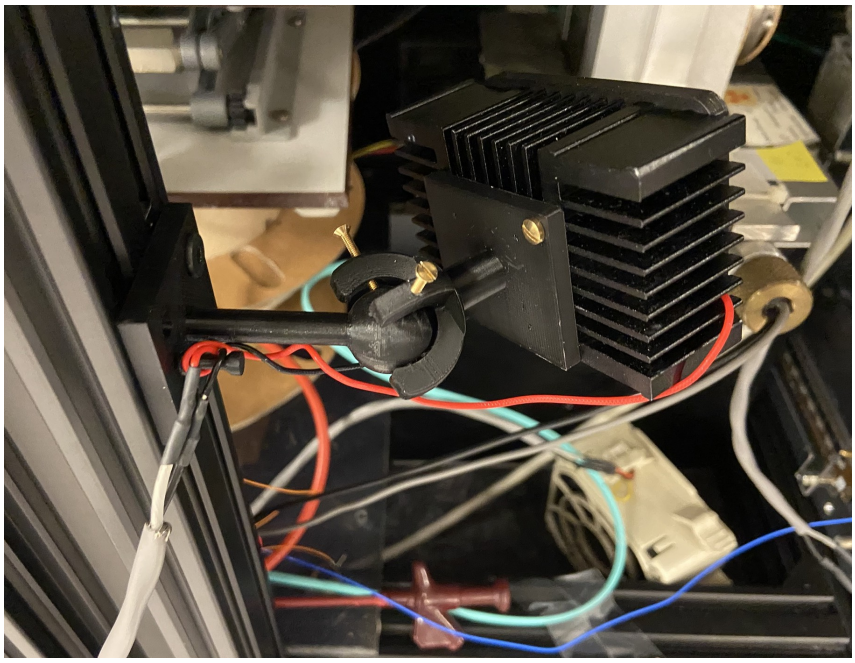

Figure 2.10: Articulated mounting arm for an LED, attached to the frame.

Chapter 3

Operation and validation of the experimental setup

In this chapter, the first part focuses on the image processing required to obtain and effectively analyze proper IR images, followed by a discussion of the encountered artefacts. The setup is then validated for both transparency and EL analysis through tests conducted on small silicon solar cells, assessing its performance in meeting the objectives.

3.1 Image processing

Images are captured and saved in 16-bit PNG format using the Xeneth software provided with the IR camera. In each raw image, every pixel is encoded with a value ranging from 0 to 65,535, depending on the camera's exposure time, aperture, and gain. Some image processing is required to adjust contrast and reduce noise. This was performed using Python methods developed with the Pillow library.

3.1.1 Grayscale mapping

A histogram represents the distribution of these pixel values, showing the number of pixels at each intensity level [23, p. 37-52]. It is used to determine the range of values present in the image and can help adjust the contrast by mapping the grayscale to a selected value range. Figure 3.1 shows the histogram of a typical image captured during a test described in this chapter. Typically, the pixels with the lowest values (forming the beginning of first peak) correspond to background noise.

The grayscale mapping is performed by selecting a specific range of values from the histogram and generating a new image by rescaling this range to the 0-65,535 interval. Two methods were developed: an automated method and a manual method.

The automated method selects the range from the lowest to the highest pixel value in the image. This is useful for processing an entire repository of images at once. However, it does not work effectively for images containing isolated high pixel values (e.g., a reflection of the illumination on a specific part of the image) and therefore may fail to map the grayscale optimally.

The manual method allows the optimal range to be chosen manually, generally starting slightly above the lowest pixel value (to discriminate noisy background pixels) and, if necessary, saturating isolated high pixel values. This method yields better results but is time-consuming,

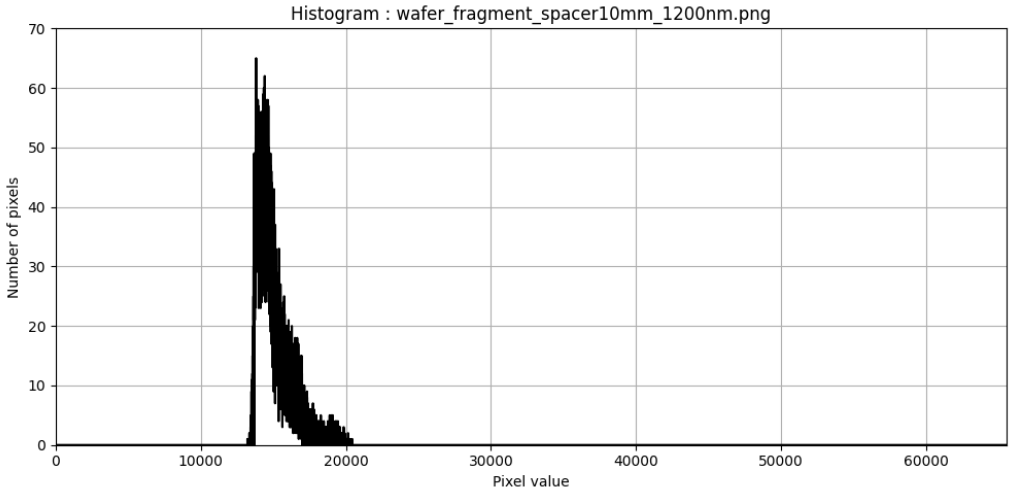

Figure 3.1: Histogram of the unprocessed+ IR image `wafer_fragment_spacer10mm_1200nm.png`. The corresponding image is given in Figure 3.2a.

as each image must be processed manually by plotting the histogram and iteratively selecting the appropriate range.

An example of the mapping of the grayscale is provided on Figure 3.2a and 3.2b.

3.1.2 Convolution filters

Convolution filters were implemented to sharpen images or detect edges. As explained in [23, p. 87-116], for two discrete two-dimensional functions I and H, the convolution operation is defined as

$$I'(u,v) = \sum_{(i,j)\in R_H} I(u-i, v-j) \cdot H(i,j) \tag{3.1}$$

with R_H denotes the range of the variables i, j depending on the dimensions of H. This operation is applied to image arrays I with different convolution kernels H depending on the wanted filter. Two kernels were used and are given in Table 3.1.

1	1	1
1	-8	1
1	1	1

Edge detection kernel

0	-1	0
-1	5	-1
0	-1	0

Sharpening kernel

Table 3.1: Convolution kernels used for image processing.

Figure 3.2 shows the processing of the image of a wafer fragment originating from the same wafer as a p-in-n strip sensor. A picture of this sample is provided in Appendix 3.7.

The edge detection filter (Figure 3.2c) highlights rapid intensity changes, enhancing contours, while uniform regions appear dark. However, noise is also amplified, which explains the speckled background pattern and makes it difficult to distinguish small structures.

In contrast, the sharpening filter (Figure 3.2d) appears to yield better results, revealing sharp structures and making the original image less blurry. A speckled background pattern is also present, but it is less problematic than with the edge detection filter.

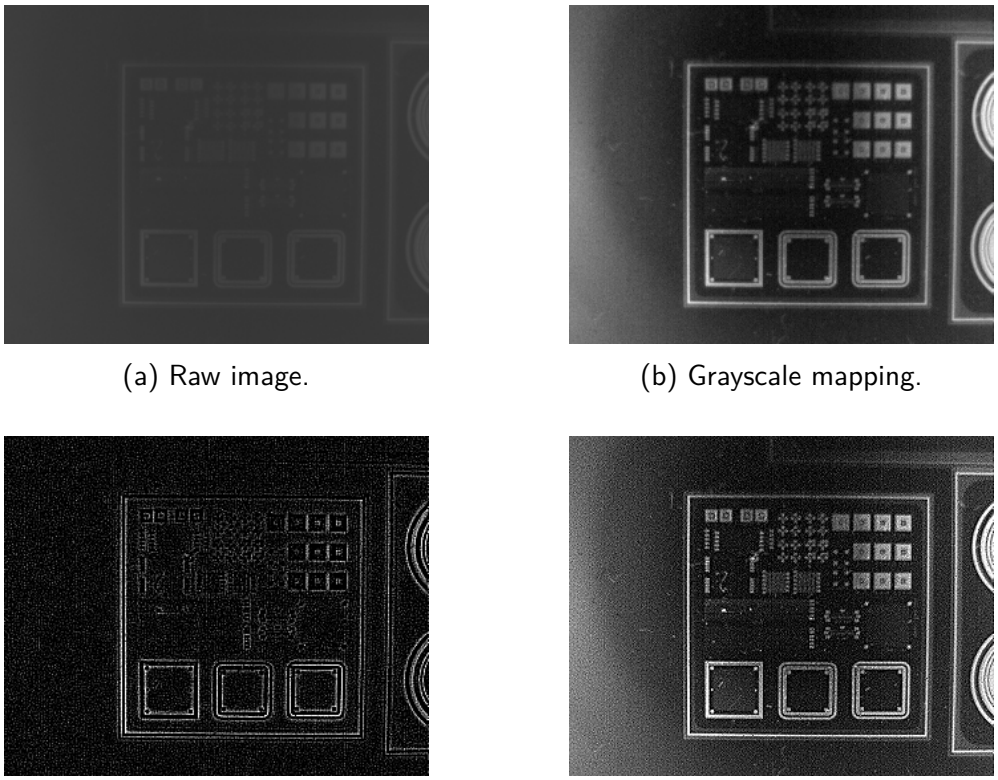

(a) Raw image.

(b) Grayscale mapping.

(c) Edge detection filter.

(d) Sharpening filter.

Figure 3.2: Processing of an IR image of a silicon wafer fragment illuminated with a 1200 nm LED.

3.1.3 Processing of captures

The camera exposure time is limited to 10 ms, which is restrictive when working with low signals. However, the software allows the capture of multiple images, letting the user choose the number of frames to record. These can then be processed to improve the signal.

Let us take the example of capturing 100 images during the electroluminescence of a phase-0 strip sensor with a current of 100 mA (see Chapter 4 for further details on this sensor). This example is illustrated in Figure 3.3. Even after applying grayscale mapping, the signal remains barely visible in a single frame because it is too small compared to the background noise.

A set of 100 empty images (without signal/EL), referred to as the empty capture, is then acquired. Each empty image from the empty capture is subtracted from the corresponding image in the first capture, almost completely removing the background noise.

The 100 resulting images are then summed together: correlated pixel values accumulate to construct the signal, while uncorrelated pixels (residual background noise) fluctuate, resulting in lower pixel values. Grayscale mapping can then be applied to obtain a clearer image. This technique is effective provided the signal is sufficiently strong compared to the camera's background noise.

3.1.4 Artefacts

Some artefacts were encountered, degrading the quality of the images and limiting the performance of the setup. This section lists and illustrate these artefacts.

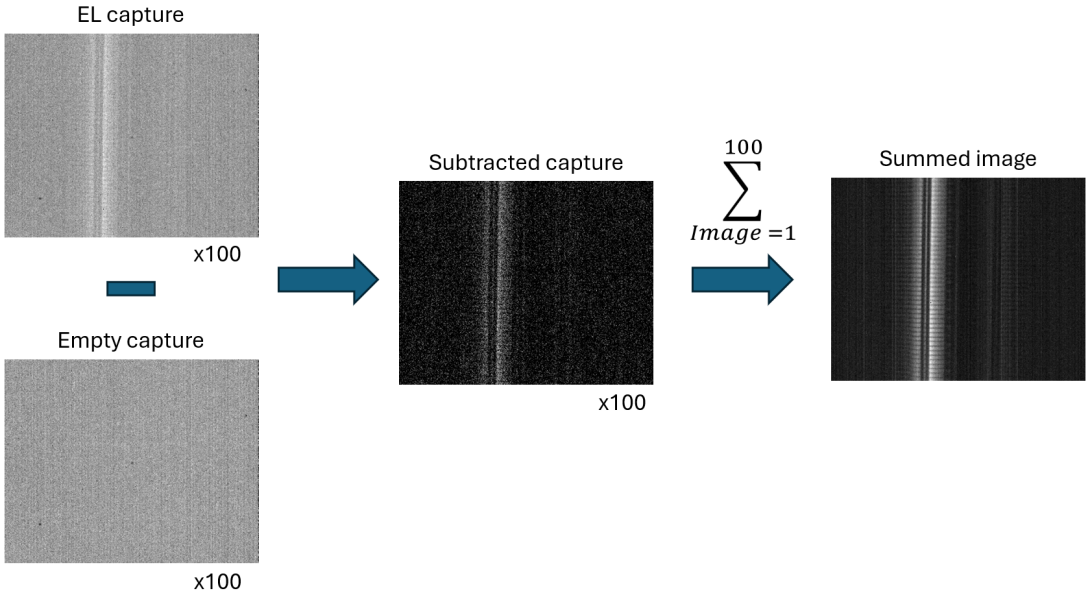

Figure 3.3: Example of image processing from a 100-frame EL capture at the edge of a phase-0 sensor under an applied current of 100 mA.

3.1.4.1 Reflections

Reflections on the sensors were encountered, saturating some pixels and rendering them unusable for transparency analysis. This was the most common artifact, requiring the optimization of the illumination configuration to minimize the issue. Different types of reflections were observed:

- In Figure 3.4a, reflections of the illumination on metallic structures such as the sensor edges are visible.
- In Figure 3.4b, the reflection of the camera lens image on the aluminium backplane is visible.
- In Figure 3.4c, a periodic reflection pattern appears on the sensor. The aluminium strips of the sensor act as a diffraction grating, generating Bragg reflections. By rotating the sensor so that the strip axis is aligned with the direction of the illuminating light rays, this pattern disappears.

3.1.4.2 Chromatic aberrations of the lens

The refractive index of optical materials varies with the wavelength of the propagating light. This also applies to the camera lens and is known as chromatic aberration [24]. Figure 3.5 illustrates this effect. The focus was adjusted using illumination at 1200 nm. The farther the wavelength from 1200 nm, the blurrier the image becomes. This occurs because the focal plane for one wavelength does not coincide with that of another. The only way to overcome this problem is to fine-tune the focus each time a different LED is used.

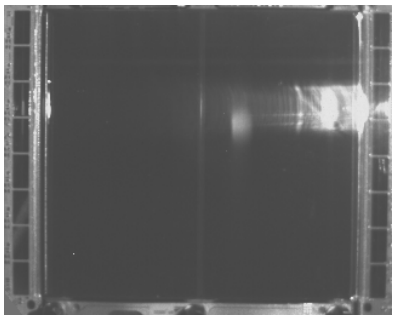

(a) Reflection on the metallic edges of strip sensors.

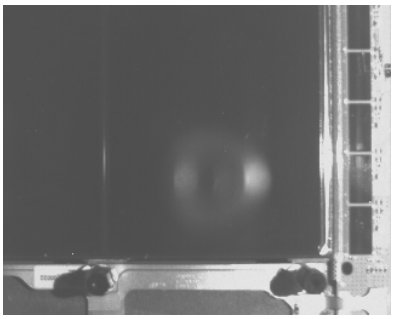

(b) Reflection of the lens of the camera on the aluminium backplane of a strip sensor.

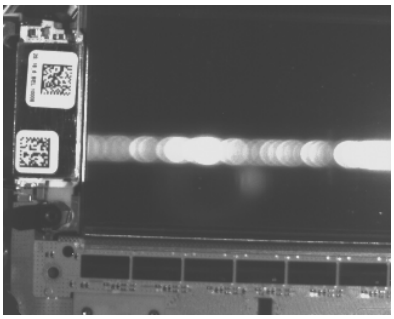

(c) Bragg reflections on the grating of aluminium strips.

Figure 3.4: Reflection artefacts on strip sensors with a 1200nm illumination.

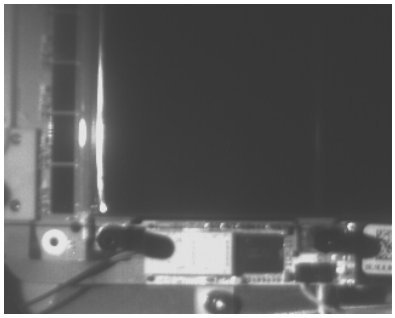

(a) 950 nm illumination.

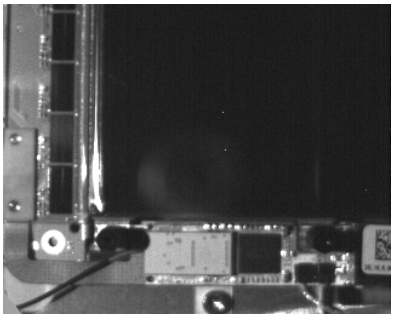

(b) 1050 nm illumination.

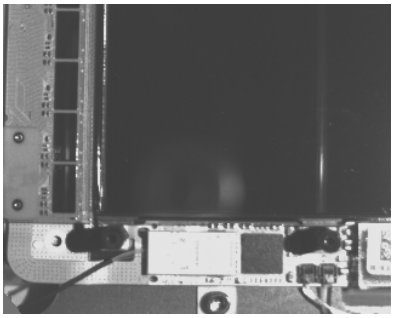

(c) 1200 nm illumination.

Figure 3.5: Illustration of the lens chromatic aberrations as a function of wavelength. Focus adjusted using illumination at 1200 nm.

3.2 Validation of the pneumatic system

Measurements of the relative humidity showed that an RH level of 10% was reached inside the light-isolated cabinet, which is sufficient for both the storage and operation of the silicon strip devices [6, p. 63]. These measurements are given in Appendix H.

3.3 Potential for transparency analysis

This section is focused on the evaluation of the potential of the setup to reveal defects in strip sensors leveraging the transparency of silicon in the near infrared region. This is done by performing some tests on lowcost small silicon solar cells or on a wafer fragment.

3.3.1 Transparency in transmission

Two tests were performed to evaluate the potential of revealing defects by transmission. In this configuration, the sample is placed between an LED source and the camera, allowing light to pass through the sample.

3.3.1.1 Transmission experiment on a scratched solar cell on the metallic backplane

For this first test, a small silicon solar cell available at IIHE, with an aluminium backplane (similar to strip sensors), was used. Aluminium is known to have very high reflectance in the explored IR region [25], so no transmission was expected through the aluminium layer. This was indeed confirmed experimentally.

To verify that silicon is sufficiently transparent in the considered IR region, the aluminium backplane of the solar cell was scratched until the silicon layer was almost reached, as shown in Figure 3.6a. The cell was then positioned with the scratched region between the LED and the camera, equipped with a 10 mm extention tube. The test was performed using the three IR LEDs, positioning the cell on the filter cap with its backplane oriented toward the LED.

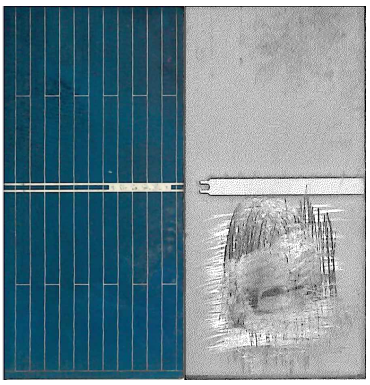

(a) Front and back sides of the scratched solar cell.

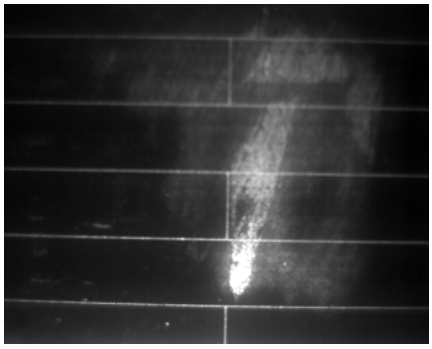

(b) Transmission at 950 nm.

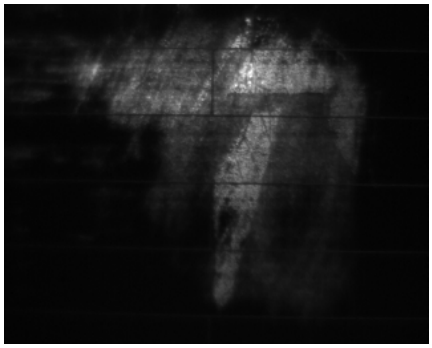

(c) Transmission at 1050 nm.

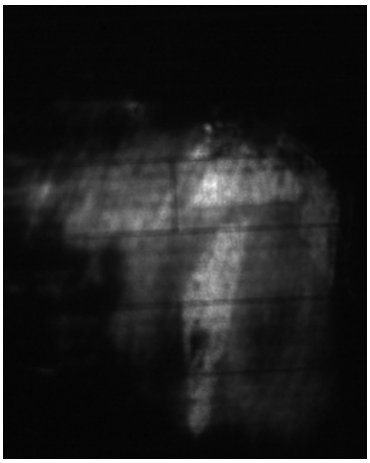

(d) Transmission at 1200 nm.

Figure 3.6: Transmission experiment on a silicon solar cell scratched on the aluminium backside. IR images taken with a 10 mm extension tube.

The results of this experiment are shown in Figure 3.6. A bright shape, very similar in Figures 3.6c and 3.6d, is observed, while Figure 3.6b shows slight differences. These variations arise from the inhomogeneous illumination of the LEDs, which makes the experiment difficult to reproduce exactly.

In addition, the solar cell does not fully cover the opening of the filter cap, allowing some light to pass beside the cell (visible in Appendix I). This introduces a risk of back-reflections that are difficult to control. Despite these factors, the transmitted light pattern remains

broadly similar across all images.

Similar patterns are also visible on the back side of the solar cell, confirming that IR light passes through silicon with minimal absorption, demonstrating its transparency in this spectral range.

Appendix I also shows a picture of the same experiment performed with the white LED. At first glance, no visible light is transmitted within the sensitivity range of the human eye under normal room lighting conditions.

3.3.1.2 Transmission experiment on a wafer fragment

Given the results obtained with the solar cell in the previous section, one can expect similar behaviour if the aluminium backplane of a strip sensor is damaged. To approach the conditions of a strip sensor more closely, a transmission experiment was carried out on a wafer fragment originating from the same wafer as a phase-0 p-in-n strip sensor of CMS. Further information about these sensors is provided in Chapter 4. A picture of the fragment is shown in Figure 3.7. Such fragments are not handled and stored as carefully as strip sensors and are therefore potentially more prone to defects such as scratches or cracks.

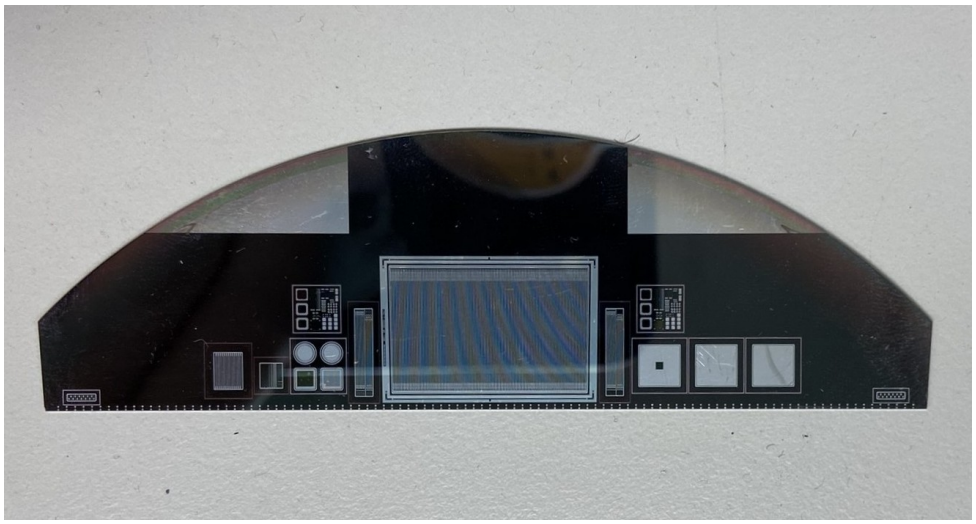

Figure 3.7: Wafer fragment from the same wafer as a phase-0 p-in-n strip sensor.

The structures visible on wafer fragments are intended for quality control by the manufacturer, and their precise composition is, in this case, unknown. However, the composition of phase-2 upgrade wafers is known, allowing some assumptions to be made: the backside layer and strip-like patterns are made of aluminium. At the centre of this fragment, a strip-like structure (hereafter referred to as "baby sensor") is present. This region was inspected in transmission using the same configuration as in the previous section.

Figure 3.8 presents the results of this experiment. The three wavelengths yield different observations:

- **950 nm** (Figure 3.8a): A corner of the baby sensor is visible, with a bright halo in the top-left corner. This result should be interpreted cautiously: a slight lateral shift of the LED under the fragment causes the signal to vanish completely. A plausible hypothesis is that light is bypassing the fragment and being reflected onto the structure. This is supported by the fact that metallic edges appear bright, whereas true transmission through the aluminium layer would yield dark edges due to aluminium's high reflectance.

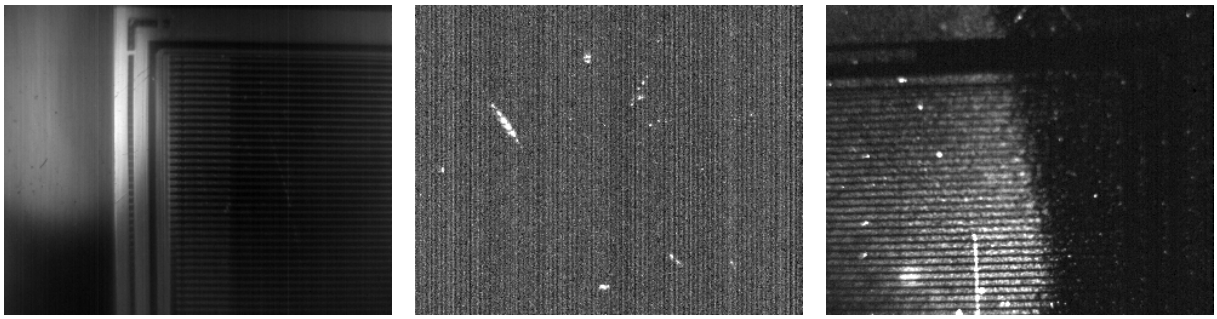

(a) Transmission at 950 nm. (b) Transmission at 1050 nm. (c) Transmission at 1200 nm.

Figure 3.8: Transmission experiment on the strip-patterned part of the wafer fragment.

- **1050 nm** (Figure 3.8b): The image was taken at the centre of the baby sensor. Only a very weak signal is detected, close to the camera's background noise. The few bright points can be interpreted as defects such as pinholes and small scratches in the aluminium backplane, allowing light to pass through.
- **1200 nm** (Figure 3.8c): This case appears intermediate between the previous two. The strip pattern is faintly visible along with bright spots. Here, the edges appear dark, suggesting a downward illumination. Although not fully understood, one possible explanation is partial light transmission through the aluminium layer. The bright spots again highlight pinholes and scratches in the backplane.

Unfortunately, such an experiment cannot be applied at every stage of 2S module production. This is because the modules consist of two parallel sensors, and the high reflectance of aluminium prevents transmission-based inspection through stacked sensors. From the moment the bare module is assembled (see Figure 1.8), this technique offers no practical utility.

3.3.2 Transparency in Reflection

Since sensors of assembled modules cannot be investigated in transmission, another way to assess the transparency of silicon is by illuminating the sensors from the top side and capturing the reflected light with the camera. An investigation of this technique is performed on solar cells.

3.3.2.1 Reflection experiment on a solar cell with a scratched metallic backplane

For a first reflection experiment, the same solar cell as in Section 3.3.1.1 was used.

The solar cell was investigated under IR illumination with the highest magnification possible for the camera (i.e., with a 10 mm extension tube). This magnification has a drawback, as the sample must be placed very close to the lens to be in focus, making it difficult to obtain uniform illumination given that the lens can shadow parts of the field of view. As a result, the signal is weaker and an optimal configuration is hard to achieve, requiring side illumination of the sample.

Figure 3.9 summarizes the results of this experiment, showing the same view of the cell as in Figure 3.6. No significant defects are visible in Figures 3.9a and 3.9b. In Figure 3.9c, a faint dark pattern, similar to the one revealed in transmission, can be discerned, but it remains weak. Overall, this experiment did not succeed in efficiently revealing backplane damage. A

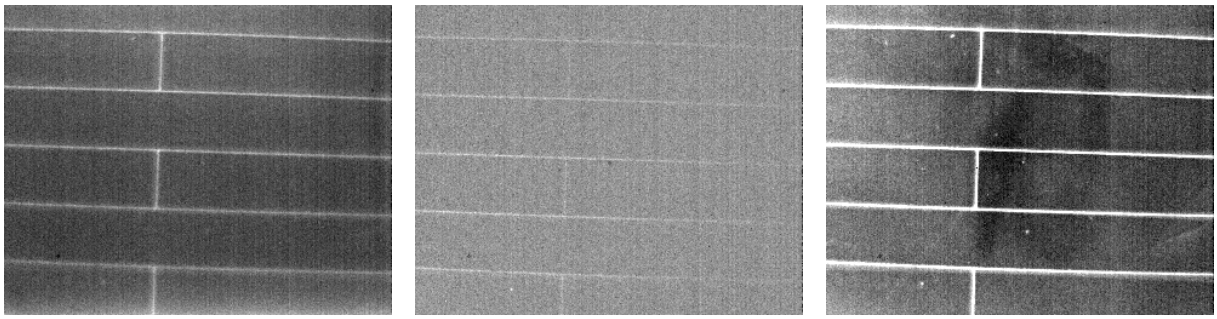

(a) Illumination at 950 nm. (b) Illumination at 1050 nm. (c) Illumination at 1200 nm.

Figure 3.9: Reflection experiment on the scratched silicon solar cell. Images taken with a 10 mm extension tube.

possible follow-up would be to repeat the experiment using a 5 mm extension tube to improve illumination, but this was not carried out.

3.3.2.2 Reflection experiment on a solar cell with cracks

To further explore the potential of this technique, a solar cell of the same type as the scratched one was intentionally damaged by impact. The same experiment was then repeated with a smaller magnification (5 mm extension tube), allowing the sample to be in focus at a slightly greater distance from the lens, which enabled better illumination.

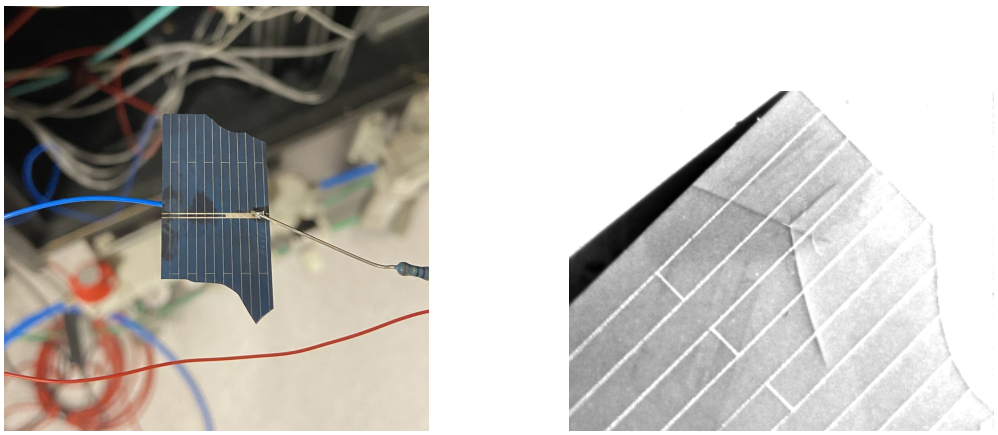

(a) Damaged solar cell.

(b) Illumination at 1200 nm of the top-left corner of the cell shown in Figure 3.10a. Image taken with a 5 mm extension tube.

Figure 3.10: Reflection experiment on a damaged silicon solar cell.

Figure 3.10 shows a picture of the damaged cell and the reflection experiment under 1200 nm illumination. As can be seen, cracks are visible under IR illumination, whereas they are not apparent in the visible range.

This is a promising result for using this technique to reveal cracks in silicon sensors.

3.3.3 Discussion on Illumination

The experiments demonstrated that silicon is indeed transparent at the three wavelengths considered, showing only minor variations in this property. However, since the absorption coefficient of silicon is lower at 1200 nm, this LED is often preferred to minimize the focus adjustments required between experiments due to chromatic aberrations.

It is also noteworthy that, given the emission spectrum of the LED filtered at 1050 nm (shown in Appendix C), a significant portion of the light is blocked by the narrow-band filter (see Appendix D). This reduces the efficiency between the power injected into the LED and the luminous power exiting the filter.

Finally, if transmission transparency becomes a consideration in the future—particularly to improve the homogeneity of sample illumination—implementing Köhler illumination [26, p. 155-156] could be a potential improvement. However, this would represent an additional technical challenge.

3.4 Potential for electroluminescence analysis

The goal of this section is to ensure that the setup is capable of capturing EL from small solar cells and effectively detecting failures before attempting the procedure on charged-particle detectors.

3.5 EL experiment on a solar cell

In this first experiment, the objective is to demonstrate that the setup can capture the EL emission of a small solar cell.

The solar cell (shown in Figure 3.11a) is connected in series with a resistor and forward-biased using a battery. The current flowing through the cell is 8.7 mA. Assuming the current is uniformly distributed across the solar cell, the current density is about 19,07 μA/mm^2. The experiment was performed without the use of spacers.

(a) Picture of the 12 mm × 38 mm solar cell and its battery.

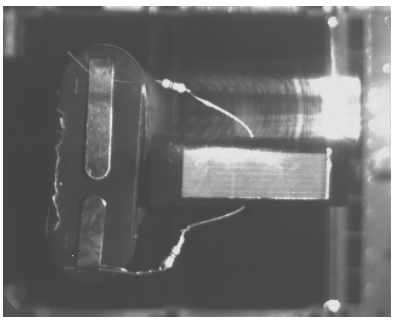

(b) Illuminated view.

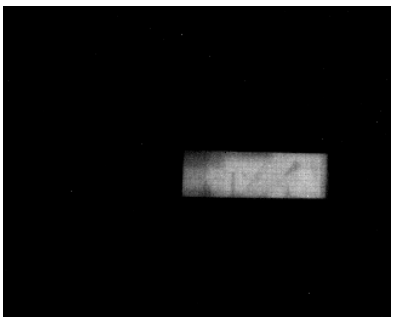

(c) EL of the solar cell.

Figure 3.11: Electroluminescence experiment on a small solar cell.

As shown in Figure 3.11c, EL emission was successfully captured. A gradient of EL intensity is visible on the right side of the cell, along with some darker spots. This can be interpreted

as an inhomogeneous distribution of current across the cell.

3.5.1 EL for defect detection in a small solar cell

This section focuses on defect detection in solar cells using the EL technique.

3.5.1.1 EL of a scratched solar cell on the metallic backplane

Using the scratched solar cell, the device was forward biased and supplied with a current of 70 mA. The result of this experiment is shown in Figure 3.12.

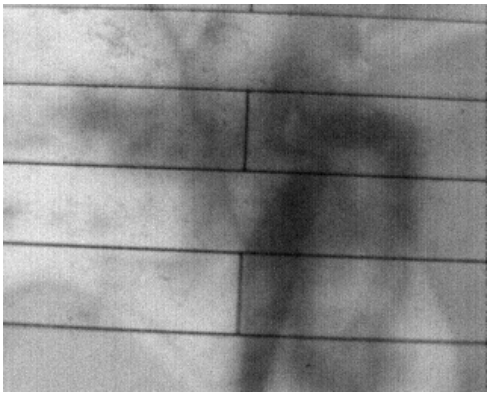

Figure 3.12: EL image of the scratched solar cell on the metallic backside, forward biased at 70mA, acquired with a 10mm spacer.

The pattern appearing bright in transmission (see Figure 3.6) appears dark in the EL image. The scratched backplane does not conduct current effectively in this area, leading to reduced EL emission.

These observations indicate that the EL technique allows detection of backplane defects.

3.5.1.2 EL of a solar cell with cracks

The same damaged cell as in Figure 3.10 was also investigated using EL.

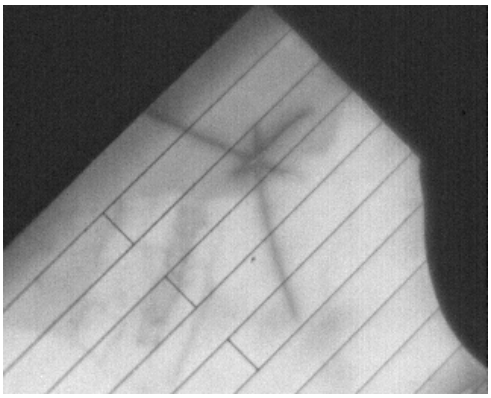

(a) EL in forward bias with a current of 50 mA.

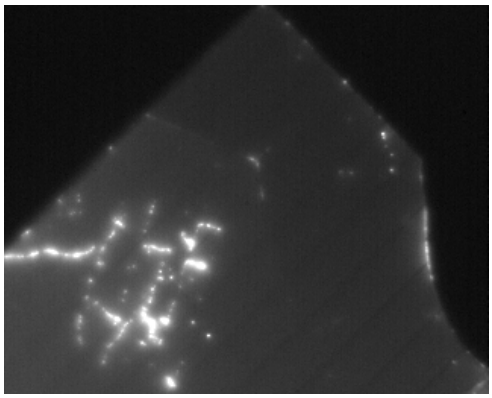

(b) EL in reverse bias with a current of 150 mA.

Figure 3.13: Electroluminescence experiment on a solar cell with cracks. Images taken with a 5 mm extension tube.

In Figure 3.13a, the cell is forward biased and supplied with a current of 50 mA. As in the transparency experiment, the cracks are visible. This indicates that the technique has potential for application to strip sensors.

Interestingly, when the cell is reverse biased with a higher current, some defects are also revealed through EL emission, as shown in Figure 3.13b. Bright spots and lines appear in the image.

Defects or impurities in the silicon bulk introduce energy levels within the forbidden bandgap (deep levels or traps). Carrier transitions involving these deep levels dominate and are known as Shockley-Read-Hall processes. For a reverse bias voltage V_{bias} greater than the full depletion voltage V_{FD}, thermally generated electron-hole pairs contribute to a leakage current. This leakage current is an undesired effect in strip detectors [6, p. 3-16].

The bright spots in Figure 3.13b can thus be interpreted as regions with a higher impurity or trap concentration N_t (such as dislocations), leading to an increased leakage current ($I_{\text{leakage}} \propto N_t$) [6, p. 15].

Another hypothesis is that these emissions occur at the metal-semiconductor contact rather than in the silicon bulk, and thus operate on the principle of a Schottky diode.

In conclusion, EL is a promising technique for detecting defects on the backplane, inhomogeneities in current density, cracks, and regions with high impurity concentrations in CMS sensors. By comparison, defect detection based on the transparency of silicon in the near-infrared range is less effective and less promising, as transmission analysis is not feasible for assembled modules, and in reflection mode, defects on the backplane were not clearly identified.

Chapter 4

Experimental results and discussion

Having evaluated the potential of the setup for both transparency and electroluminescence analysis using solar cells and a wafer fragment, the investigations can now focus on strip sensors. Experiments were conducted on phase-0 CMS sensors as well as on sensors integrated into 2S modules for the CMS phase-2 upgrade.

The chapter begins with a brief description of the phase-0 sensors. This is followed by the presentation of transparency analysis results for both phase-0 and phase-2 sensors. Finally, the EL analysis and its corresponding results for the same types of sensors are detailed.

All the captured images, their processing, and additional pictures of the setup are provided in the following Google Drive folder: IR_images.

4.1 Description of the phase-0 sensors

The phase-0 sensors are the strip detectors currently used in CMS. The phase-0 modules present at IIHE are remnants from the production carried out 15 years ago. Several geometries of these modules exist, but the phase-0 sensor of the investigated module in this chapter has dimensions of 94.6 mm $\times$ 96.4 mm, with an interstrip pitch of 183 μm. Two sensors are placed side by side on the same module, with each strip of one sensor wirebonded to the corresponding strip of the other sensor. Figure 4.1 shows a phase-0 module, and Figure 4.2 presents a microscope view of the encapsulated wirebonds connecting the two sensors.

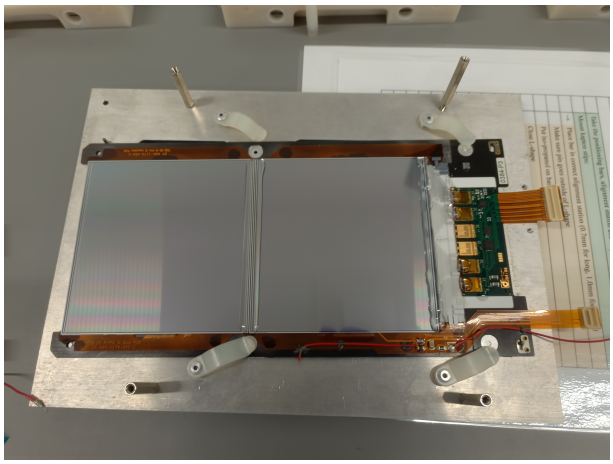

Figure 4.1: Old phase-0 silicon strip sensor module.

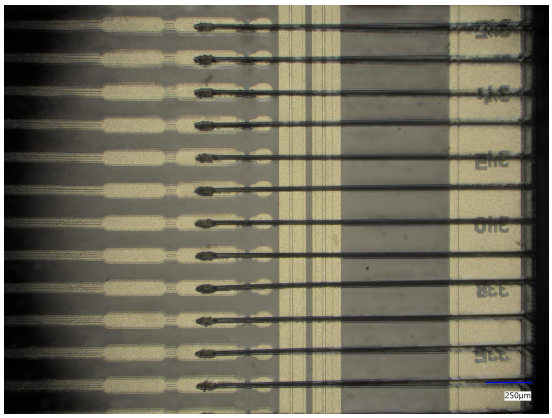

(a) Wirebonding at the left sensors.

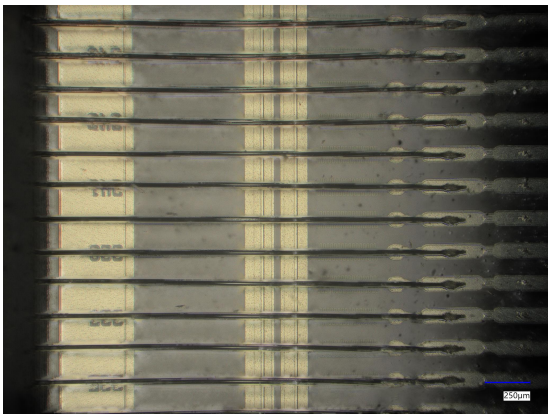

(b) Wirebonding at the right sensor.

Figure 4.2: Wirebonding between the two sensors of a phase-0 module. Each pair of strips corresponds to a number printed on the edge ring.

These sensors operate on the same principle as the new generation (phase-2 sensors), but differ in the doping of the substrate. Figure 4.3 presents a 3D schematic of the corner of a p-in-n strip sensor, representative of phase-0 devices. Compared to Figure 1.10, the design is very similar, except that the p and n dopings are inverted and no "stop" implants are required between the strips.

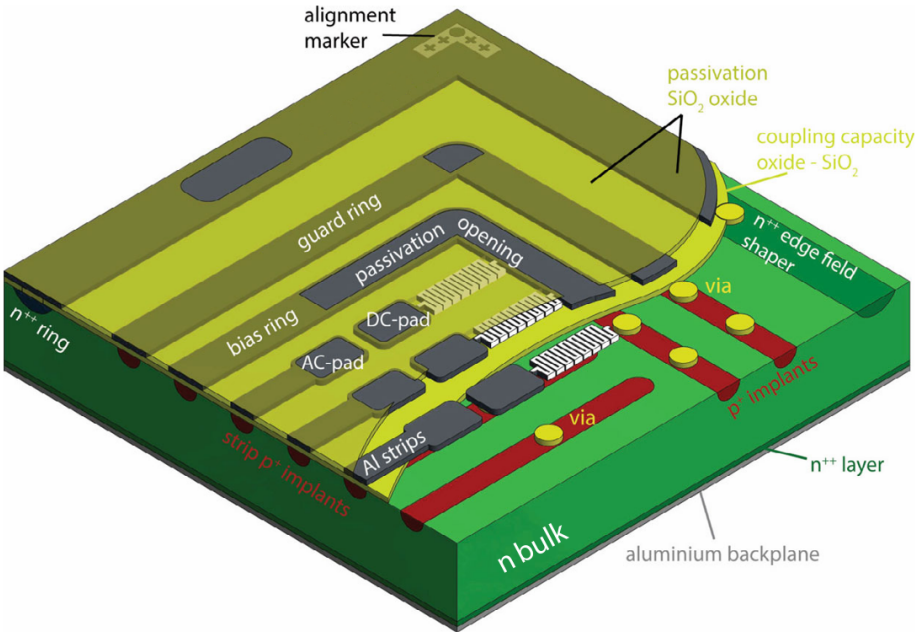

Figure 4.3: 3D schematic of the corner of a p-in-n strip sensor, adapted from [6].

As in the phase-2 sensors, biasing is applied through the bias ring and the aluminium backplane. However, in this case, a positive high voltage is applied to the aluminium backplane, while the bias ring remains connected to ground. On phase-0 modules, the bias ring of one sensor is wire-bonded at one corner (with two bonds for redundancy), while the second sensor's bias ring is wire-bonded to that of the first sensor. In phase-2 sensors, it is connected at all four corners for each of the two sensors. This wire-bonding is illustrated in Figure 4.4.

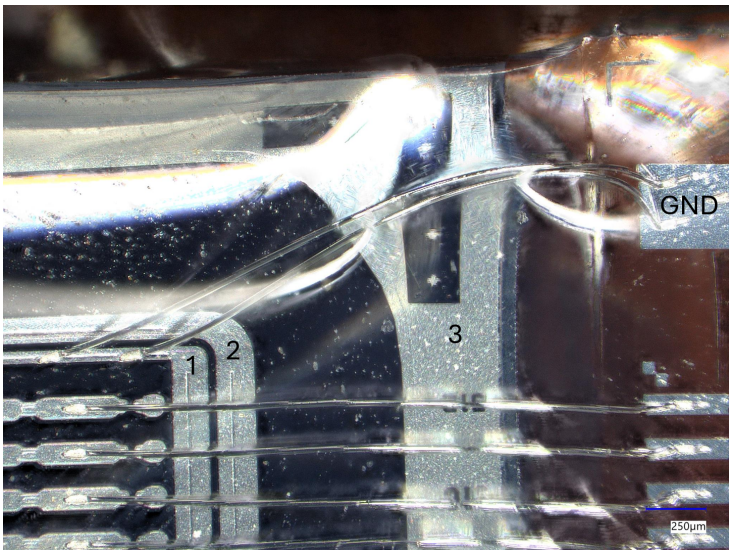

Figure 4.4: Wirebonding of the bias ring to the ground of a phase-0 sensor: (1) bias ring, (2) guard ring, and (3) edge ring.

The phase-0 sensors used in this work have never been installed in CMS and are intended solely for research purposes.

4.2 Transparency analysis for charged particle detectors

As discussed in Section 3.3.1, the analysis in transmission is not possible on assembled 2S modules and was thus not further investigated. For this reason, the rest of this work was focused on reflection experiments taken at various scales and views of the sensors.

Most of the images presented in this chapter were obtained using a 1200 nm illumination, as this LED generally provides a good image quality. Images acquired at other wavelengths are not systematically shown in order to avoid redundancy between figures.

4.2.1 Phase-0 sensors

An image taken under 1200nm illumination is shown in Figure 4.5, where no abnormalities were observed. However, such a large-scale view may not be well suited for revealing defects. Closer views were acquired in parallel with the EL experiments, but no broader investigation of transparency was performed independently, since the phase-0 sensor was introduced into the study specifically for EL inspection. This aspect is explained in more detail later in this chapter. Nevertheless, the IR images acquired during the EL experiments did not reveal any significant features that would demonstrate the usefulness of exploiting silicon transparency at the LEDs wavelengths for defect detection.

4.2.2 Phase-2 sensors

The results of the transparency analysis on phase-2 sensors are presented in this section. The experiments were performed on the `2S_18_6_BEL-10008` module, an assembled module at IIHE that exhibits unusual IV curves, with an abnormally high current draw at the sensor edges. For this reason, this module was selected for further investigation to identify possible defects

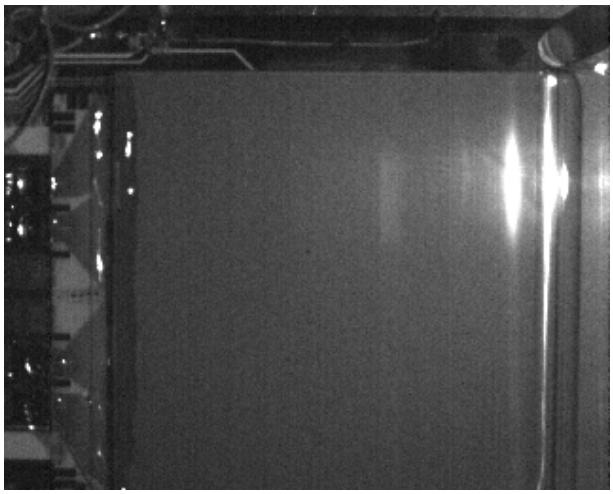

Figure 4.5: View of an entire phase-0 sensor, illuminated at 1200 nm.

in its sensor. A picture and an IR image of this module are shown in Figure 4.6. The sensor is protected by an on-module plexiglass plate to prevent accidental damage.

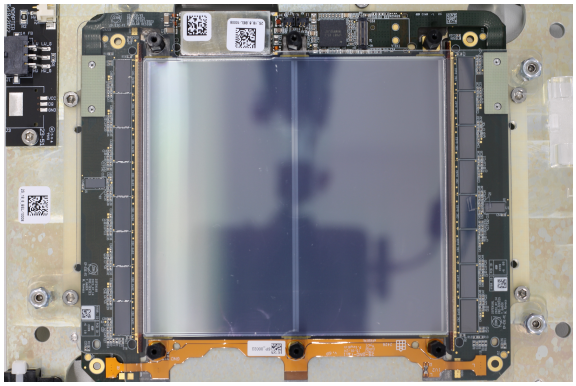

(a) The 2S_18_6_BEL-10008 module.

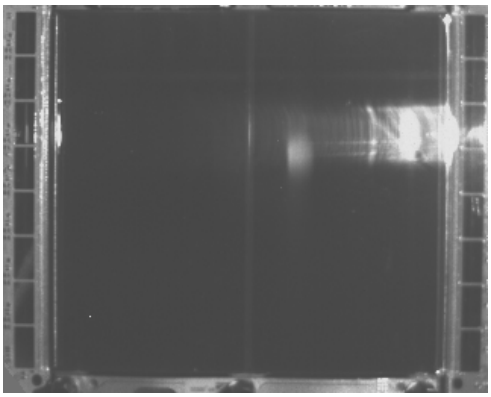

(b) IR image of the 2S_18_6_BEL-10008 module. Illuminated at 1200 nm.

Figure 4.6: Picture and IR image of an entire phase-2 sensor.

As the image in Figure 4.6b is not sufficient to detect defects and presents a large reflection artefact, a more detailed analysis was performed on each corner of the sensor, as shown in Figure 4.7.

The sensor appears dark in the images, as the illumination coming from the right is reflected to the left, outside the camera's field of view, by the aluminium surface. No abnormal structures (e.g. scratches) were observed scattering light towards the camera, except for the central aluminium line separating the two stripped sides of the sensor. The strip pattern is not visible, as is also the case to the naked eye.

Structures inside the CBCs (see Figure 1.6) located on the sensor edges are visible, providing additional evidence of silicon transparency. More detailed images are provided in Appendix J.

To obtain a closer view, a 5 mm extension tube was added to the camera. Due to the material constraints of the setup, acquiring and processing each view of the sensor was time-consuming and did not always yield high-quality images. For this reason, a full close-range scan of the sensor was not performed. However, the real-time feedback from the camera

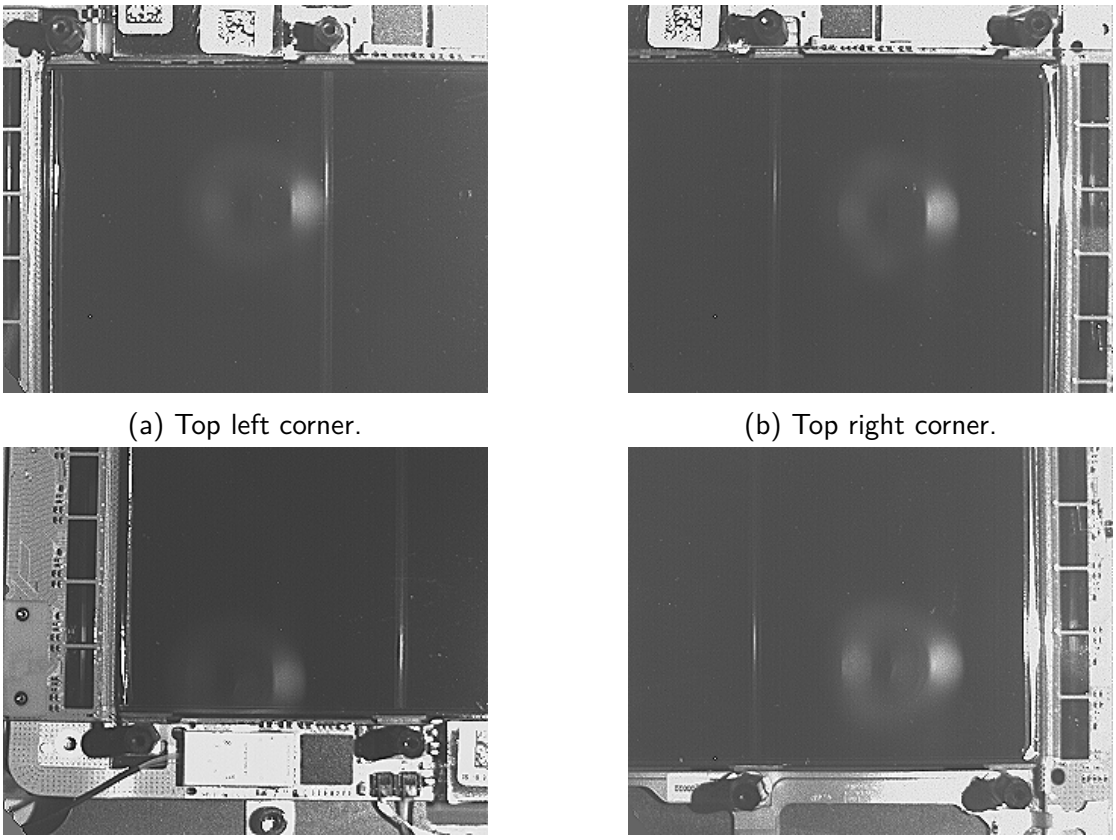

(a) Top left corner.

(b) Top right corner.

(c) Bottom left corner.

(d) Bottom right corner.

Figure 4.7: Transparency analysis at each corner of a phase-2 sensor. Illuminated at 1200 nm and processed with a sharpening filter.

software allowed grayscale mapping and contrast to be adjusted on the fly, enabling a detailed visual inspection. No significant defects were observed during this analysis. Selected images are shown in Figure 4.8.

With a closer view, good illumination, and appropriate image processing (sharpening filter), the strip pattern of the sensor becomes faintly visible (more clearly in Figures 4.8a and 4.8b). As a reminder, the strip pitch is 90 μm.

In Figure 4.8b, a slight irregularity in the encapsulation can be seen, but it does not pose any issue for the module. Two bright spots on the sensor are visible and are assumed to be dust. In addition, some brighter halos appear in certain regions of the images (e.g., in the bottom-right corner of Figure 4.8a), which are also assumed to be dust on the plexiglas plate protecting the sensor, and therefore out of focus.

Furthermore, in the three images of Figure 4.8, the bottom-left corner and one nearby pixel show corrupted pixels. This issue was later resolved by recalibrating the camera and did not occur again in subsequent images.

For a closer view of the sensors, 10 mm extension tubes can be used, but they present some drawbacks. The sensor must be positioned very close to the camera, making it difficult to illuminate the sample uniformly (see Section 3.3.2.1) and requiring the removal of the plexiglas protective plate. To avoid the risk of damaging the sensor, manipulations were limited to cases where EL imaging was performed simultaneously. These views, presented later in this chapter, did not reveal any irregularities in the strip sensors.

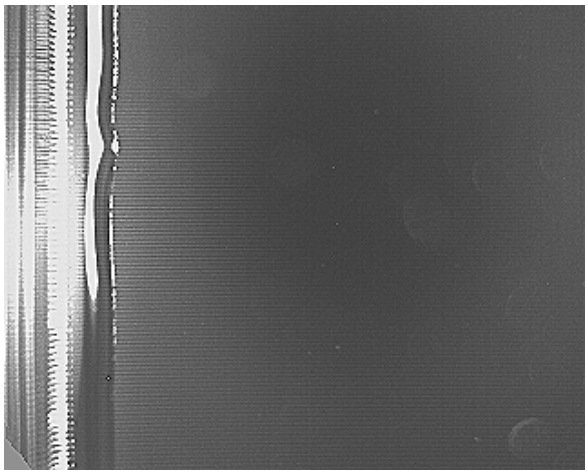

(a) Left edge.

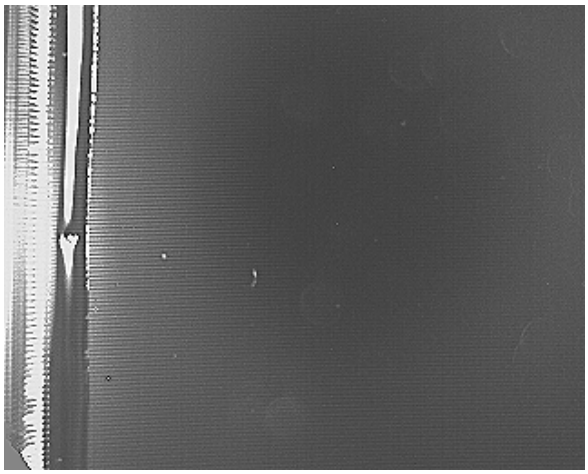

(b) Left edge.

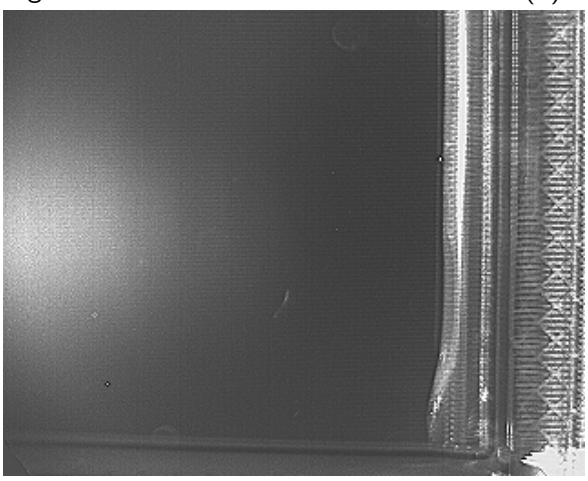

(c) Bottom right corner.

Figure 4.8: Transparency analysis with a closer view of the phase-2 sensor using a 5 mm extension tube. Illuminated at 1200 nm and processed with a sharpening filter.

4.2.3 Discussion of the transparency analysis for defect detection

As mentioned above, illumination of the strip sensors with infrared light did not reveal significant defects. In addition, material limitations represented an obstacle to effectively capturing and inspecting the sensors. Therefore, the transparency of silicon at these wavelengths has not been demonstrated to be a useful tool for defect detection in the inspected sensors. However, it has also not been demonstrated to be ineffective, since the presence and nature of possible defects remain uncertain parameters.

The previous study on silicon solar cells has shown that infrared light can be useful for revealing cracks in silicon. Consequently, this approach may still be of interest for inspecting cracks in the sensors of newly assembled 2S modules. To further investigate this possibility, future work could focus on the inspection of an intentionally damaged baby sensor of a wafer fragment.

4.3 Electroluminescence analysis for charged partile detectors

Electroluminescence experiments performed on solar cells yielded encouraging results; however, reproducing these on strip sensors proved more challenging. Initially, a series of EL experiments were conducted on the `2S_18_6_BEL-10008` module, but no signal was detected by the camera. Consequently, phase-0 sensors were used to investigate EL on this type of sensor, as they allow fewer restrictions on the current flowing through the sensors, thereby increasing the EL signal. Subsequently, the same experiments were carried out on a decommissioned 2S module, which had no particular constraints other than preserving the module's aesthetic appearance. This section presents all these results along with their discussion.

4.3.1 Phase-0 sensors

As mentioned previously, tests in both forward and reverse bias on the `2S_18_6_BEL-10008` module were initially limited to currents of 8 μA by the current source. However, the nominal current of non-irradiated 2S modules is 50 μA, and higher currents were required to perform EL. For this reason, older phase-0 modules were used to further investigate the EL technique on this type of sensor.

For both phase-0 and phase-2 strip sensors, the high-voltage supply normally passes through an RC filter and resistors located on the service hybrid and the HV tails (connected to the backplane of the sensor). See Figures 1.6 and 1.8. To prevent potential issues during the following experiments, this circuitry was bypassed and the supply was connected directly to the sensors.

4.3.1.1 EL experiments with a close view using a 10 mm extension tube

The first inspection was carried out with a 10 mm extension tube, focusing on the edge of the sensor. The current source was limited to 31,1 mA. A sequence of 100 images was acquired for a forward-biased sensor, first at 5 mA and then at 31,1 mA. After image processing, no signal was visible in the summed image for the 5 mA case. The view and the result for the 31,1 mA case are shown in Figure 4.9.

The experimental view in Figure 4.9a shows one of the two edges of the sensor that is not wirebonded. The bias and guard rings can be guessed at the bottom of the image, and the strips are clearly visible. Some dust also scattered light toward the camera. The EL image in Figure 4.9 constitutes the first EL signal obtained with strip sensors. As can be observed, the signal seems to originate from the edge of the sensor. A dark lined pattern appears, revealing the strips as well as the bias and guard rings.

Then, another current source was used in order to reach higher currents. A new experiment was performed at the junction between the two sensors of the phase-0 module using a 10 mm extension tube.

The experimental view is shown in Figure 4.10a. The image is quite noisy due to the encapsulation protecting the wire bonds, but some structures are still visible. In fact, it is a closer view than that presented in Figure 4.11a.

To analyse how the intensity of the EL signal evolves as a function of the applied current, 100-images captures were performed at 5, 30, 100, and 200 mA. The results of the processed captures are presented in Figure 4.10.

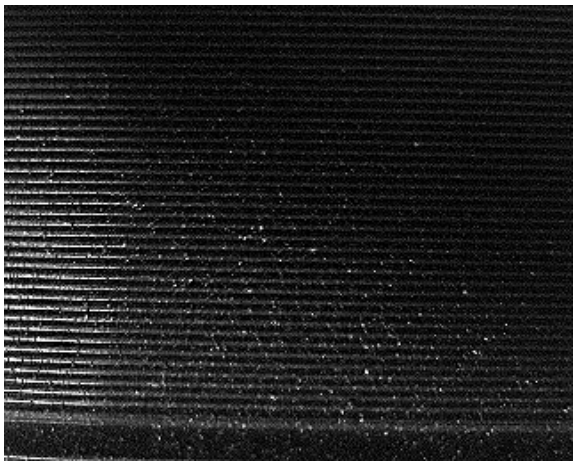

(a) Experimental view, illuminated at 1050 nm and processed with a sharpening filter.

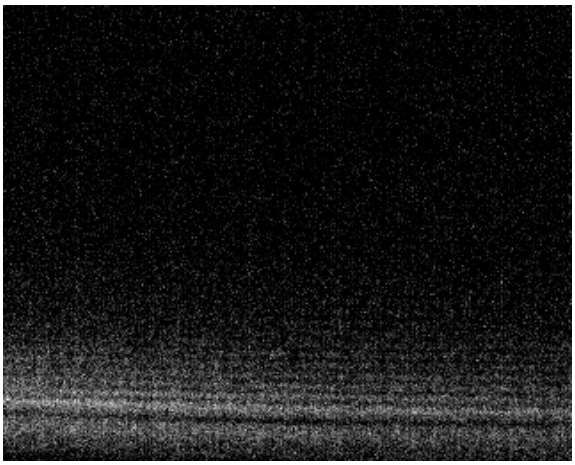

(b) Summed image at 31,1 mA.

Figure 4.9: EL experiment on a forward-biased phase-0 sensor supplied at 31,1 mA, with a close view obtained using a 10 mm extension tube.

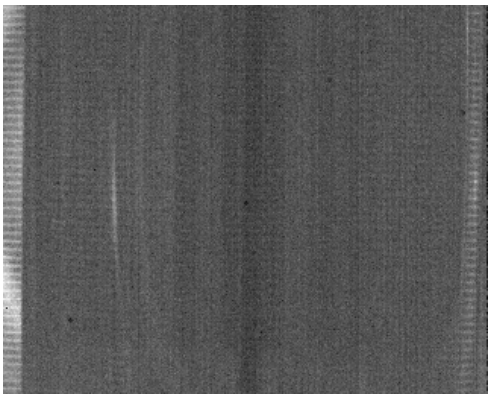

(a) Experimental view, illuminated at 1200 nm.

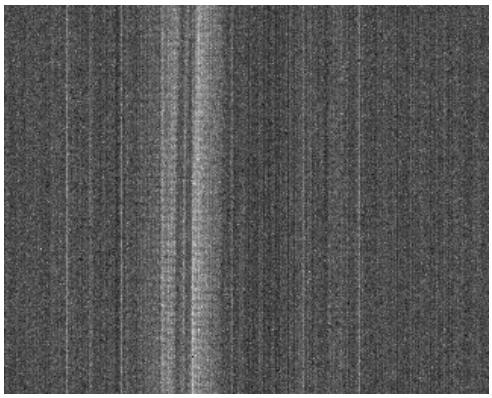

(b) Summed image at 30 mA.

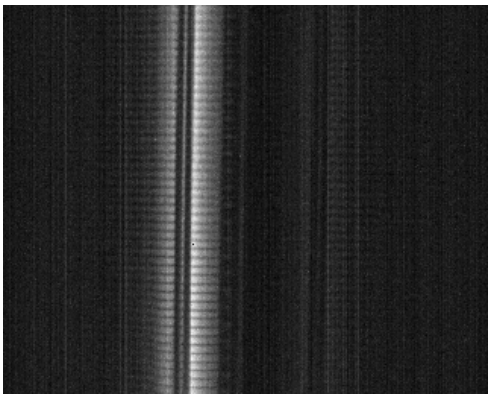

(c) Summed image at 100 mA.

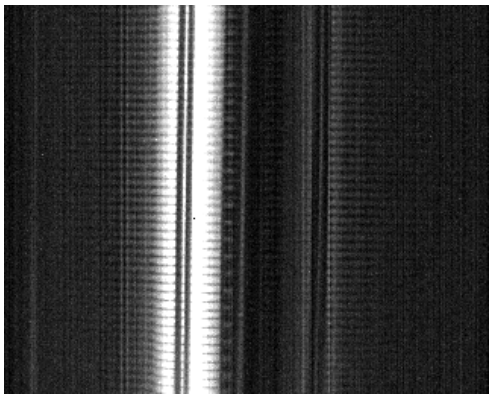

(d) Summed image at 200 mA.

Figure 4.10: EL experiment on a forward-biased phase-0 sensor supplied with increasing currents, with a close view obtained using a 10 mm extension tube.

The 5 mA capture resulted in a noisy image where no EL signal could be identified, and is therefore not reported here. The capture at 30 mA produced a noisy summed image, but some

signal is visible. At 100 mA, the light is significantly more intense, and the strips, wirebonds, bias ring, and guard ring are identifiable with much less noise than before. At 200 mA, the EL intensity is even stronger, with the bias and guard ring of the left sensor clearly visible in high contrast with the EL light. Moreover, Figure 4.10d is intentionally slightly saturated to highlight the fact that a weaker, yet present, EL signal can be observed in the sensor on the right side.

Given the high contrast between the bias and guard rings and the EL signal, a logical conclusion would be that the EL originates from beneath these rings. This is consistent with the observations from Figure 4.9b.

4.3.1.2 EL experiment with a close view using a 5 mm extension tube

To investigate if there may exist some differences in the EL signal as a function of the field of view of the sensor, the same experiment has been performed with larger view by using a 5 mm extention tube. The resluts of this experiment are given in Figure 4.11.

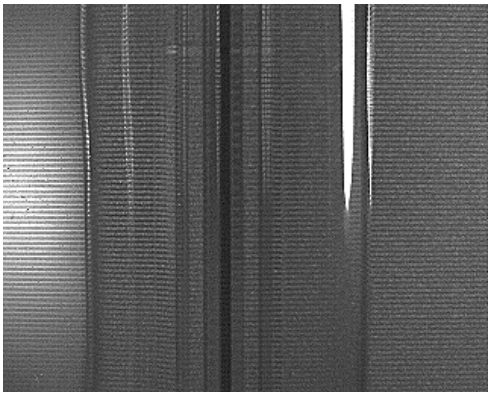

(a) Experimental view, illuminated at 1200 nm and processed with a sharpening filter.

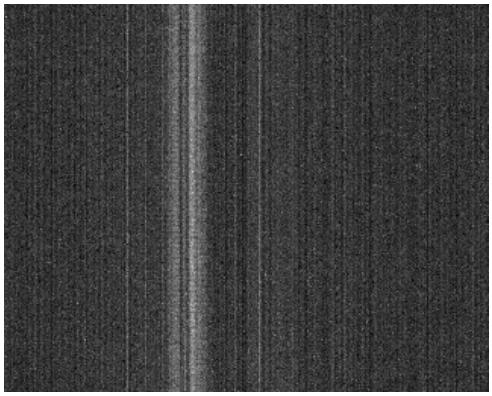

(b) Summed image at 30 mA.

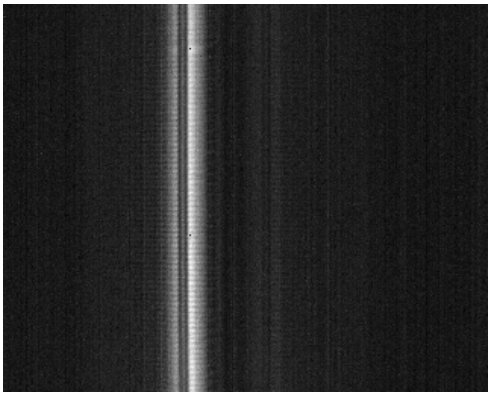

(c) Summed image at 100 mA.

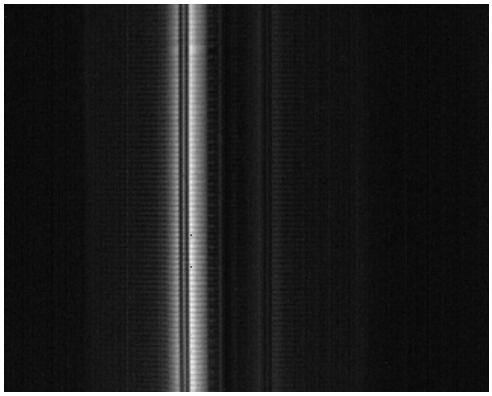

(d) Summed image at 200 mA.

Figure 4.11: EL experiment on a forward-biased phase-0 sensor supplied with increasing currents, with a close view obtained using a 5 mm extension tube.

Figure 4.11a provides a high-quality image of the strips. At the top of the image, an irregularity can be observed at the wirebonding between the two sensors, caused by a missing micro-wire. The junction was encapsulated specifically for these experiments and the micro-

wire was already missing at that time. This does not constitute evidence for defect detection using the transparency of silicon, since it can also be observed in the visible range.

Compared to the experiment with a 10 mm extension tube, the results are quite similar. The 5 mA capture still produced no usable signal and is therefore not reported here. The bias and guard rings remain clearly visible, especially in Figures 4.11c and 4.11d. The experiment at 200 mA does not show a significant difference compared to the one at 100 mA, except for reduced noise due to the stronger signal.

4.3.1.3 EL experiment with an entire view of the sensor

As the EL appears to be uniform along the guard and bias rings, it would be interesting to capture EL at the scale of the entire sensor. This constitutes the last EL experiment performed on the phase-0 sensor. The same modus operandi was applied, with no extension tube on the camera, and the results are shown in Figure 4.12.

Again, at 5 mA, nothing was detected. However, the summed images from the captures at 30 mA, 100 mA, and 200 mA revealed a very interesting result: a gradient in EL intensity can be observed along the bias and guard ring, with a maximum at the bottom-left corner. This corner corresponds exactly to the location where the bias ring is connected to the ground, as shown in Figure 4.4, highlighting the presence of higher currents at this point. This EL gradient extends into the sensor on the right, although it is less pronounced.

4.3.2 Phase-2 sensors

EL experiments on the `2S_18_6_BEL-10008` module were not performed at currents higher than 8 μA to avoid any damage, as this module is still usable despite its irregularities. As demonstrated in the experiments on the phase-0 sensors, a difference of three orders of magnitude in the current is necessary to obtain an exploitable signal, even when increasing the number of images per capture by a factor of 100. For this reason, another 2S module was required to verify whether the observations made on the phase-0 sensors also apply to those of phase-2.

The module used was a decommissioned 2S module, which now serves solely as a display model for visitors. The only requirement was therefore to ensure that its aesthetics were not degraded. As with the phase-0 sensor, the RC filter and resistors were bypassed, and the sensors were directly supplied by the current source.

Since the connections between the bias ring and ground occur at each corner of the phase-2 sensors, a more homogeneous EL intensity was expected along the sensor edges. One corner was therefore investigated using a close view obtained with the 5 mm extension tube, and another with the 10 mm extension tube. Captures were performed with a current supply of 25, 50, 100, and 250 mA for each view, plus an additional capture at 1 A for the view taken with the 10 mm extension tube. The results of these tests are shown in Figures 4.13 and 4.14.

A first observation is that, as expected, the EL occurs along the bias and guard rings.

At 25 mA, the summed image is too noisy to clearly distinguish the EL from the background. At 50 mA, some brighter spots appear within the noise, but the shape of the sensor is still not discernible. Even at 100 mA, the summed images remain very noisy, which was not the case for the phase-0 sensor. At 250 mA, some noise is still present. This indicates that higher currents are required to achieve the same image quality, which can be explained by the more homogeneous distribution of current along the sensors.

In the investigated phase-0 sensor, most of the EL signal originated from one sensor, while the second sensor was not as well supplied with current. This imbalance resulted in stronger

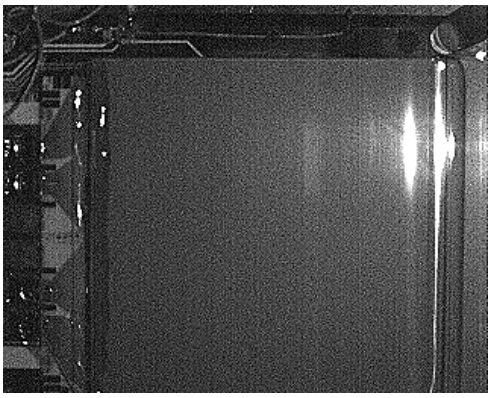

(a) Experimental view, illuminated at 1200 nm and processed with a sharpening filter.

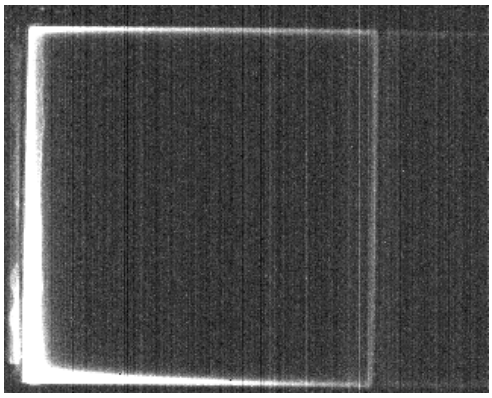

(b) Summed image at 30 mA.

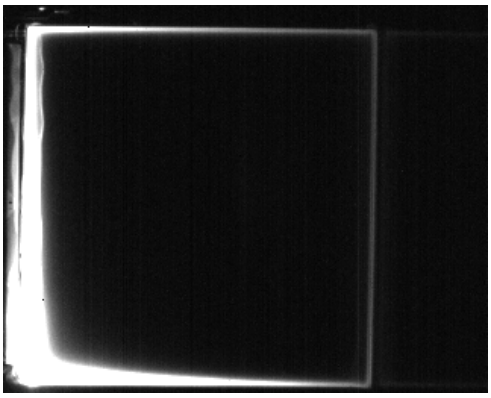

(c) Summed image at 100 mA.

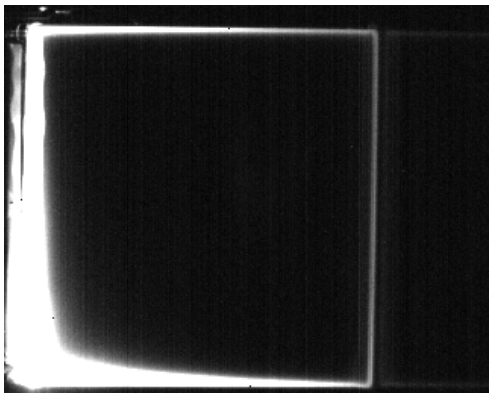

(d) Summed image at 200 mA.

Figure 4.12: EL experiment on a forward-biased phase-0 sensor supplied with increasing currents, view of the entire sensor.

EL emission from the investigated sensor. In the phase-2 sensors, both sensors are equally connected to ground, allowing for a better distribution of the current. Consequently, the total current supplied to the phase-2 sensors needs to be increased compared to the phase-0 sensor, which was advantageously powered.

The experiment at 1 A was performed by capturing 1000 frames while switching the supply on and off to avoid excessive heating due to the Joule effect. This resulted in a high-contrast image with low noise.

In both Figures 4.13 and 4.14, the EL appears to stop at the intersection between the AC-pads and the bias and guard rings. This unexpected phenomenon may be explained by the thickness of the AC pads (shown in Figure 4.15), which may not allow enough photons to pass through. However, this hypothesis has not been proven, and no alternative explanation has been found.

4.3.3 Discussion of the EL analysis for defect detection

Given the observations, three questions may arise:

1. Can the 2S modules sustain such high currents?
2. Why is the EL confined to the bias and guard rings?

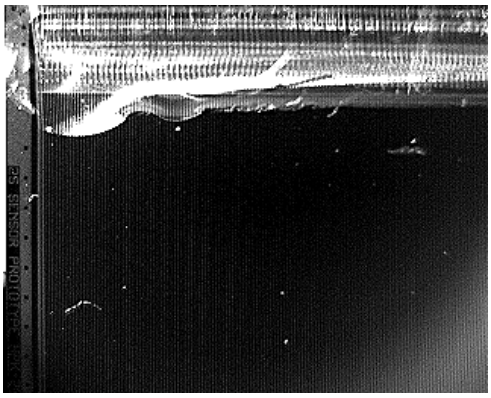

(a) Experimental view, illuminated at 1050 nm and processed with a sharpening filter.

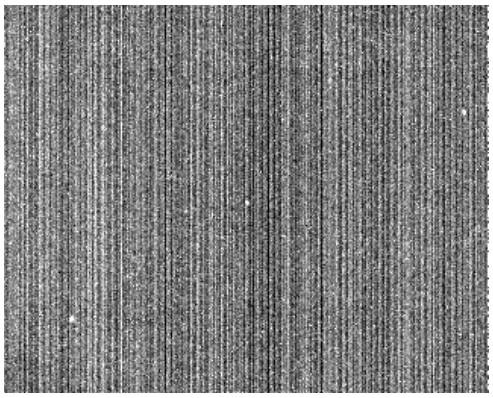

(b) Summed image at 25 mA.

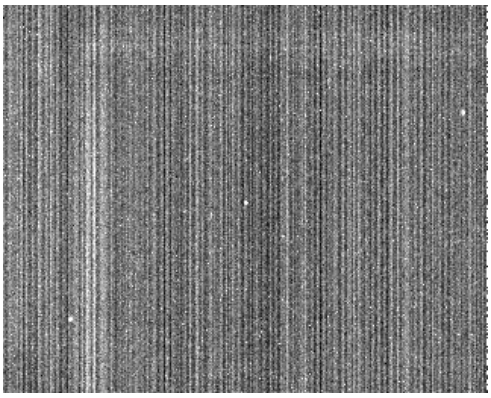

(c) Summed image at 50 mA.

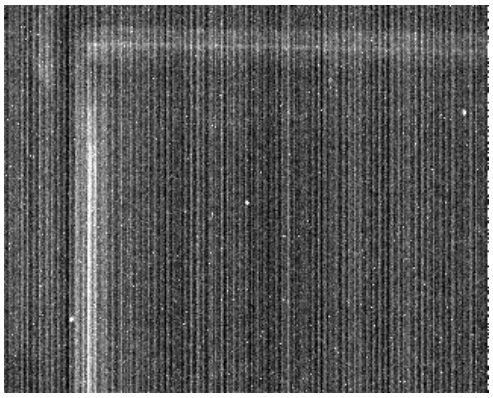

(d) Summed image at 100 mA.

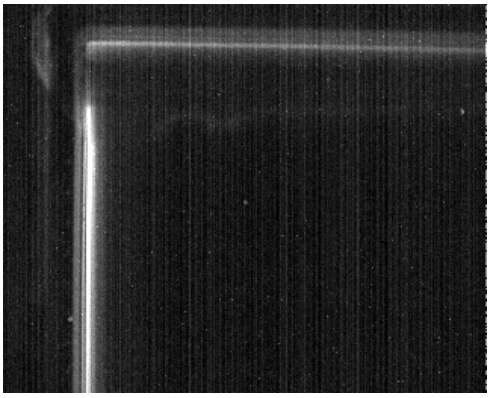

(e) Summed image at 250 mA.

Figure 4.13: EL experiment on a forward-biased phase-2 sensor supplied with increasing currents, with a close view obtained using a 5 mm extension tube.

3. Is this technique suitable as a quality control tool in the assembly line?

The purpose of this discussion is to attempt to address these questions.

4.3.3.1 Current sustainability of 2S modules

Silicon is a semiconductor with an indirect bandgap structure, which requires phonons for interband transitions to satisfy conservation of energy and momentum [27, p. 380-386]. This

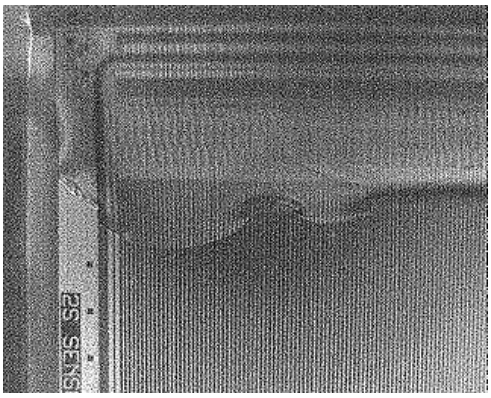

(a) Experimental view, illuminated at 1200 nm and processed with a sharpening filter.

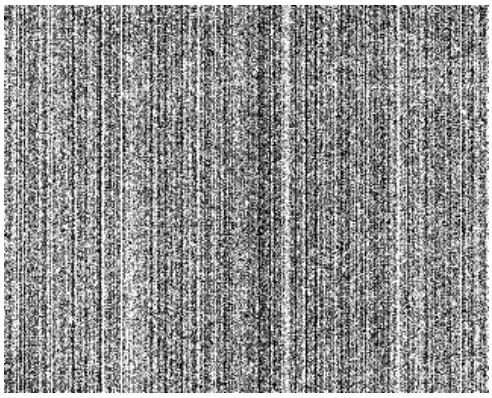

(b) Summed image at 25 mA.

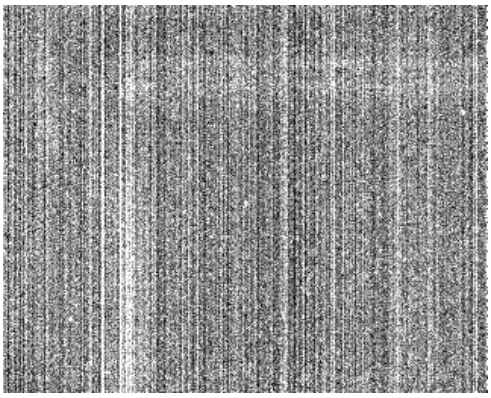

(c) Summed image at 50 mA.

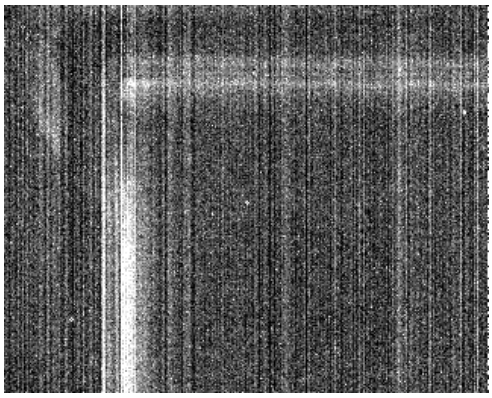

(d) Summed image at 100 mA.

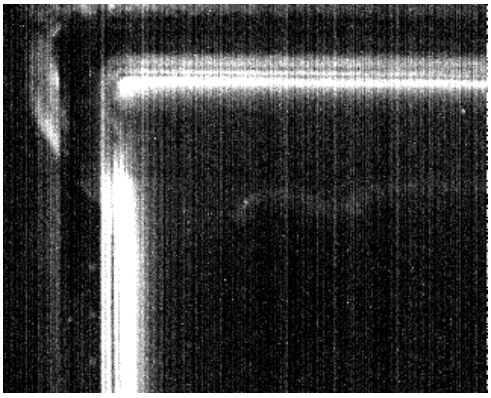

(e) Summed image at 250 mA.

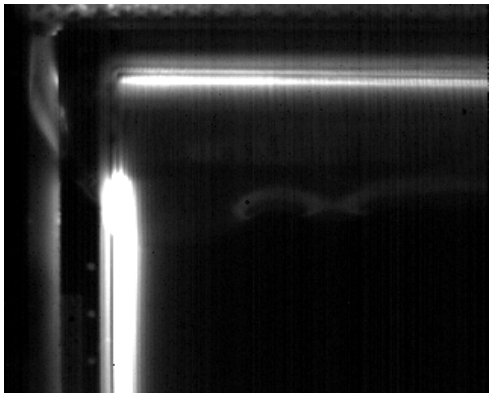

(f) Summed image at 1 A.

Figure 4.14: EL experiment on a forward-biased phase-2 sensor supplied with increasing currents, with a close view obtained using a 10 mm extension tube.

explains the very low quantum efficiency for EL in silicon forward-biased p-n junctions [28]. A high density of injected carriers is therefore needed to generate enough radiative transitions to be captured by the camera.

Since a current of about 100–250 mA is required in the sensors to obtain a sufficient EL signal, one may question whether the 2S modules can effectively sustain such currents.

For these tests, the electronics of the service hybrids and the HV tails were bypassed. These normally include an RC filter and a set of resistors. According to the SEH Pana V3_1

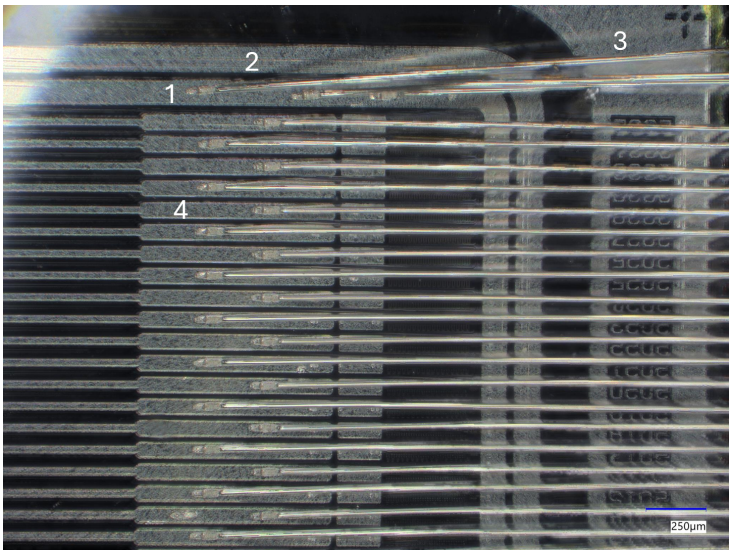

Figure 4.15: Microscope view at the corner of a phase-2 sensor: (1) bias ring, (2) guard ring, (3) edge ring and (4) AC-pads.

electronic schematic, the resistors are 8.8 kΩ and 1 kΩ, implemented as 0402 chip resistors with a maximum power dissipation P_{max} of 1/16 W. A simple calculation ($I_{\text{max}} = \sqrt{P_{\text{max}}/R}$) gives a maximum current I_{max} of 2.67 mA for $R = 8.8$ kΩ and 7.9 mA for $R = 1$ kΩ.

In conclusion, the service hybrids and HV tails cannot support the high currents required for EL.

4.3.3.2 EL at the bias and guard rings

As demonstrated during the experiments, the EL is mainly observed along the bias and guard rings. This indicates that the depletion region of the p-n junction is confined near these structures. For a phase-2 sensor, it is located between the n^+ implants of the bias and guard rings, and the p^+ implant of the edge ring together with the p^{++} doping of the backplane, as illustrated in Figure 1.11. For the phase-0 sensors, the same behavior is observed, but with the dopings inverted.

Since the radiative transitions occur underneath the bias and guard rings, the isotropically emitted photons must be scattered in order to reach the camera objective. This also reduces the yield between the injected current and the detected EL signal. One possible way to improve this yield would be to perform the experiment with the sensor placed at an oblique angle, but the experimental setup was not designed for this purpose.

4.3.3.3 Suitability of EL imaging for quality control

The confinement of EL at the edges of the sensors does not provide an optimal configuration for defect detection. In contrast to solar cells, where a homogeneous EL signal is essential for inspecting the entire device, the signal in these sensors is localized. One possible way to detect a defect would be through efficient light scattering caused by the defect, but no experimental evidence of this was obtained. Another issue that EL could potentially reveal is a poor connection of the bias ring to ground; however, this is unlikely since three wirebonds connect the bias ring to the ground for redundancy (see Figure 4.15).

In addition, the requirement for high currents, which makes it necessary to bypass some of

the electronic components of the sensors, poses a practical limitation for testing an assembled module efficiently.

Therefore, EL imaging does not appear to be a suitable method for quality control of 2S modules at the IIHE assembly line, in contrast to its successful application in solar cells.

4.4 Future work

During the work carried out in this thesis, several directions for future investigation were identified.

In the EL experiments, it was noticed that a peak in the EL signal appeared at the startup of the current source. The measurement of this transient, given in Appendix K, revealed that high currents were briefly reached, producing sufficient EL before the regulator of the source limited the current to its requested value. In fact, the HV circuit resistors can withstand much larger currents for very short times, depending on their duty cycle characteristics. The duty cycle is defined as the ratio of the pulse width to the period of a periodic pulsed signal [29, p. 16]. Knowing that the camera has an input for synchronization, a complete characterization of the HV circuit of the module could make it possible to trigger the camera on HV pulses, thereby capturing high-quality electroluminescence images while minimizing damage on the HV circuit.

Another promising approach for defect detection is photoluminescence. In this technique, carriers in the semiconductor are excited by photons and subsequently recombine radiatively, emitting secondary photons that can be detected. Photoluminescence imaging is already employed for the inspection of photovoltaic cells and offers the advantage of requiring no electrical contact with the samples [30, 31]. Adapting this method to the present work would require a redesign of the optical setup.

Finally, a more detailed study of transparency on wafer fragments would help to better assess the potential of transparency imaging for defect detection. As a first step, this could be pursued by deliberately inducing controlled damage.

Chapter 5

Conclusion

The work presented in this thesis aimed to explore two techniques by building an experimental setup designed to detect defects in silicon strip detectors using a camera sensitive in the SWIR range. The first technique consisted in illuminating the sensors with infrared LEDs, while the second relied on forward biasing the sensors to observe their electroluminescence. The success of these approaches could provide a useful inspection tool for the assembly line of 2S modules at IIHE, within the scope of the phase-2 upgrade project of the CMS silicon tracker.

First, the experimental setup was designed and implemented inside a light-isolated cabinet. This required selecting appropriate optical components, designing and building a pneumatic system to dry the air in the cabinet, as well as creating and 3D-printing mechanical parts. The firmware of an electronic board for control and monitoring of the setup was also programmed, although its full potential was not fully exploited.

A validation of the setup was then carried out. It confirmed that the system was capable of efficiently detecting defects in silicon solar cells, as well as in a wafer fragment taken from the same wafer as a CMS phase-0 sensor. However, it was concluded that transmission-based transparency analysis would not be applicable to assembled 2S modules, due to the superposition of two aluminium backplanes.

Subsequently, reflection-based transparency analysis was performed on both phase-0 and phase-2 sensors. Unfortunately, these experiments did not reveal significant defects. This study was limited by material constraints of the setup — such as the need to bring the sensors very close to the camera — as well as by the unknown nature of the expected defects. Nevertheless, this method could still be of interest for detecting potential cracks, but this remains to be demonstrated for this type of sensor.

Finally, phase-0 and phase-2 sensors of CMS were forward-biased, producing an EL signal along the bias and guard rings. However, currents much higher than the nominal operating current of 2S modules were required, which made it necessary to bypass the module electronics. Furthermore, the inhomogeneity of the EL observed in these sensors does not provide conditions as favourable for defect detection as in the case of solar cells. Overall, these limitations make systematic inspection of modules using this technique impractical in its current form for the assembly line.

In summary, these analyses clarified the potential and limitations of transparency imaging and EL for detecting defects in silicon strip sensors. Building on this work, synchronizing the camera with HV pulses could potentially yield high-quality EL images with minimal electrical stress on module electronics, while photoluminescence imaging could offer a complementary, contact-free approach already used in photovoltaic inspection.

Declaration of generative AI and AI-assisted technologies in the writing process

During the preparation of this work, the author used ChatGPT and Copilot in order to debug code (firmware and LaTeX), assist in implementing image processing and find references. After using this tool/service, the author reviewed and edited the content as needed and take full responsibility for the content of the publication.

Bibliography

[1] CERN. 70 years of CERN. *Nature Reviews Physics* 6(10), 577–577 (2024).

[2] G. Arnison et al. Experimental observation of isolated large transverse energy electrons with associated missing energy at s=540 GeV. *Physics Letters B* 122(1), 103–116 (1983).

[3] S. Chatrchyan et al. Observation of a new boson at a mass of 125 GeV with the CMS experiment at the LHC. *Physics Letters B* 716(1), 30–61 (2012).

[4] E. Lopienska. The CERN accelerator complex, layout in 2022. General Photo (2022).

[5] L. Evans and P. Bryant. LHC Machine. *Journal of Instrumentation* 3(08), S08001 (2008).

[6] F. Hartmann. *Evolution of Silicon Sensor Technology in Particle Physics: Basics and Applications*. 3rd edition. Vol. 293 (Springer Nature Switzerland, Cham, 2024).

[7] G. Bayatian et al. CMS Physics Technical Design Report: Addendum on High Density QCD with Heavy Ions (2007).

[8] S. Di Mitri. *Fundamentals of Particle Accelerator Physics* (Springer International Publishing, Cham, 2022).

[9] S. Chatrchyan et al. The CMS experiment at the CERN LHC. *Journal of Instrumentation* 3(08), S08004 (2008).

[10] K. Nash. The Phase-2 upgrade of the CMS outer tracker. *Nuclear Instruments and Methods in Physics Research Section A: Accelerators, Spectrometers, Detectors and Associated Equipment* 1058, 168788 (2024).

[11] *Project Schedule*. Accessed: 12 July 2025. CERN. 2025. URL: https://project-hl-lhc-industry.web.cern.ch/content/project-schedule.

[12] G. Lindström, M. Moll, and E. Fretwurst. Radiation hardness of silicon detectors - a challenge from high-energy physics. *Nuclear Instruments and Methods in Physics Research Section A: Accelerators, Spectrometers, Detectors and Associated Equipment* 426(1), 1–15 (1999).

[13] M. Moll. Radiation damage in silicon particle detectors: Microscopic defects and macroscopic properties. PhD Thesis. Hamburg U., (1999).

[14] The CMS Collaboration. *The Phase-2 Upgrade of the CMS Tracker - Technical Design Report*. Tech. rep. CERN-LHCC-2017-009. CERN, (2017).

[15] R. Besson. *Technologie des composants électroniques, Tome 2* (Édition Radio, 1967).

[16] The CMS Collaboration. *Technical Specification for the Supply of Silicon Sensors for the CMS Outer Tracker upgrade project*. Tech. rep. CERN, (2019).

[17] M. A. Green. Self-consistent optical parameters of intrinsic silicon at 300 K including temperature coefficients. *Solar energy materials and solar cells* 92(11), 1305–1310 (2008).

[18] U. Jahn et al. Review on IR and EL Imaging for PV Field Applications (2018).

[19] F. Spertino et al. A power and energy procedure in operating photovoltaic systems to quantify the losses according to the causes. *Solar Energy* 118, 313–326 (2015).

[20] M. Paggi et al. Fatigue degradation and electric recovery in Silicon solar cells embedded in photovoltaic modules. *Scientific reports* 4, 4506 (2014).

[21] B. Burkle et al. *AICF Bridge Humidity Measurements*. Presentation. (2022).

[22] U. Heintz et al. QC Document for Preproduction and Production Modules (v4) (2025).

[23] W. Burger and M. J. Burge. *Digital Image Processing: An Algorithmic Introduction Using Java* (Springer, London, 2016).

[24] M. W. Davidson and M. Abramowitz. Optical Microscopy. *Encyclopedia of Imaging Science and Technology* (2002).

[25] C. O. Ayieko et al. Controlled Texturing of Aluminum Sheet for Solar Energy Applications. *Advances in Materials Physics and Chemistry* 5(11), 458–466 (2015).

[26] B. R. Masters. *Superresolution Optical Microscopy: The Quest for Enhanced Resolution and Contrast*. Vol. 227 (Springer International Publishing, Cham, 2020).

[27] M. Dresselhaus et al. *Solid State Properties* (Springer, Berlin, Heidelberg, 2018).

[28] M. S. Bresler et al. Electroluminescence efficiency of silicon diodes. *Phys. Solid State* 46(1), 5–9 (2004).

[29] P. Horowitz and W. Hill. *The art of electronics*. Third edition, 20th printing with corrections (Cambridge University Press, Cambridge, New York, 2024).

[30] A. Redondo Plaza et al. Partial Photoluminescence Imaging for Inspection of Photovoltaic Cells: Artificial LED Excitation and Sunlight Excitation. *Energies* 16(11), 4531 (2023).

[31] T. Trupke et al. Photoluminescence Imaging for Photovoltaic Applications. *Energy Procedia*. International Conference on Materials for Advanced Technologies 2011, Symposium O 15, 135–146 (2012).

[32] E. Hecht. *Optics*. 4th ed. (Addison-Wesley, Reading, Mass, 2002).

[33] P. Hilgraf. *Pneumatic Conveying: Basics, Design and Operation of Plants* (Springer, Berlin, Heidelberg, 2024).

Appendices

A Appendix: The assembly jigs at IIHE.

The construction of the 2S modules relies on manual jig-based assembly techniques, with robotic assistance for glueing and wirebonding. The first step in the assembly line involves gluing the Kapton isolators and high-voltage (HV) tails onto the sensors. The sensor is placed on a jig that holds it in a fixed position using a vacuum system. This jig is illustrated in Figure 1a. Metallic bars ensure that the Kapton is glued in the correct positions. This step is followed by wirebonding and encapsulation.

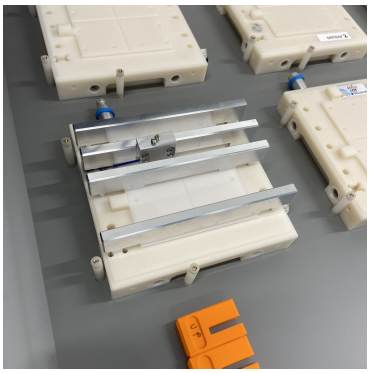

(a) Kapton jig.

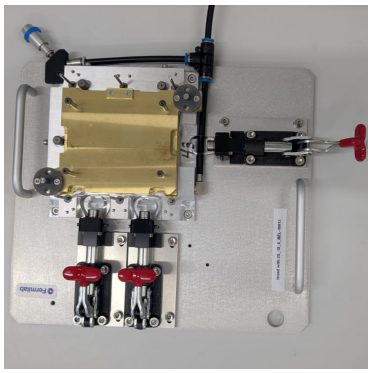

(b) Sandwich jig.

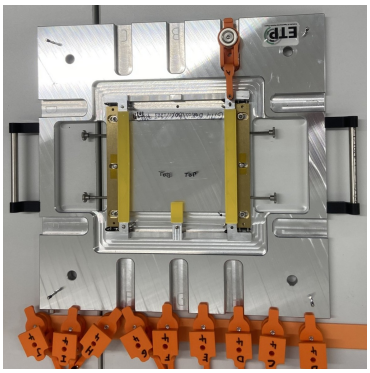

(c) Hybrid glueing jig.

(d) 2S Module.

Figure 1: (a, b, c) Jigs of the assembly line and (d) a fully assembled 2S module.

The sensors are then glued together using spacers (bridges) positioned between the kapton layers of the two sensors. This is the most critical assembly step in terms of alignment precision. The sensors are sandwiched between a weight plate and a jig (also equipped with a vacuum system) to maintain pressure during the curing of the glue. Springs on the sides of the jig, shown in Figure 1b, ensure proper alignment between the two sensors. However, if these springs

apply excessive force, they can cause defects in the sensors. After this step, the alignment is verified by measuring the angle between the strips of the two sensors. The required alignment precision between the sensors is defined as follows: a displacement perpendicular to the strips of less than $\Delta x < 50$ μm, a displacement along the strips of less than $\Delta y < 100$ μm, and a tilt angle between the strips smaller than 400 μrad [14]. For this reason, the sensors must be cut with a precision better than $\pm$ 10 μm along the critical edge.

Then, the readout electronic hybrids are glued using the hybrid glueing jig shown in Figure 1c. Custom 3D-printed parts are used to hold all components in place on the sides of the jig. The electronics are then tested. The next step is to wirebond each sensor strip to the corresponding readout chip. This process is performed using a fully automated wirebonder. The bonding wires are then encapsulated with glue, followed by a series of control tests. Finally, the modules undergo thermal cycling to verify their ability to withstand temperature variations (as different parts of the module have different coefficients of thermal expansion). This is necessary because the modules will operate around -30 °C in CMS.

B Appendix: Optics of the camera

The following ray description of the optics comes from [32] and by asuming the f $= 16$ mm lens as a thin lens. The extention tubes increase the image distance d_i and decrease the object distance d_o (both positive defined values on their respective side of the lens), both linked by the lens equation plotted on Figure 2.

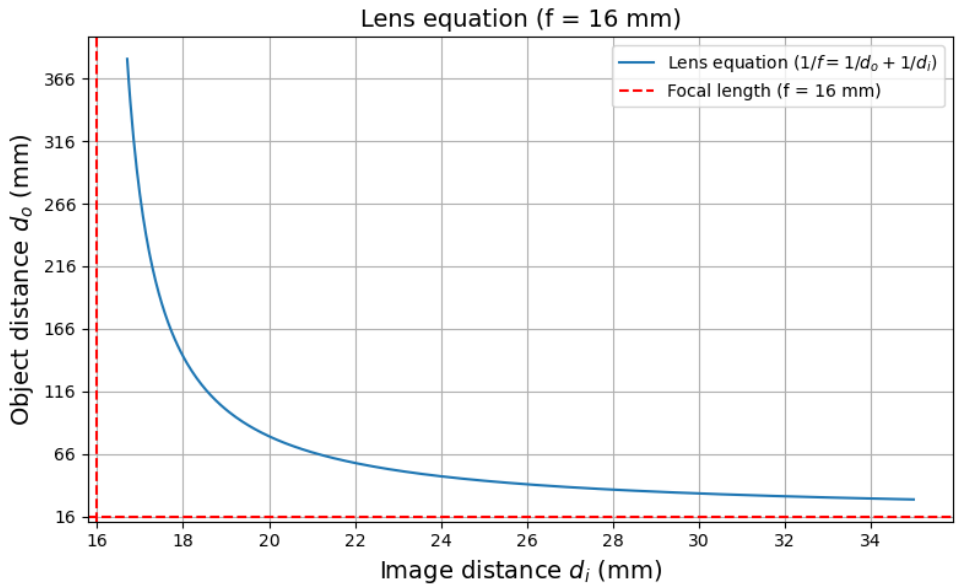

Figure 2: Plot of the lens equation with a focal length $f = 16$ mm.

In practice, the origin and the real optics inside the lens are not known but this non-accurate description gives a good idea of the principle and the focus is finetuned with the manual focus of the lens.

The transverse magnification is defined as

$$M = \frac{y_i}{y_o} = -\frac{d_i}{d_o} \tag{1}$$

where y_i and y_o stands for the transverse distance with the optical axis respectively for the image and the object plane. Since the object is inverted in the image plane, y_i has the opposite sign of y_o and gives an negative value to the magnification. The magnification as a function of the image distance is plotted on Figure 3.

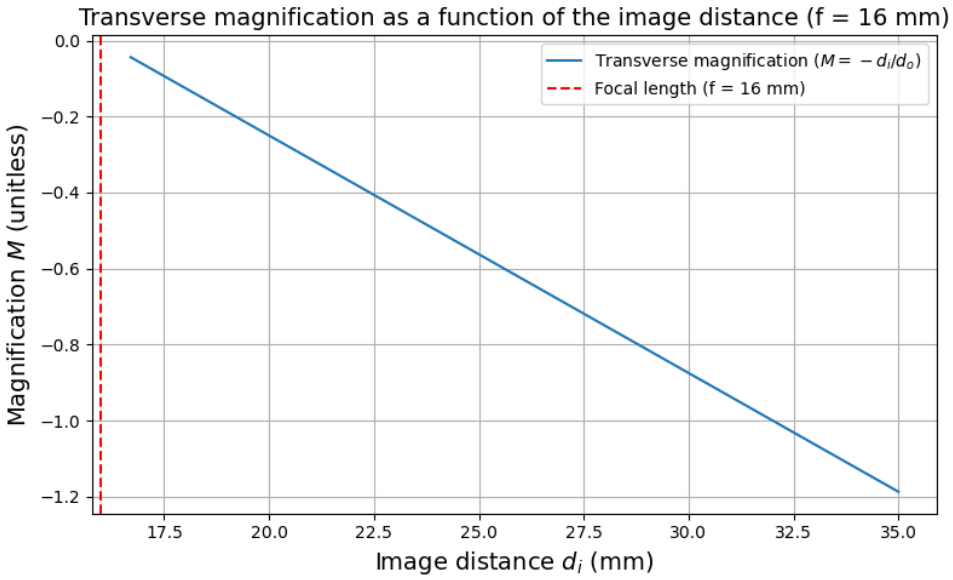

Figure 3: Plot of the transverse magnification as a function of the image distance d_i for a focal length $f = 16$ mm.

C Appendix: LED's emission spectrums

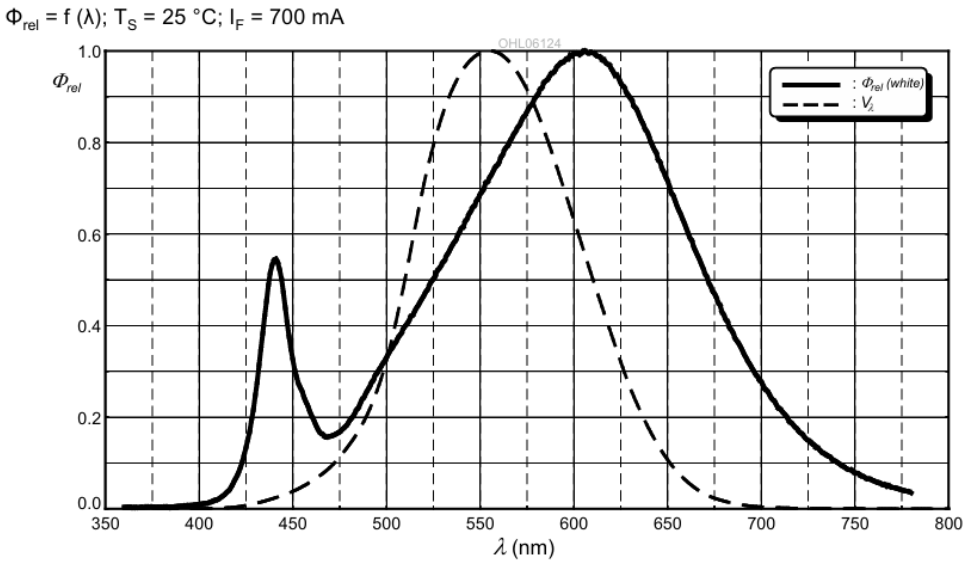

Figure 4: Relative emission spectrum of the white LED. The dashed V_λ curve is the standard eye response and Φ_{rel} is the relative luminous flux. Taken from the LCW CQAR.EC datasheet.

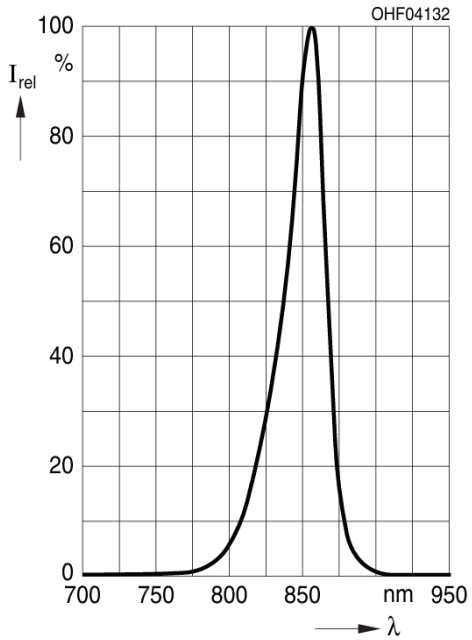

(a) Emission spectrum of the 850 nm LED. I_{rel} is the relative intensity. Taken from the SFH 4716S datasheet.

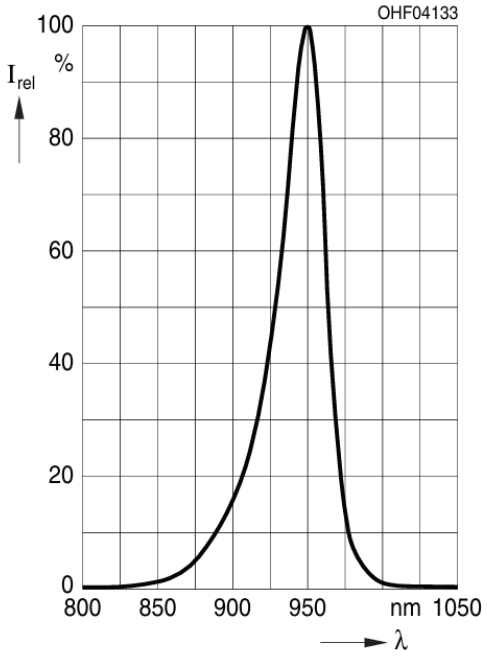

(b) Emission spectrum of the 950 nm LED. I_{rel} is the relative intensity. Taken from the SFH 4775S datasheet.

Figure 5: Spectral emission of the 850 nm and 950 nm LEDs.

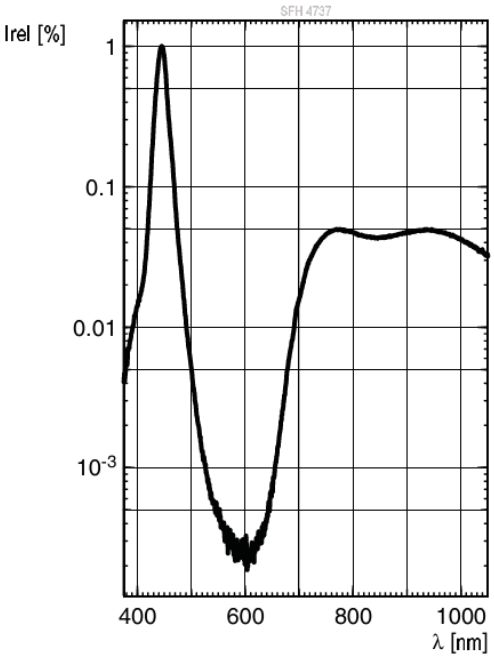

(a) Emission spectrum of the broadband LED. I_{rel} is the relative intensity. Taken from the SFH 4737 datasheet.

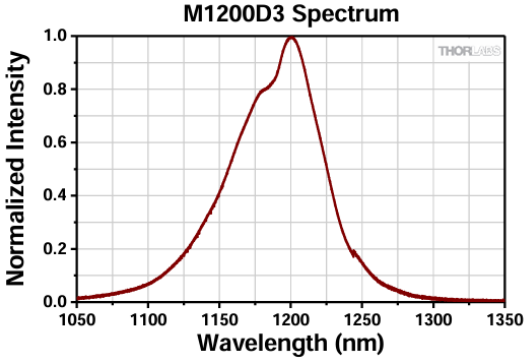

(b) Emission spectrum of the 1200 nm LED. Taken from the M1200D3 datasheet.

Figure 6: Spectral emission of the broadband and 1200 nm LEDs.

D Appendix: Narrow band filters transmission spectrums

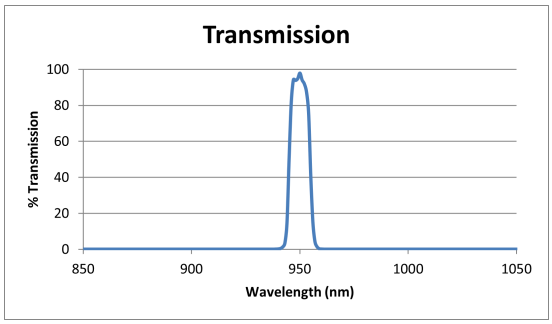

(a) 950 nm narrow band filter. Taken from the FBH950-10 data provided by THORLABS.

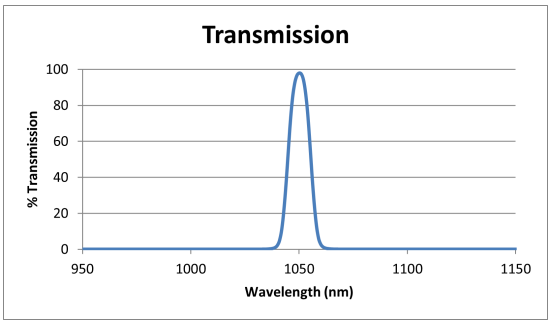

(b) 1050 nm narrow band filter. Taken from the FBH1050-10 data provided by THORLABS.

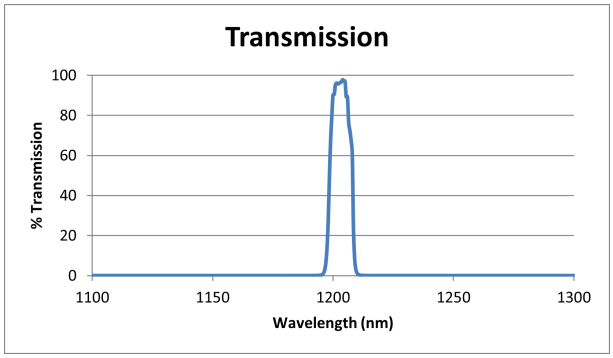

(c) 1200 nm narrow band filter. Taken from the FBH1200-10 data provided by THORLABS.

Figure 7: Transmission spectra of narrow band filters centered at 950, 1050 and 1200 nm.

E Appendix: components of the pneumatic system

Reference	Description	Reference	Description
10-AS1002FS-06A	Speed Controller	KQ2H06-G03N	Fitting
AD37-D	Auto drain valve	KQ2H10-G02N	Fitting
AF30-F02C-L-D	Air filter	KQ2H10-G03N	Fitting
AF30P-060S	Filter element for AF30, 5µm	KQ2H10-G04N	Fitting
AFD30-F02C-L-D	Micro mist separator, 0.01µm	KQ2R06-10A	Fitting
AFD30P-060AS	Filter element for AFD30	KQ2T06-00A	Fitting
AFM30-F02C-L-D	Air filter	T0604G-20	Tube 6mm
AFM30P-060AS	Filter element for AFM30	T1075BU-20	Tube 10mm
AN10-C06	Silencer	VHK2A-06F-06F	Finger valve
AN20-02	Silencer	VHS30-F02-D	Pressure relief 3 port valve
AR30-F02-D	Regulator	VX240KYXCA	2 port solenoid valve
G36-10-01-L	Pressure gauge	Y300-D	Spacer
IDG30LA-F03	Membrane air dryer	Y300T-D	Spacer with fastening system
IS10M-30-6L-D	Pressure switch	Y400T-D	Spacer with fastening system
KM16-06-06-3	Fitting		

Table 1: List of components of the pneumatic system coming from SMC.

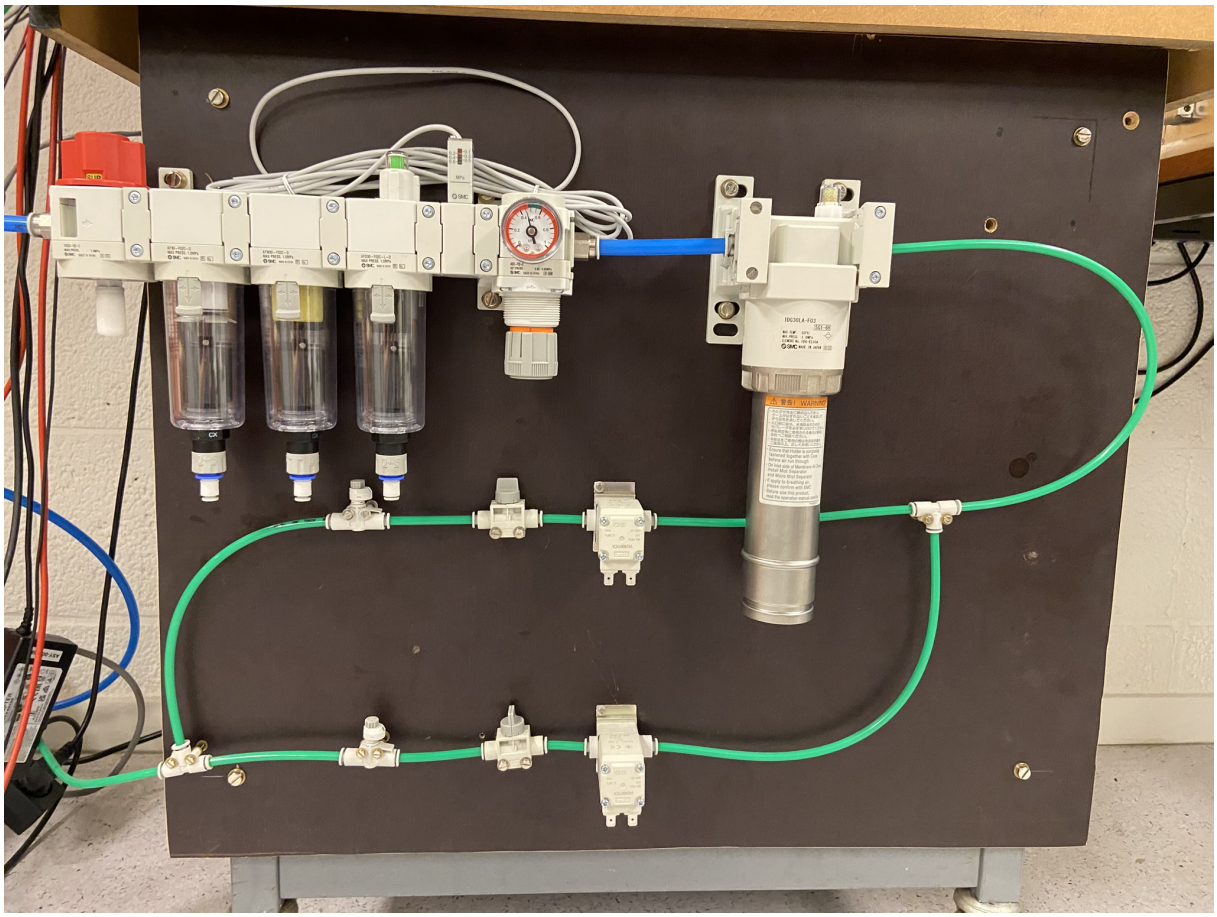

Figure 8: Part of the builded pneumatic system.

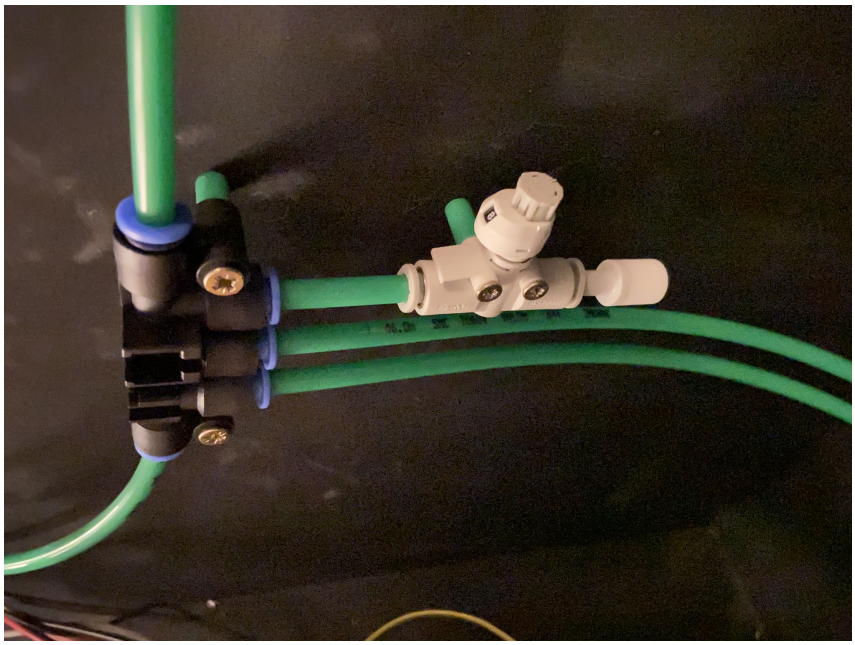

Figure 9: Diffuser in the enclosure.

F Appendix: Relative humidity and temperature monitoring

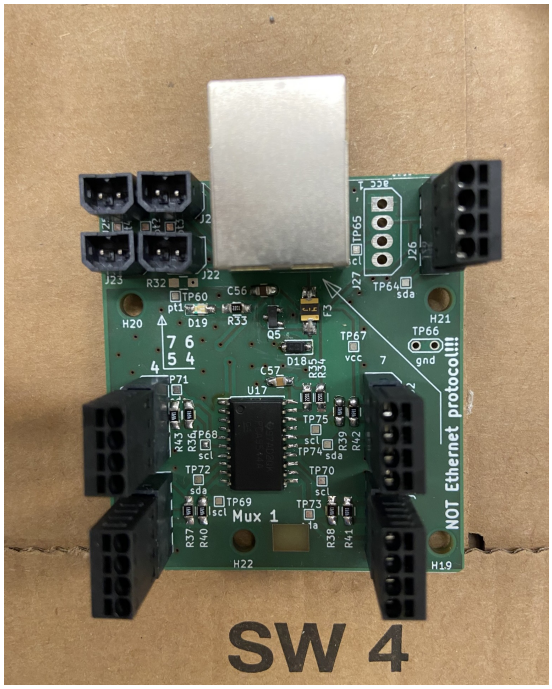

(a) Multiplexer PCB.

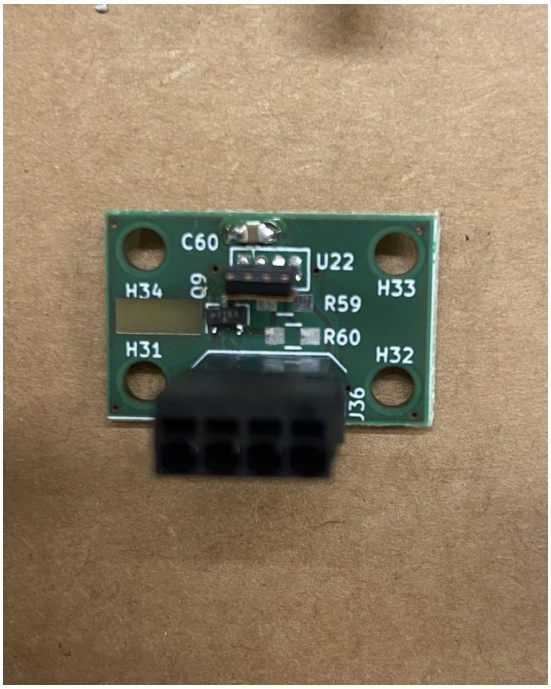

(b) PCB for HIH8120-021-001 temperature and relative humidity sensor (x4).

Figure 10: PCBs for temperature and relative humidity monitoring.

G Appendix: Graphical user interface of the light controller

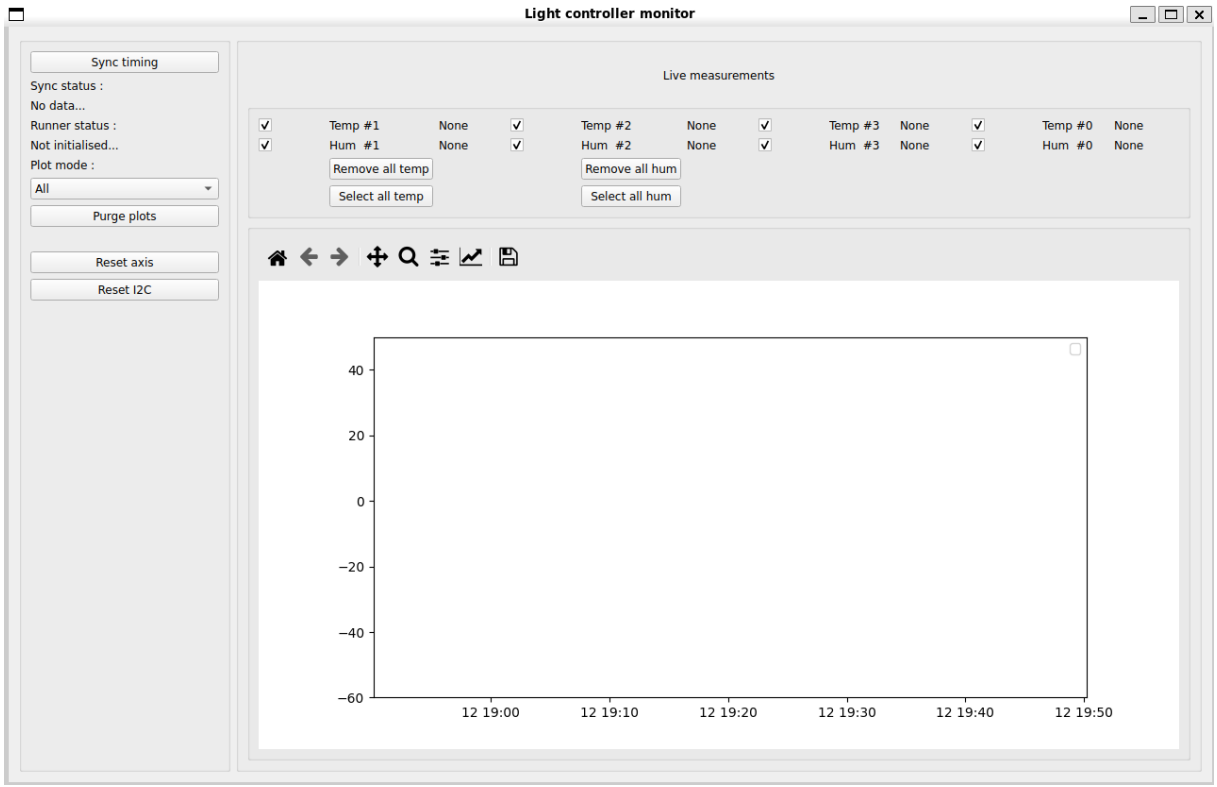

Figure 11: Light controller monitor.

H Appendix: Relative humidity measurements.

The Relative Humidity φ is defined as:

$$\varphi = \frac{p_D(T)}{p_D^*(T)} \quad \text{With } 0 \leq \varphi \leq 1 \tag{2}$$

with $p_D(T)$, the partial pressure of the vapor at the gas temperature T and $p_D^*(T)$, the saturation pressure of the vapor at the gas temperature T [33, p. 12].

(a) Relative humidity measurement inside the light-isolated cabinet.

(b) Relative humidity measurement at the opening of the light-isolated cabinet.

Figure 12: Relative humidity measurment for validation of the pneumatic system.

I Appendix: Transmission of visible light through a scratched solar cell.

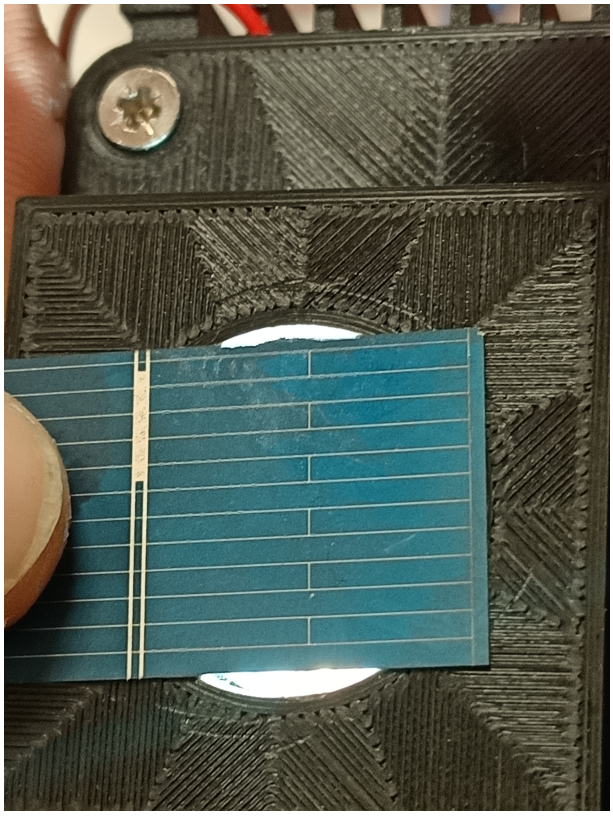

Figure 13: Check of the transmission of visible light through a scratched solar cell on the aluminium bachside.

J Appendix: Transparency of a CBC under IR illumination

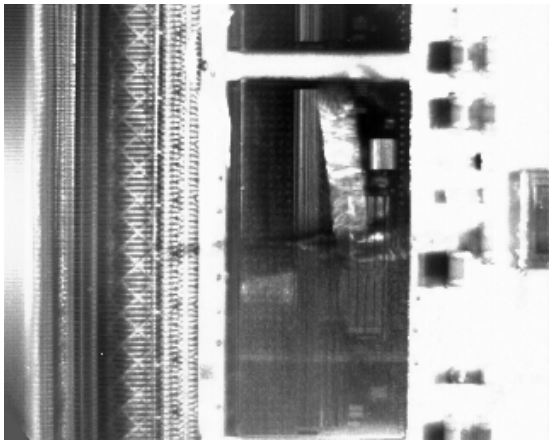

(a) CBC illuminated at 1200 nm.

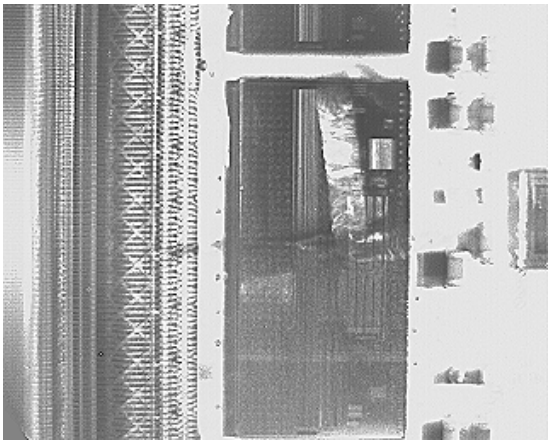

(b) Sharpened CBC image.

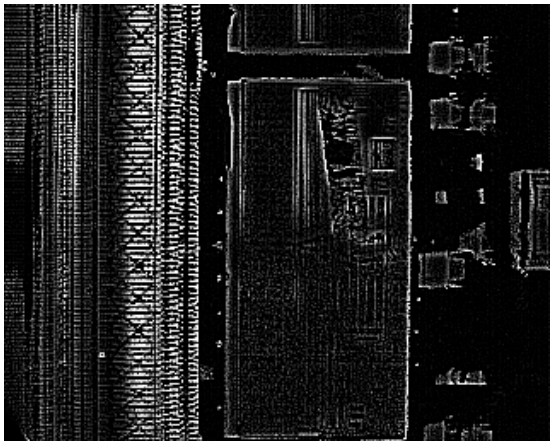

(c) Edge-detection filtered CBC image.

Figure 14: Transparency of a CBC under 1200 nm illumination.

K Appendix: Transient of the current source.

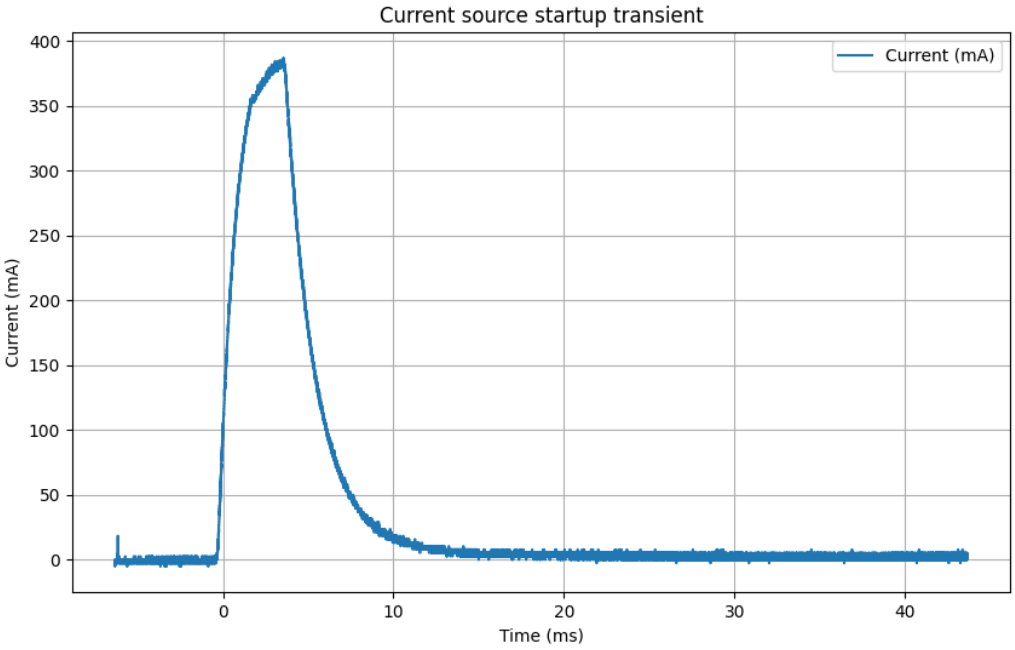

Figure 15: Current source stratup transient measured during the experiments performed on the decommissioned 2S sensor (see Section 4.3.2).